



**Politecnico
di Torino**

Politecnico di Torino

Master's degree in Civil Engineering Structures

A.a. 2022/2023

Ottobre 2023

**Structural analysis of
hybrid steel-glass sway frames with
semi-rigid joints modelled through
springs**

Supervisors:

Politecnico di Torino: Prof. Mauro Corrado

Ghent University: Prof. dr. ir.-arch. Jan Belis

Prof. dr. ir. Robby Caspeele

Counsellors:

Ghent University: Ir. Mirko Pejatovic

Candidate: Moschini Nicolas

Acknowledgements

This master dissertation closes my academic career, an experience which formed and changed me under different points of view. During these years many people helped, supported, and guided me along all the steps I have been performing and I thank you all.

This thesis works is the result of the link between two high-level universities such as the Polytechnic of Turin and the University of Ghent. I would like to express my gratitude to both universities for the educational and instructive opportunities they have provided me.

I would like to express my gratitude to my supervisors Prof. dr. ir.-arch. Jan Belis and Prof. dr. ir. Robby Caspeele for giving me the opportunity to perform this research. Furthermore, I also feel inclined to thank them for the advice and corrections they have provided me throughout the entire course of this work.

Furthermore, this work will also incorporate knowledge derived from the Polytechnic of Turin. Therefore, I wish to extend my thanks to my supervisor, prof. Mauro Corrado, for affording me the opportunity to undertake this thesis project.

Additional significant gratitude is owed to my advisor, Ir. Mirko Pejatovic, for all the support he has provided me, both during the modelling and results attainment phase, as well as during the thesis writing. In particular, I wish to thank him for his availability during the intermediate meetings, both for the guidance offered and his willingness to assist.

Another person from Ghent University, whose assistance has been instrumental, is ir. Stef Helderweirt. I feel obliged to express my gratitude for the extensive support he has provided me with the DSM tool, as well as for his availability in conducting meetings with me at any given time.

Throughout these years, I have encountered numerous people who have contributed significantly to my personal growth. However, certain persons have remained a constant presence, my family. I am enthusiastic to express my gratitude to my parents for their firm support and the sacrifices they have made to help me achieve this goal. Moreover, the greatest appreciation is reserved for my sister, Ambra, whose support has been fundamental. She has consistently offered guidance and assisted me in overcoming challenging situations.

Last but certainly not least, I wish to express my gratitude to some friends who have proven to be truly special throughout these years. They have stood by my side during both the most joyful moments and the challenging ones: Gianluca, Nazaret, Mattia, Marco and Lara.

Nicolas Moschini, October 2023

Ringraziamenti

Questa tesi di laurea magistrale segna la chiusura della mia carriera accademica, un'esperienza che mi ha formato e cambiato da diversi punti di vista. Durante questi anni molte persone mi hanno aiutato, sostenuto e guidato in tutti i passi che ho compiuto, e ci tengo a ringraziare tutti.

Questo lavoro di tesi è il risultato del legame tra due università di alto livello, come il Politecnico di Torino e l'Università di Gand. Desidero esprimere la mia gratitudine ad entrambe le università per le opportunità educative e formative che mi hanno offerto.

Desidero esprimere la mia gratitudine ai miei supervisori, il professor Jan Belis e il professor Robby Caspeele, per avermi dato l'opportunità di condurre questa ricerca. Inoltre, desidero ringraziarli per i consigli e le correzioni che mi hanno fornito durante tutto il corso di questo lavoro.

Inoltre, questo lavoro include anche conoscenze derivate dal Politecnico di Torino. Pertanto, desidero estendere i miei ringraziamenti al mio supervisore, il professor Mauro Corrado, per avermi offerto l'opportunità di intraprendere questo progetto di tesi.

Un'altra riconoscenza significativa è dovuta al mio correlatore, Mirko Pejatovic, per tutto il sostegno che mi ha fornito, sia durante la fase di modellazione che di ottenimento dei risultati, sia durante la stesura della tesi. In particolare, desidero ringraziarlo per la sua disponibilità durante gli incontri, sia per la guida offerta che per la sua disponibilità ad assistere.

Un'altra persona dell'Università di Gand, il cui aiuto è stato fondamentale, è Stef Helderweirt. Mi sento obbligato a esprimere la mia gratitudine per il sostegno esteso che mi ha fornito con lo strumento DSM, nonché per la sua disponibilità nel condurre incontri con me in qualsiasi momento.

Nel corso di questi anni, ho incontrato molte persone che hanno contribuito in modo significativo alla mia crescita personale. Tuttavia, alcune persone sono rimaste una presenza costante, la mia famiglia. Sono entusiasta di esprimere la mia gratitudine ai miei genitori per il loro saldo sostegno e i sacrifici che hanno fatto per aiutarmi a raggiungere questo obiettivo. Inoltre, la più grande gratitudine è riservata a mia sorella, Ambra, il cui supporto è stato fondamentale. Ha offerto costantemente orientamento e mi ha aiutato a superare situazioni difficili.

Infine, ma certamente non meno importante, desidero esprimere la mia gratitudine ad alcuni amici che si sono dimostrati davvero speciali nel corso di questi anni. Sono stati al mio fianco durante i momenti più gioiosi e quelli più impegnativi: Gianluca, Nazaret, Mattia, Marco e Lara.

Nicolas Moschini, Ottobre 2023

Permission of use on loan

The author gives permission to make this master dissertation available for consultation and to copy parts of this master dissertation for personal use.

In all cases of other use, the copyright terms have to be respected, in particular with regard to the obligation to state explicitly the source when quoting results from this master dissertation.

Nicolas Moschini, 26/10/2023

Structural analysis of hybrid steel-glass sway frames with semi-rigid joints modelled through springs

Nicolas Moschini

Supervisor(s): Prof. Mauro Corrado, Prof. dr. ir.-arch. Jan Belis, Prof. dr. ir. Robby Caspeele,
Counsellor: Ir. Mirko Pejatovic

Master's dissertation submitted in order to obtain the academic degree of
Master of Science in Civil Engineering

Academic year 2022-2023

Abstract

In last decades, the potential of glass in modern architecture, due to his transparency, is increased. From this, it started to be employed as load-bearing structural material for beams and columns. As a result, there is a necessity to find solutions for its brittle behaviour and improve its post-fracture performances. One of the most developed concepts are the "hybrid glass beams," where glass is combined with other materials, like stainless steel, to increase its strength and post-fracture behaviour. In particular, this master's thesis focuses on the correct modelling of the structural system. The primary objective is to accurately replicate the connection's stiffness using a spring constant. To achieve this, the analysis will start with the experimental results of a beam-column connection developed by Mirko Pejatovic, from which the spring constant for the three considered laminations will be determined. Subsequently, two distinct numerical models will be developed to replicate the experimental outcomes. The first model will be created using ABAQUS Standard, accurately reproducing the lamination and utilizing a UMAT model which recreate the brittle behaviour of glass. The other numerical analysis will be performed with Python, employing a code based on the Direct Stiffness Method, known as the DSM tool. After isolating the connection, itself, the analysis will then shift to a frame composed of three columns and two beams subjected to both vertical and horizontal loads. Finally, a parametric study encompassing various load configurations will be executed to understand the influence of vertical and horizontal loads on the load-bearing capacity of the structure.

Keywords

reinforced laminated glass beams, semi-rigid connections, numerical modelling, user-defined material model, direct stiffness method

Structural analysis of hybrid steel-glass sway frames with semi-rigid joints modelled through springs

Nicolas Moschini

Supervisor(s): Prof. Mauro Corrado, Prof. dr. ir.-arch. Jan Belis, Prof. dr. ir. Robby Caspeele
Counsellor: Ir. Mirko Pejatovic

Abstract— In last decades, the potential of glass in modern architecture, due to his transparency, is increased. From this, it started to be employed as load-bearing structural material for beams and columns. As a result, there is a necessity to find solutions for its brittle behaviour and improve its post-fracture performances. One of the most developed concepts are the "hybrid glass beams," where glass is combined with other materials, like stainless steel, to increase its strength and post-fracture behaviour. In particular, this master's thesis focuses on the correct modelling of the structural system. The primary objective is to accurately replicate the connection's stiffness using a spring constant. To achieve this, the analysis will start with the experimental results of a beam-column connection developed by Mirko Pejatovic, from which the spring constant for the three considered laminations will be determined. Subsequently, two distinct numerical models will be developed to replicate the experimental outcomes. The first model will be created using ABAQUS Standard, accurately reproducing the lamination and utilizing a UMAT model which recreate the brittle behaviour of glass. The other numerical analysis will be performed with Python, employing a code based on the Direct Stiffness Method, known as the DSM tool. After isolating the connection, itself, the analysis will then shift to a frame composed of three columns and two beams subjected to both vertical and horizontal loads. Finally, a parametric study encompassing various load configurations will be executed to understand the influence of vertical and horizontal loads on the load-bearing capacity of the structure.

Keywords— reinforced laminated glass beams, semi-rigid connections, numerical modelling, user-defined material model, direct stiffness method

I. INTRODUCTION

Glass is becoming always more popular as a structural material. However, due to his brittle behaviour, it needs to be employed together with other materials in order to acquire strength and post-fracture performances. To further increase strength and characteristics, the concept of "hybrid glass beams" was introduced. In specific, the most promising solution are the reinforced glass beams, in which laminated glass panes are reinforced with stainless steel. The cross sections analysed in this research are the are the outcome of a research program which originated in the early 2000s and is still going on to further improve this concept. However, in order to achieve high performance in a structural system, not only the cross-sections strength plays the central role but also the connections between the elements. Modelling the connection in a correct way influence the distribution of the internal forces and so the design of the structure. From this, the best way to recreate the correct behaviour of connection is to model it as semi-rigid using springs. However, with limited

study and provisions in current codes, there is a need to explore this aspect through numerical and experimental studies. Thanks to the numerical modelling, the glass behaviour can be replicate aligning it with experimental results. From this, parametric studies allow insight into the effect that the parameters have on structure response, such as reinforcement, dimensions, external loads and rigidity of the connections.

II. CROSS-SECTIONS AND MATERIALS

In the research three different cross sections have been examined. In particular, the materials employed are Annealed Float Glass, Stainless Steel AISI 304 and SentryGlas® as interlayer. What differ between the three configurations is the reinforcement size. In particular, the first one present a stainless-steel reinforcement 10x10 mm, the second one 8x10 mm and the third 10x5mm, being the first number the width and the second one the height. Three glass panes are present, two external one having a width of 6 mm and a height of 125 mm, and an internal one. The internal glass has a height of 105 mm in all the cross section but the thickness change in function of the width of the reinforcement. in the lamination. Two foils of interlayer are employed between the elements giving a thickness of 1,52 mm. The resulting cross section are reported in Figure 1.

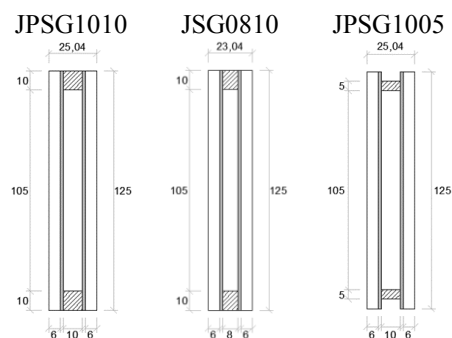


Figure 1: Cross sections analysed in the research.

III. NUMERICAL MODELS

Two numerical models will be employed within the scope of this research. A 3D FEM model developed in the software ABAQUS Standard and an analytical 1D model developed in Python which takes the name of DSM Tool.

A. ABAQUS model

In the software ABAQUS the three different cross-sections are modelled respecting the sizes of each element and recreating the correct lamination. In order to do this, each

element is created and then assembled together in the final form in both the models that will be presented. The materials are defined in the context of the program using their mechanical characteristics. In particular for the glass a user-defined model (UMAT) is used. This can recreate the brittle behaviour of glass and also the crack formation. The interlayer is defined as a linear infinite plastic material, characterized by the mechanical characteristics resulting from the experiments performed at 23° with a load duration of 30 minutes. The stainless-steel is defined as a plastic material and the mechanical characteristics were defined by experimental test that were performed on samples of the different reinforcement typologies. In order to optimize the precision of the results and the calculation time just half of the cross-section is modelled both in the model of the connection and also in the model of the frame.

B. DSM tool

This python code has been developed inside the Ghent university and is based on the Direct Stiffness Method. The tool works in an iterative way defining a new stiffness of the elements at each load increment. To account for the materials non-linearities it bases his calculations on the moment-curvature diagram, which is created from the stress-strain relationship of the materials. This was developed to study reinforced concrete cross sections, however, defining a stress strain diagram describing the linear elastic behaviour of glass was possible to recreate the system under analysis. Nevertheless, the tool does not give the possibility to model real geometry of the cross section. As a result, the interlayer was neglected and the stainless-steel reinforcement was defined as a bar, having the same area of the square once. Thanks to certain modifications made in the code, it has become possible to model the connections as semi-rigid by introducing a spring with a specified stiffness defined in kNm/rad at the desired nodes.

IV. ANALYSIS OF THE CONNECTION

The aim of this part of the study is to determine to what extent the previously presented numerical models accurately replicate the behaviour of an L-shaped connection between two elements, such as a beam-column connection.

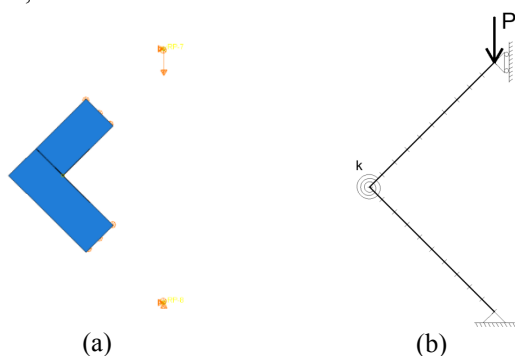


Figure 2: Model in ABAQUS (a) and model in DSM tool (b)

Firstly, based on the experimental results performed by ir. Mirko Pejatovic, three different spring constants, related to the connections created with the different laminations, are defined. Afterwards, the ABAQUS model is created. Is important to highlight that in order to increase the precision of the results just a portion of the connection have been modelled (Figure 2(a)). The boundary conditions, which are an hinge at the bottom node and an impose displacement at the tope node, were applied on the structure by means of tie constrains. From this

analysis was possible to determine the crack pattern in the connection and the maximum loads that the connections can sustain. Those loads are then applied in the DSM tool model. In this case two different simulations are performed, one with the connection modelled as rigid and one with the semi-rigid connections using the spring constant previously defined. Comparing the results coming from these simulations with the experimental once can be evinced that the results obtained from ABAQUS more accurately replicate the experimental findings. This is attributed to a lower level of model approximation compared to that reproduced in Python. Within the DSM tool, various approximations have been employed, both concerning material behaviour and section geometry. This leads to optimal outcomes within the linear-elastic range, yet it inadequately approximates the connection behaviour during the plastic phase of materials. The graphs illustrating the simulation results together with the experimental once for the three cases are depicted in Figures 3, 4, and 5. More specifically, concerning the first examined configuration, JPSG1010, the outcomes of the ABAQUS model closely align with the experimental results, despite minor disparities. Conversely, the DSM tool results exhibit elevated stiffness, causing the model to collapse at significantly lesser relative rotations compared to the experimental findings.

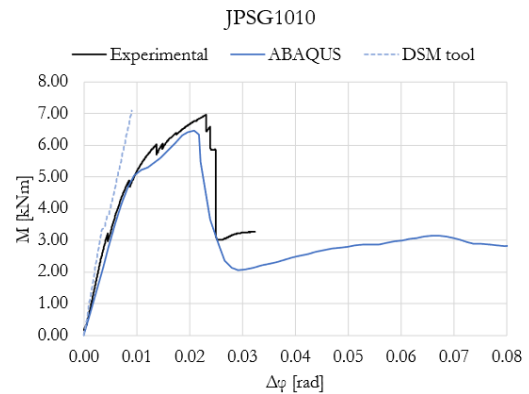


Figure 3: Resulting curves for the connection modeled with JPSG1010.

For the second case, JPSG0810, the ABAQUS model initially demonstrates greater stiffness within the linear-elastic phase. Subsequently, however, the connection behaviour is accurately replicated up to failure. The DSM tool accurately emulates the linear-elastic behaviour, but due to its load increment-based model, it fails to recreate the plastic phase of the connection.

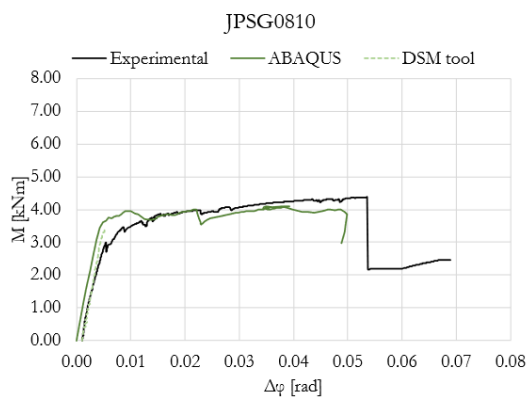


Figure 4: Resulting curves for the connection modelled with JPSG0810.

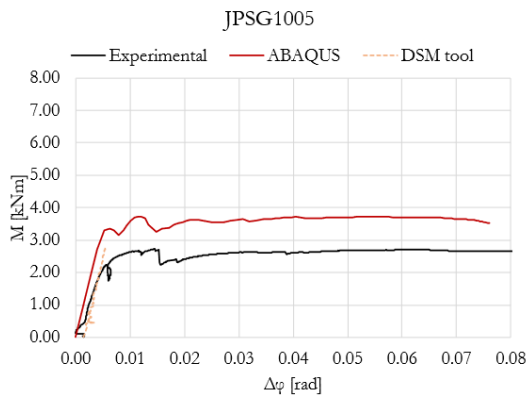


Figure 5: Resulting curves for the connection modelled with JPSG1005.

In the case of the final configuration, JPSG1005, when analysed through the DSM tool, it yields the same results as the previously presented case, JPSG0810. Meanwhile, the 3D model created in ABAQUS exhibits a similar trend to the experimental data, although the section demonstrates higher resistance to moments. This discrepancy could be attributed to the fact that the 3D model fails to reproduce the loss of adhesion between the reinforcement and interlayer.

V. FRAME ANALYSIS

Once the specific study of the connection alone had been conducted, utilizing the same sections previously mentioned, three distinct frames were constructed in order to analyse their behaviour. The frame is composed of three columns and two beams. Column height and beam length both measure 1500 mm. The system will be subjected to two vertical loads P , applied at the midspan of the beams, and a horizontal load H acting on the top of the left column. Hinge boundary conditions are applied to the column base connection due to the practical challenges associated with ensuring zero rotation in a real-case scenario.

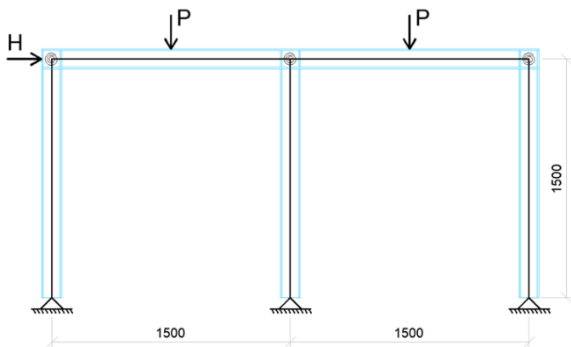


Figure 6: Frame geometry.

In this study, no available experimental data is accessible for direct comparison, limiting the possibility of validating results against real behaviour. Comparing the results coming from the two numerical models, it is evident that the 3D model in ABAQUS capture the behaviour of the frame more comprehensively. This alignment is due to the inherent nature of the FEM models, characterized by reduced approximations and assumptions. Analysing the results of the frames and comparing them with the outcomes of the corner analysis, a distinct trend emerges. The ABAQUS results are approximated in a more closely way when the connections are modelled as

rigid in the DSM tool. However, the failure of the system is lower compared to the FEM model. When the spring constant is employed, the model exhibits reduced stiffness and divergent results. It's important to note that the spring constant representation allows for achieving higher loads at failure due to higher ductility. Consistently observed across all studied cases, the behaviour can be attributed to the operational principles of the DSM tool. As previously stated, the tool monotonically increases the load without controlling displacements. Additionally, its calculations rely on moment-curvature relationships of cross-sections. Once the maximum moment occurs in any section, the tool assumes structural failure, omitting stress redistribution that is accounted for in ABAQUS.

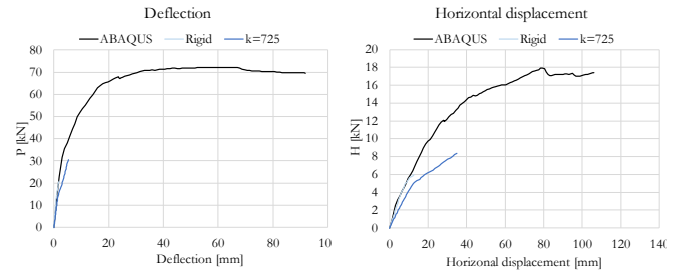


Figure 7: Resulting curves for the frames modelled with JPSG1010.

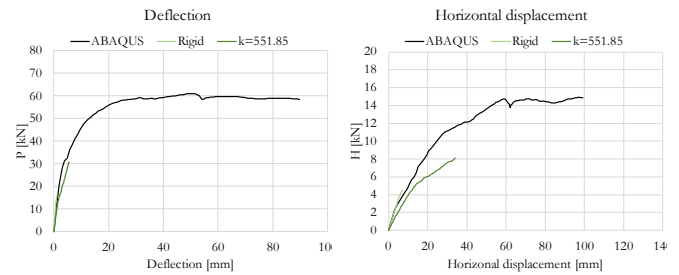


Figure 8: Resulting curves for the frames modelled with JPSG0810

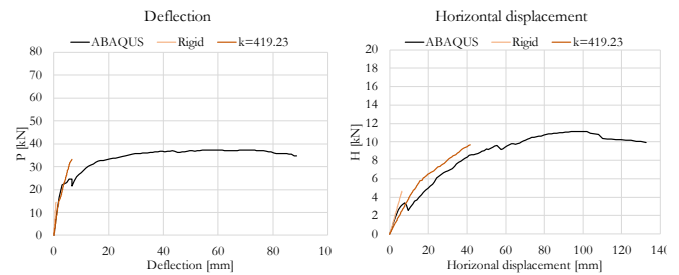


Figure 9: Resulting curves for the frames modelled with JPSG1005

A detailed examination of each case reveals that for JPSG1010, the DSM tool model fails at approximately 40% of the maximum load achieved in ABAQUS. Correspondingly, for JPSG0810, the failure load in the DSM tool model is approximately registered at 50% of the maximum load. Interestingly, in the case of JPSG105, the maximum load endured by the structure aligns with ABAQUS results, with similar trends in the load-displacement diagrams. This divergence can potentially be explained by the fact that the stainless steel 5x10 mm displays greater ductility, despite being able to withstand lower stresses.

VI. PARAMETRIC STUDY

C. Only vertical loads P applied

When only vertical loads are applied the objective is to determine the maximum capacity of the frame under just gravity load. Remarkably, the maximum loads recorded across the three models in ABAQUS are consistent with the results presented in the frame analysis, where both vertical and horizontal loads were applied together. Across all cases, the initiation of the first crack is conspicuously apparent, represented by prominent peaks on the left side of the graphs. Following this, a transition from the linear-elastic phase occurs, leading to an ascending branch until the maximum load is reached, beyond which a descending trend ensues. Two sets of curves will be presents, one that depict the overall deflection from the ABAQUS model, and one indicating differences in initial stiffness across models.

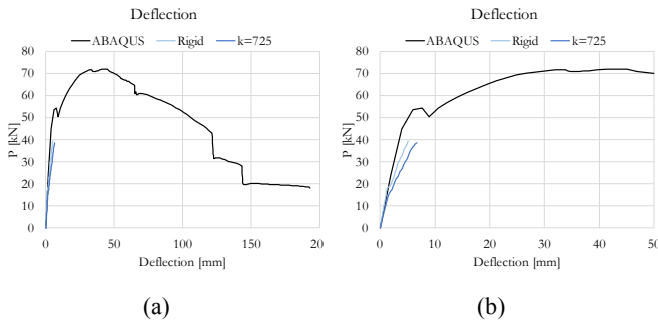


Figure 10: Resulting curves with the maximum deflection achieved (a) and with a focus on the initial stiffness (b) for the frame modelled with JPSG1010.

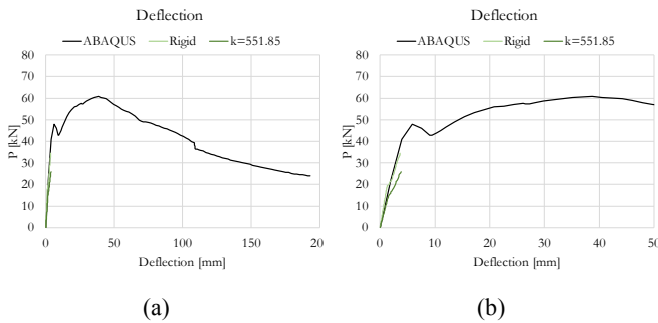


Figure 11: Resulting curves with the maximum deflection achieved (a) and with a focus on the initial stiffness (b) for the frame modelled with JPSG0810.

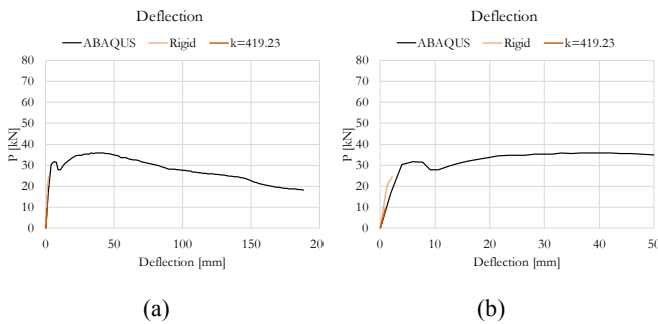


Figure 12: Resulting curves with the maximum deflection achieved (a) and with a focus on the initial stiffness (b) for the frame modelled with JPSG105.

D. Only horizontal load H applied

This investigation centred on the application of only the horizontal load H . From the graphs in Figure 13, 14 and 15 the maximum displacement thresholds that the structure can endure it is evident, this for the first two cases. However, the same pattern does not apply to the last configuration, which lacks the characteristic drop observed in the others. From this, it is not possible to define a real failure of the structure from the numerical results. In this analysis, a significantly greater increase in load-bearing capacity is observed for horizontal loads, comparing this to the case in which both vertical and horizontal loads are simultaneously applied. This underscores the influence of vertical load application on the structure's ability to support horizontal loads.

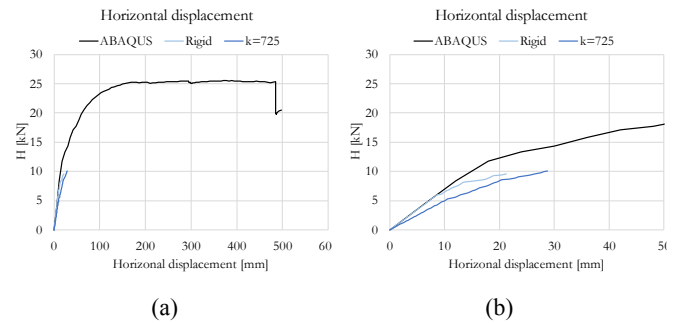


Figure 13: Resulting curves with the maximum horizontal displacement achieved (a) and with a focus on the initial stiffness (b) for the frame modelled with JPSG1010.

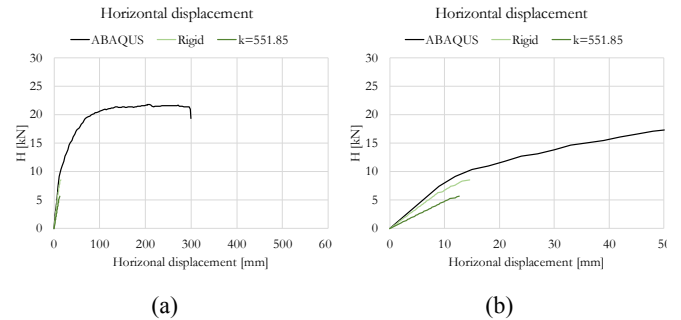


Figure 14: Resulting curves with the maximum horizontal displacement achieved (a) and with a focus on the initial stiffness (b) for the frame modelled with JPSG0810.

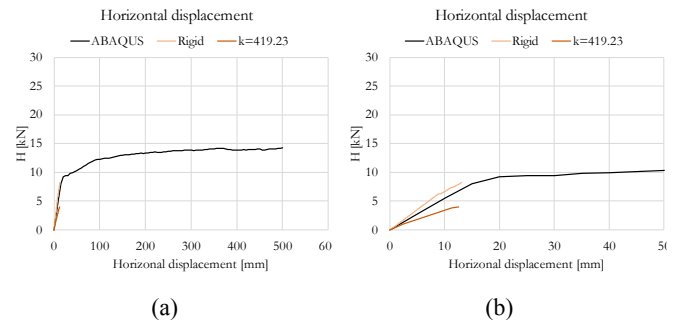


Figure 15: Resulting curves with the maximum horizontal displacement achieved (a) and with a focus on the initial stiffness (b) for the frame modelled with JPSG1005.

E. Two-step analysis

The last parametric study has the objective to understand the influence that different values of the applied vertical loads have on the structural behaviour. This analysis will be performed only in the software ABAQUS because the DSM tool does not

have the possibility to perform loading in two steps. The applied horizontal force is the one coming from the previous analysis when only horizontal loads were applied. While, for what concerns the vertical loads, those were chosen as a percentage on the maximum load that the structure can withstand.

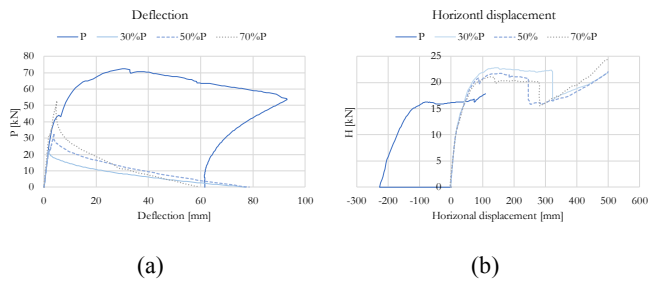


Figure 16: Resulting curves for frame modelled with JPSG1010 on which different percentage of load P have been applied followed by H

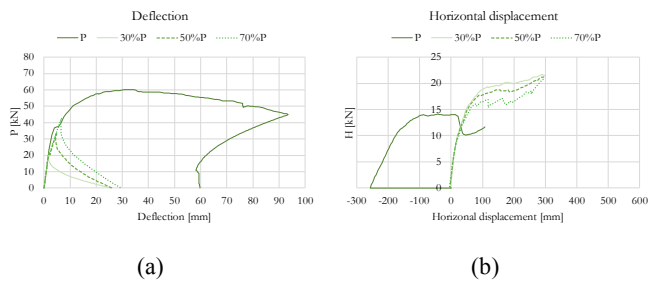


Figure 17: Resulting curves for frame modelled with JPSG0810 on which different percentage of load P have been applied followed by H.

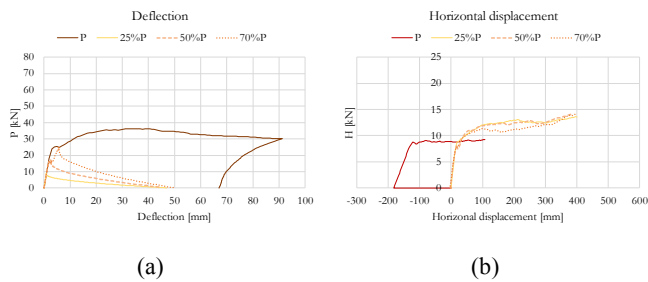


Figure 18: Resulting curves for frame modelled with JPSG1050 on which different percentage of load P have been applied followed by H.

In all three instances, the reference curve, designated simply as P emerges as the outcome of implementing a 100 m displacement in the downward y-direction, followed by a 100 m displacement in the x-direction, as the analysis previously presented in Chapter V. In all three cases, it can be observed that the graph depicting the horizontal displacement, resulting from this initial analysis, exhibits a displacement in the negative x-direction, discernible through the presence of straight lines along the x-axis. This is because, due to the hinged boundary conditions at the base and the significant vertical displacement, the frame has become unstable and started to slide towards the left (negative x-direction). This behaviour has been recorded in all three frames with different values. Subsequently, at the end of the first step of the analysis,

the application of the horizontal load occurs, resulting in the curves observed for the different cases. Has to be pointed out that, this instability has not occurred, or to a lesser extent, in cases where a smaller loads P have been applied.

In the first case, characterized by the frame modelled with the JPSG1010 lamination, it can be observed that the application of the maximum load P results in the frame having enough strength to still support a horizontal load H of 16.81 kN. However, when a portion of the load P is applied, the frame can sustain higher horizontal loads, averaging around 22 kN. This leads to an increase of 23% in load-bearing capacity compared to when the maximum load P is applied. This result can be compared with the outcomes from the previous parametric study, where only a horizontal force was applied. In that case, the maximum value of load H was 25.52 kN. This implies that, applying a load P between 70% and 30% of the maximum vertical load, the horizontal load-carrying capacity of the structure is reduced from 17% to 10% respectively. Furthermore, it is essential to emphasize that the failure of the structure occurs at significantly lower horizontal displacements compared to when only horizontal loads are applied. This is because, at the end of the application of load P, crack formation is already occurring in various parts of the structure, in particular in the connections and at the centre of the beams. The final displacement can decrease by 42%, when a load equal to 70% of P is applied, and by 35% when 30% of P is applied.

The second lamination under examination presents similar results to the first, however notable deviations are registered particularly when a percentage of load P is applied. In this case, when the maximum load P is applied, the vertical load-bearing capacity decreases by 35%, compared when only the horizontal load is applied. However, when 70% of load P is applied, the capacity drops by 21%, and in the case of applying 30% of load P, the capacity decreases of a lower amount, by 7%. The intriguing aspect of these simulations is that the structural failure is not clearly discernible from the graphs. After the end of the elastic range, the curves appear to diverge. A closer examination of the data reveals that at certain points, there is a reduction followed by the start of the ascending branch. At these points, the failure of the structure was assumed, which in this case coincides with the maximum horizontal load considered. This final failure, as before, occurs at smaller horizontal displacements. The registered decrease moves from 40% to 45% when 30% or 70% of the vertical load is applied. Therefore, in this case, the horizontal displacement decreases to a greater extent.

The last case under analysis, utilizing the JPSG1005 section, behaves similarly to the preceding JPSG0810 case. As in the previous instance, it is not feasible to identify structural failure clearly. The decrease in load-bearing capacity is also comparable, where applying 30% of load P results in an 8% reduction, and the application of 70% of load P leads to a 20% decrease in capacity. When the maximum load P is applied, the reduction in strength is 35%. By following the same assumptions adopted in the previous case, the structural failure was assumed for horizontal displacements beyond which a decrease in data was observed, followed by the initiation of the ascending branch. Unfortunately, in this case, it is not possible to compare the data with the results of the earlier analysis, as obtaining consistent results from ABAQUS when only horizontal loads were applied was not possible. In this case further experimental investigation is needed.

VII. CONCLUSIONS

This study underscores the critical importance of understanding connections within glass structures and specifically delves into the influence of connection stiffness, modelled using springs, on the structural behaviour. The research begins from experimental data to define rotational stiffness constants employed in the DSM tool, leading to accurate experimental reproduction. However, limitations arise from the code structure in cases of individual connection analysis. Once the elastic branch is concluded the plastic capacity is not faithfully recreated, this is because the code works in a load-controlled manner and a series of assumptions needed to be applied. Furthermore, the DSM tool considers the moment-curvature diagram of sections, leading to entire structure collapse when the maximum capacity is reached in one section, lacking in recreating stress redistribution and the real cracking behaviour of glass. The 3D model built in ABAQUS accurately mirrors the structural behaviour. While the first connection (JPSG1010) the stiffness is optimally represented, some deviations occur in the second and third cases (JPSG0810 and JPSG1005). ABAQUS inability to replicate the loss of adhesion between the reinforcement and the interlayer may contribute to discrepancies. Besides this, the models consistently exhibit more accurate behaviour replication, partly due to fewer approximations. The frame analysis performed with the DSM tool shows its inability to recreate the correct behaviour, as it yields lower structural failure loads. In contrast, the 3D model having less approximations and considering crack formation through its UMAT model, accurately emulating brittle glass behaviour. Nevertheless, experimental verification is essential. The parametric study reveals that applying loads lower than maximum capacity leads to robust resistance against horizontal loads. After applying the 70% of the maximum vertical load, the structural capacity decrease of the 20%. Under the same vertical load condition, the maximum collapse displacements decrease by approximately 40%. In conclusion, the ABAQUS Finite Element Model (FEM) effectively replicates various lamination behaviour with minor deviations. Meanwhile, the analytical model through the DSM tool reproduces the linear-elastic phase but fails to encompass complete behaviour due to high assumptions in cross-section and configuration modelling, which inevitably limits result accuracy.

In the future further research can be focused on the precision of DSM tool. An implementation of the code is required to address the brittle behaviour of glass and how fractures propagate, as in the case of a UMAT model. Another option is to work on the moment-curvature diagrams in a different way, without altering the geometric characteristics of the section but changing how they are defined. As for the frame model, a more in-depth study of the central connection, where there are two beams and a column, should be carried out. Unfortunately, without experimental results that can prove the correct value of the spring constant, recreating the stiffness of that connection using a k value is quite challenging. As a final improvement, a more thorough study of the stiffness of the base connection of the column could also be conducted, allowing this connection to be modelled as a spring with a certain rigidity as in the case of the top connections.

REFERENCES

- Cupać, J., Martens, K., Nussbaumer, A. et al (2017). *Experimental investigation of multi-span post-tensioned glass beams*. *Glass Struct Eng* 2, 3–15. <https://doi.org/10.1007/s40940-017-0038-5>.
- Huang, W. (2017). *L-shaped Connection for Glass Portal Frame. Structural analysis and its application*. TU Delft.
- J. Wright and J. MacGregor (2012). *Flexure: Behaviour and Nominal Strength of Beam Sections. in Reinforced Concrete: Mechanics and Design*, 6th ed. USA: Pearson, ch. 4, sec. 2, pp. 108-119.
- Louter, P. C. (2011). *Fragile yet ductile: structural aspects of reinforced glass beams*. TU Delft.
- Louter, P. C., Belis, J., Veer, F. A., and Lebet, J.-P. (2012b). *Structural response of SG-laminated reinforced glass beams; experimental investigations on the effects of glass type, reinforcement percentage and beam size*. *Engineering Structures*, 36:292-301.
- Martens, K. (2018). *Statically Indeterminate Reinforced Glass Beams*. Ghent University.
- Moreman, S (2022). *Rotational characteristics of steel reinforced glass beam-to-column adhesive joints: experimental and numerical study*. Ghent University.
- Pejatovic, M., Caspeele, R., & Belis, J. (2022). *Numerical study of post-fracture behavior of a two-sided reinforced laminated glass beam-column connection prototype*. *GLASS STRUCTURES & ENGINEERING*, 7(3), 399–414. <https://doi.org/10.1007/s40940-022-00193-x>
- R. Van Coile (2016). *Towards reliability-based structural fire safety: development and probabilistic applications of a direct stiffness method for concrete frames exposed to fire*. M.Sc. dissertation, Dept. Struct. Eng., Ghent University.
- Santarsiero, M., Bedon, C., Moupagitsoglou, K. (2019). *Energy-based considerations for the seismic design of ductile and dissipative glass frames*. *Soil Dynamics and Earthquake Engineering*. <https://www.sciencedirect.com/science/article/pii/S0267726119304063>
- Symoens, E. (2019). *Experimental validation of a numerical model for the simulation of membrane action in reinforced laminated glass beam systems*. Ghent University.

Table of contents

Acknowledgements	i
Permission of use on loan	v
Abstract	vii
Extended Abstract	vii
Table of contents	xv
List of figures	xv
List of tables	xv
List of abbreviations and symbols	xv
Chapter 1 - Introduction	1
1.1 Aim	2
1.2 Contents of this research	3
Chapter 2 - State of art and materials	1
2.1 Structural use of glass	1
2.2 Hybrid glass beam	3
2.2.1 Composite glass beams	3
2.2.2 Reinforced and post-tensioned glass beams	4
2.3 Materials used in this research	12
2.3.1 Annealed Float Glass	12
2.3.2 SentryGlas®	14
2.3.3 Stainless steel	15
Chapter 3 - Connection and frame modelling	19
3.1 Connection modelling	19
3.2 Frame analysis	21
3.2.1 Parameters influencing the response	21
3.2.2 Energy-based analytical model	22

Chapter 4 - Analysis of the connection	25
4.1 Overview	25
4.2 Experimental tests	27
4.2.1 Description of the tests	27
4.2.2 Experimental results	29
4.3 3D FEM analysis using reducing element approach	31
4.3.1 Material implementation	31
4.3.2 Definition of the geometry	32
4.3.3 Results	34
4.4 Direct Stiffness Method tool	39
4.4.1 Definition of the geometry	40
4.4.2 Cross-section characteristics	41
4.4.3 Results	45
4.5 Comparison of the results	48
Chapter 5 - Frame analysis	53
5.1 3D FEM analysis using reducing element approach	54
5.1.1 Definition of the geometry	54
5.1.2 Results	57
5.2 Direct Stiffness Method tool	60
5.2.1 Definition of the geometry	60
5.2.2 Results	61
5.3 Comparison of the results	63
5.4 Parametric study	65
5.4.1 Only vertical load P	65
5.4.2 Only horizontal load H	70
5.4.3 Two-step analysis	75

Chapter 6 - Conclusions	85
6.1 Overall conclusions	85
6.2 Future work	87
Bibliography	89

List of figures

Figure 2.1: Examples of composite glass beams [Martens, 2018]	3
Figure 2.2: Desired load-carrying behaviour for structural glass beams [Martens et al., 2018]	5
Figure 2.3: Steel-reinforced glass beam section [Martens et al., 2018]	6
Figure 2.4: Load-deflection diagrams for beam specimens GB-interlayer (left) and SG-interlayer (right) [Martens et al., 2018]	6
Figure 2.5: Reference cross section (a), cross sections investigated for the reinforcement percentage (b) and scale factor (c) [Martens et al., 2018]	7
Figure 2.6: Load-displacement curves for the cross section with solid reinforcement (a) and larger-scaled section (b) [Martens et al., 2018]	8
Figure 2.7: Load-displacement curves with different glass types [Martens et al., 2018]	9
Figure 2.8: Cross section used by Orlando et al. [Martens et al., 2018]	9
Figure 2.9: Load-deflection curves of the FRP reinforced beams from Orlando et al. [Martens et al. 2018]	10
Figure 2.10: Cross section of the post-tensioned glass beam in Louter et al. 2014 [Martens, 2018]	11
Figure 2.11: Load-deflection curves related with the post tensioned glass beam Louter, Cupac et al. [Martens et al., 2018]	11
Figure 2.12: Schematic representation of the float glass process [Martens, 2018]	12
Figure 2.13: Schematic representation of the stress-strain diagram of glass in tensile loading	13
Figure 2.14: Stress-strain diagrams of the three stainless steel reinforcement	16
Figure 3.1: Different joints according to rotational stiffness [Huang, W., 2017]	19
Figure 3.2: Structural behaviour of connections [Huang, W., 2017]	20
Figure 3.3: Relationship between the rigidity of the connections (k) and the effect on the bending moment [Huang, W., 2017]	21
Figure 3.4: Schematic representation of (a) the structural glass frame object of analysis, with (b) detail view of a typical push-pull moment connection at the base of the columns.	22
Figure 4.1: Model in ABAQUS (a) and model in DSM tool (b)	25
Figure 4.2: Schematization of the test set up.	27
Figure 4.3: Different cross section typologies	28

Figure 4.4: Moment-Rotation curves of the experiments	29
Figure 4.5: Half-cross sections implemented in ABAQUS Standard	32
Figure 4.6: 3D FEM model in ABAQUS, applied boundary condition (a)	33
Figure 4.7: Mesh applied on the corner element	34
Figure 4.8: Position and nomenclature of the points used for the analysis	35
Figure 4.9: Resulting curves from experiments and DSM Tool for JPSG1010	36
Figure 4.10: Resulting curves from experiments and DSM Tool for JPSG0810	36
Figure 4.11: Resulting curves from experiments and DSM Tool for JPSG1005	37
Figure 4.12: Resulting cracking pattern for JPSG1010	38
Figure 4.13: Resulting cracking pattern for JPSG0810	38
Figure 4.14: Resulting cracking pattern for JPSG1005	38
Figure 4.15: Subdivision of the corner element	40
Figure 4.16: Graphs of the constitutive law of the materials	41
Figure 4.17: Real cross section (a), numerical cross section (b) and moment-curvature diagram defined by the DSM tool (c) for JPSG1010	42
Figure 4.18: Real cross section (a), numerical cross section (b) and moment-curvature diagram defined by the DSM tool (c) for JPSG0810	43
Figure 4.19: Real cross section (a), numerical cross section (b) and moment-curvature diagram defined by the DSM tool (c) for JPSG1005	43
Figure 4.20: Position of the chosen points in the undeformed (a) and deformed (b) configuration	45
Figure 4.21: Resulting curves from experiments and DSM Tool for JPSG1010	47
Figure 4.22: Resulting curves from experiments and DSM Tool for JPSG0810	47
Figure 4.23: Resulting curves from experiments and DSM Tool for JPSG1005	47
Figure 4.24: Resulting curves for JPSG1010	49
Figure 4.25: Resulting curves for JPSG0810	49
Figure 4.26: Resulting curves for JPSG1005	50
Figure 5.1: Schematic representation of the frame	53
Figure 5.2: Frame modelled in ABAQUS Standard	54
Figure 5.3: Applied boundary condition in the 3D FEM model	55
Figure 5.4: Mesh applied to the frame	56
Figure 5.5: Load- deflection curves resulting from 3D FEM analysis in ABQUS	58
Figure 5.6: Load-displacement curves resulting from 3D FEM analysis in ABQUS	58

Figure 5.7: Crack pattern at failure for the frame modelled with JPSG1010	59
Figure 5.8: Crack pattern at failure for the frame modelled with JPSG0810	59
Figure 5.9: Crack pattern at failure for the frame modelled with JPSG1005	59
Figure 5.10: Subdivisions of the elements composing the frame	60
Figure 5.11: Subdivision of the elements inside the frame thickness.	61
Figure 5.12: Results from the DSM tool for JPSG1010	62
Figure 5.13: Results from the DSM tool for JPSG0810	62
Figure 5.14: Results from the DSM tool for JPSG1005	62
Figure 5.15: Resulting curves for the frames modelled with JPSG1010	64
Figure 5.16: Resulting curves for the frames modelled with JPSG0810	64
Figure 5.17: Resulting curves for the frames modelled with JPSG1005	64
Figure 5.18: Resulting curves with the maximum deflection achieved (a) and with a focus on the initial stiffness (b) for the frame modelled with JPSG1010.	66
Figure 5.19: Resulting curves with the maximum deflection achieved (a) and with a focus on the initial stiffness (b) for the frame modelled with JPSG0810.	66
Figure 5.20: Resulting curves with the maximum deflection achieved (a) and with a focus on the initial stiffness (b) for the frame modelled with JPSG1005.	67
Figure 5.21: Bending moment diagram resulting from the DSM toll when only vertical loads are applied	68
Figure 5.22: Shear force diagram resulting from the DSM toll when only vertical loads are applied	68
Figure 5.23: Normal force diagram resulting from the DSM toll when only vertical loads are applied	68
Figure 5.24: Resulting crack pattern for the frame modelled with JPSG1010 when only vertical loads are applied	69
Figure 5.25. Resulting crack pattern for the frame modelled with JPSG0810 when only vertical loads are applied	69
Figure 5.26: Resulting crack pattern for the frame modelled with JPSG1005 when only vertical loads are applied	69
Figure 5.27: Resulting curves with the maximum horizontal displacement achieved (a) and with a focus on the initial stiffness (b) for the frame modelled with JPSG1010.	71
Figure 5.28: Resulting curves with the maximum horizontal displacement achieved (a) and with a focus on the initial stiffness (b) for the frame modelled with JPSG0810.	71

Figure 5.29: Resulting curves with the maximum horizontal displacement achieved (a) and with a focus on the initial stiffness (b) for the frame modelled with JPSG1005.	72
Figure 5.30: Bending moment diagram resulting from the DSM toll when only horizontal load is applied	73
Figure 5.31: Shear force diagram resulting from the DSM toll when only horizontal load is applied	73
Figure 5.32: Normal force diagram resulting from the DSM toll when only horizontal load is applied	73
Figure 5.33: Resulting crack pattern for the frame modelled with JPSG1010 when only horizontal load is applied	74
Figure 5.34: Resulting crack pattern for the frame modelled with JPSG0810 when only horizontal load is applied	74
Figure 5.35: Resulting crack pattern for the frame modelled with JPSG1005 when only horizontal load is applied	74
Figure 5.36: Resulting curves for frame modelled with JPSG1010 on which different percentage of load P have been applied followed by H	77
Figure 5.37: Crack pattern at the end of the first step, when 50% of the vertical load is applied, for the frame modelled with JPSG1010	78
Figure 5.38: Crack pattern at the end of the two-step analysis for the frame modelled with JPSG1010	78
Figure 5.39: Resulting curves for frame modelled with JPSG0810 on which different percentage of load P have been applied followed by H	79
Figure 5.40: Crack pattern at the end of the first step, when 50% of the vertical load is applied, for the frame modelled with JPSG0810	80
Figure 5.41: Crack pattern at the end of the two-step analysis for the frame modelled with JPSG0810	80
Figure 5.42: Resulting curves for frame modelled with JPSG1005 on which different percentage of load P have been applied followed by H	81
Figure 5.43: Crack pattern at the end of the first step, when 50% of the vertical load is applied, for the frame modelled with JPSG1005	82
Figure 5.44: Crack pattern at the end of the two-step analysis for the frame modelled with JPSG1005	82

List of tables

Table 2.1: Physical and mechanical properties of soda-lime silicate glass	13
Table 2.2: Physical and mechanical properties of SentryGlas [Martens, 2018]	14
Table 2.3: Physical and mechanical properties of the different reinforcements in stainless steel reinforcements	15
Table 4.1: Comparative description of the characteristics and assumptions of the two different models	26
Table 4.2: Geometrical characteristics of the different cross sections	28
Table 4.3: Results of the experimental tests	30
Table 4.4: Comparison between experimental results and numerical simulation in ABAQUS	36
Table 4.5: Characteristics of the real cross sections and of the once implemented in Phyton	44
Table 4.6: Results of the DSM Tool	46
Table 4.7: Comparison between experimental results and numerical simulation in Phyton (DSM Tool)	48
Table 5.1: Numerical results coming from the numerical modelling with just vertical load applied	67
Table 5.2: Numerical results coming from the numerical modelling with just horizontal load applied	72
Table 5.3: Numerical results of the two-step analysis for the frame modelled with JPSG1010	77
Table 5.4: Numerical results of the two-step analysis for the frame modelled with JPSG0810	79
Table 5.5: Numerical results of the two-step analysis for the frame modelled with JPSG1005	81

List of abbreviations and symbols

Abbreviation	Meaning
ANG	Annealed Float Glass
CFRP	Carbon Fiber Reinforced Polymer
EFL	Equivalent Lateral Force
FRP	Fiber Reinforce Polymers
FTG	Fully Tempered Glass
GB	Acrylate Adhesive
GFRP	Glass Fibre Reinforced Polymer
HSG	Heat Strengthened Glass
SFRP	Steel Fibre Reinforced Polymer
SG	SentryGals®
UMAT	User-defined Material

Symbol	Meaning
A_g	Total area of glass
A_s	Area of 1 reinforcement
b	Total width of the cross-section
χ	Curvature
d	Diameter of the reinforcement
d_c	Displacement at formation of the first crack
d_f	Displacement at failure
α_T	Coefficient of thermal expansion
D_{lim}	Limit displacement define by the codes
Δ	Maximum horizontal displacement
$\Delta\varphi_c$	Relative rotation at formation of the first crack
$\Delta\varphi_f$	Relative rotation at failure
Δt	Time increment defined in ABAQUS Standard
E	Young's modulus
EI_{hybrid}	Hybrid bending stiffness
$\varepsilon_{y,s}$	0.2% Yield strain of steel
$\varepsilon_{t,s}$	Ultimate tensile strain of steel
$\varepsilon_{t,SG}$	Ultimate tensile strain of SentryGlas®
$f_{y,s}$	0.2% Yield strength of stainless steel
$f_{t,s}$	Ultimate tensile strength of stainless steel
$f_{t,SG}$	Ultimate tensile strength of SentryGlas®
$f_{t,k,gl}$	Characteristic tensile bending strength of glass
H	Horizontal load
H_{max}	maximum horizontal force
h	Total height of the cross section
$h_{g,e}$	Height of external glass pane
$h_{g,i}$	Height of external glass pane
h_s	Height of reinforcement
I_{hybrid}	Hybrid moment of inertia

k	Rotational stiffness k
M	Bending Moment and the rotation θ
M_c	Bending moment at the formation of the first crack
M_f	Bending moment at failure
n	Number of steps defined in the DSM Tool
n_f	Number of steps completed at failure
ν	Poisson's ratio
P	Vertical load
P_0	Final load impose in the DSM tool
P_f	Load at failure coming from the DSM tool
P_{max}	Vertical load at failure
ρ	Density
q	Behaviour factor
σ	Stress
T_{g1}	Glass transition temperature
$t_{g,e}$	Thickness of external glass pane
$t_{g,i}$	Thickness of internal glass pane
t_s	Thickness of the stainless-steel reinforcement
t_{SG}	Thickness of interlayer
θ_r	Relative rotation
v	Imposed horizontal displacement
v_f	Horizontal displacement at failure

Chapter 1 - Introduction

Among the materials employed in the field of construction, glass is unquestionably one that can be deemed relatively nascent. However, its utilization as a structural material has been progressively developing in recent decades.

Due to the inherent characteristics of the material, such as low tensile strength and brittle behaviour, glass has up to now served as a secondary element. Furthermore, due to the aforementioned characteristics and its inability to undergo ductile deformations, glass is considered an unsuitable material for structural purposes from a safety perspective.

Nevertheless, thanks to its transparency, glass holds significant potential for utilization in contemporary architecture.

To address the drawbacks associated with the mechanical properties of glass, efforts have been made in order to find a solution to these problems. Firstly, different thermal treatments can be applied to glass panes. These treatments, carried out at different temperatures, aim to increase the tensile strength of the glass. However, those do not improve the post-breakage behaviour.

To address this issue, a solution has been developed by fabricating glass panels through the lamination of alternating layers of glass panes and foils of resin interlayer. In these components, when one sheet fractures, the others continue to bear the load together with the interlayer. Specifically, what is created is a mechanism in which the glass panes bear the compressive stresses, while the interlayer handles the tensile ones. This approach effectively increases the material's strength after fracture.

Nevertheless, despite these implemented measures, the structural glass component might still experience total failure as a result of unforeseen circumstances.

In order to further improve the strength of the final configuration and to increase the aforementioned characteristics glass has been combined with other materials to create the so called "hybrid glass beams". In particular, the primary aim of these composite sections is to enhance the post-breakage behaviour, thereby ensuring a higher level of safety.

In this research, the glass panes are laminated with stainless steel reinforcements in the tensile and compressive zones. The cross-sections, as presented, are the outcome of research efforts that originated in the early 2000s. This type of lamination is referred to as "reinforced glass beams," although the configuration will also be employed in columns within this study.

It is important to highlight that glass is a material that has received limited study until now, which is why there are relatively few provisions in current codes. Nevertheless, given its potential, it

becomes imperative to develop and analyse novel concepts for employment within the field of civil engineering. To achieve these outcomes, conducting a well-detailed analytical study is crucial, particularly due to the mechanical behaviour of glass. However, employing experimental tests remains the optimal method to acquire accurate results. Once obtained, by modelling through software programs, this behaviour can be replicated within structural software, enabling detailed analyses without the necessity of physical specimens each time. Furthermore, once the numerical results aligning with experimental once, parametric studies can be conducted to comprehend the influence of specific parameters on the structure, such as reinforcement, dimensions, and external loads.

1.1 Aim

The continuous investigation into the rotational attributes of a hybrid glass joint prototype has produced encouraging findings concerning the post-fracture behaviour of these connections. Building upon the acquired findings, the subsequent phase involves an examination of the performance of a moment-resistance portal frame.

Moreover, recent experiments conducted on statically indeterminate structures have demonstrated that global system actions can be achieved through the formation of plastic hinges and stress redistributions. In addition, other research has indicated that activating membrane actions can provide additional strength to structural elements, thereby increase their safety.

The primary objective of this research is to analyse the stiffness of connections achieved through the lamination method that will be presented in the following chapters. The aim is to replicate this behaviour through an equivalent spring constant and to study the behaviour of sway frames. This aspect holds significant importance in recreating the accurate response of the structure when subjected to external loads. Modelling the connection as rigid or as hinged does not always replicate the correct behaviour and can lead to inaccuracies in internal reactions during operation. Once the spring constant has been determined for each examined lamination, it will then be applied to the nodes of the frame. In this scenario, the objective will not only be to analyse the behaviour of the connections but also to assess the impact of external loads.

1.2 Contents of this research

The presented Master's thesis centres on the investigation of connections within a glass structure. This first chapter serves as an introduction to the thesis work, elucidating the research motivations, objectives, and the structure along with its corresponding contents.

In the subsequent two chapters, a theoretical exploration is undertaken regarding the current state of research concerning glass structures and connection modelling. Particularly, Chapter 2 -delves into the contemporary utilization of glass in construction, outlining various types of manufactured beams that have been analysed in previous research. Furthermore, this chapter introduces and examines the materials that will be employed in the samples and numerical modelling.

In Chapter 3 -, the importance of accurate connection modelling is emphasized, both as a single element and within a frame structure.

Chapter 4 -, will explain and analyse the experimental results obtained by ir. Mirko Pejatovic and will provide the initial data to begin the numerical modelling. The latter will be executed in ABAQUS Standard and in Python, through a code based on the Direct Stiffness Method, called DSM tool.

The study of the frame will be done in Chapter 5 -, the characteristics of which will be introduced at the beginning of the chapter. In this scenario, there are no experimental results on which to base the research. Consequently, only the outcomes of the modelling conducted through software will be presented and analysed. Moreover, a parametric study will be conducted to analyse the influence that different configurations of external loads exert on the structure. First, the resistance to only vertical loads will be analysed, followed by the assessment of resistance to solely horizontal loads and lastly, a two-step analysis will be conducted. This, in particular, will be carried out in ABAQUS since the program offers the capability to perform two-step analyses, a feature that is not possible in the Python code.

Chapter 2 - State of art and materials

Before going in depth with the analysis performed in this study some aspects regarding glass and glass structures should be discussed.

Firstly, a general introduction into the employment of glass as a structural material will be done, and with this some advantages and drawbacks of his application will be listed.

After, the concept of hybrid glass beams will be explained. In this section the most common typologies developed nowadays are described by means of examples taken from the literature. In particular, the concept of composite glass beams and reinforced and post-tensioned glass beams. The examples chosen aim to recreate a sort of timeline of how the research have developed toward the cross section that are then used in this research.

From this, the materials employed in this thesis are discussed, namely Annealed Float Glass, SentryGlas® and Stainless steel AISI304.

At last, an introduction to previous research done for the modelling of the glass connection and glass frames will be reported.

2.1 Structural use of glass

Within modern architecture the utilization of glass as a construction material is progressively on the rise. In addition to its conventional role as an infill panel, glass has undergone a transformation in recent decades, assuming the role of a load-bearing material for diverse structural components, including beams, columns, and walls. These structural constituents find application in a variety of contexts, such as roof structures, façade configurations, conservatories, footbridges, and staircases. The main disadvantages concerning the use of glass are mainly related to its brittle material behaviour. Glass is prone to sudden and unexpected failure and for this is not seen as a safe material for buildings. This vulnerability arises from the material's inability to redistribute stress through local yielding. As a result, glass is highly sensitive to peak stresses, which can cause it to crack under excessive localized pressure. Once a crack appears, it typically propagates unimpeded, and the resulting shards have extremely sharp edges that pose an immediate hazard to individuals in the vicinity. Additionally, although glass is relatively strong in compression, it exhibits weakness in tension.

To address the issue related with the unsafe structural behaviour of glass, two measures are typically employed for structural glass elements. Firstly, a tempering process is performed to increase the surface tensile strength. This increment in strength subsequently fortifies the

resistance of the element. Secondly, foil or resin interlayers are employed in the assembly of components composed of multiple layers of glass, resulting in what is commonly referred to as laminated glass. In the event that one of the glass layers fails, the remaining layers remain capable of bearing the load. Both measures are directed towards diminishing the likelihood of complete failure, with the ultimate aim to avoid the collapse of the structural glass element.

However, even with the implementation of these measures, the potential for total failure of the structural glass component remains, primarily due to unforeseen occurrences. The numerous glass layers within the component could, for instance, experience cracking resulting from severe or repeated impacts, or from simultaneous high localized stress affecting all glass layers due to assembly errors, as an example at the supports or joints. Consequently, it is highly suggested to incorporate supplementary safety measures or safety strategies aimed to increase the redundancy of structural glass components.

Another aspect that needs to be highlighted is related to the type of glass used in the lamination. First, a glass pane that does not undergo any treatments takes the name of annealed float glass. If it undergoes the tempering process it can yield to two types of glass: heat strengthened glass, which is subjected to a tempering process at lower temperatures when compared with the second typology, the tempered glass. This last typology presents the higher tensile strength in comparison with the other two typologies, however, when it breaks, it suddenly fractures in small elements. From this, annealed laminated glass and heat strengthened laminated glass exhibit superior performance in terms of post-breakage behaviour, in contrast to tempered laminated glass. This discrepancy arises from the relatively unlikely occurrence of cracks appearing at precisely the same locations within the various layers of annealed or heat-strengthened glass. Such irregularity in the cracking pattern creates an overlap of intact, larger glass sections that contribute to residual rigidity and constrained deformation.

An alternative approach to enhance post-breakage capacity involves incorporating diverse structural materials such as steel, concrete, wood, carbon fibre elements, and post-tensioned steel cables. These additional components function in conjunction with the glass elements to create a composite system. It is essential to underscore that the establishment of suitable connections between these components holds paramount importance in realizing the intended capacity. This, in conjunction with the utilization of laminated glass units, necessitates adjustments to the element design, thereby generating robustness at the component level as required in the building codes.

2.2 Hybrid glass beam

Based on the insights previously mentioned, it can be deduced that glass is a viable option for structural applications when it is integrated with lamination and supplementary materials to create hybrid glass beams. The objective of the reinforced glass beam concept is to establish substantial post-breakage resistance for structural glass beams.

At first, this was realized by incorporating reinforcement at the tensile zone of the beam. Afterwards, other research that have been conducted highlighted how the addition of reinforcing elements in the compressed zone can create even greater strength in the structural elements. These supplementary materials, which encompass concrete, timber, stainless steel, Fiber Reinforced Polymers, among others, contribute post-fracture strength and ductility after glass breakage. The reinforcement is generally linked to the glass element via an intermediary bonding layer in order to avoid surface stresses.

Over the years, a diverse array of hybrid glass beams has been developed and subjected to investigation. Among these concepts, in the work of Martens et al. [Martens, 2018] a distinction is made between two main categories, the composite glass beams and the reinforced and post-tensioned glass beams. However, it should be noted that in some cases, the beam concepts developed represent an intermediate solution between the two types.

2.2.1 Composite glass beams

In the scenario of composite glass beams, the secondary material constitutes a significant portion of the beam's cross-section, typically exceeding 25%, and plays an active role in supporting the load-carrying function of the structural element. These typologies predominantly manifest as T and I-section beams, with the central web composed of laminated glass, while the flanges are constructed from a distinct material. The cohesion between these elements is established through the utilization of adhesives or a bolted connection system. Furthermore, other conceptualizations have been developed where the beam's sections are stratified, alternating between layers of glass and the complementary material.

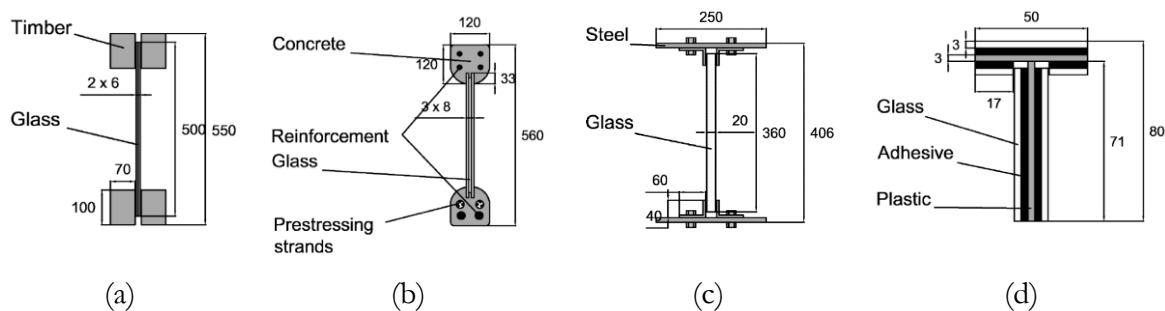


Figure 2.1: Examples of composite glass beams [Martens, 2018]

2.2.2 Reinforced and post-tensioned glass beams

In the reinforced and post-tensioned glass beams category, minor quantities of alternative material are introduced into the cross-section of the beam, generally less than 10%. These additions gain functionality mainly during the post-fracture phase in the case of reinforced glass beams. Nevertheless, they modify the load-bearing characteristics of the glass section within the initial linear elastic phase. As an example, post-tensioned glass beams may exhibit a higher initial glass fracture load. In this category, the supplementary material generally preserves the original shape of the beam section. These latter concepts are closely related to the principles of reinforced and post-tensioned concrete beams.

In the context of reinforced glass beams, the activation of the reinforcement occurs following fracture. It operates as a fracture bridge, effectively transmitting tensile forces among various segments of the fractured glass laminate. Consequently, the internal resisting moment in beams undergoing bending remains intact, facilitated by the lever arm between the tensile forces within the reinforcement and the compression zone where the glass is still active.

Analysing the post-tensioned glass beams, the utilization of steel tendons serves to apply a compressive load onto the glass beam, thus augmenting its tensile capacity. Primarily, this increases the initial strength against failure. As loading progresses, the initially imposed compressive stresses are gradually offset within the tensile zone until reaching a point of zero stress. Continued loading results in the development of tensile stresses within the glass, inevitably leading to glass fracture. To achieve a ductile post-fracture behaviour, the responsibility of carrying these tensile stresses shifts to the prestressing strands, aiming to establish an internal resisting moment comparable to the scenario observed in reinforced glass beams.

In both these concepts, the selection of appropriate reinforcement or post-tensioning material, coupled with a well-designed section, holds the potential to produce structural glass beams characterized by secure failure behaviour, as depicted in Figure 2.2.

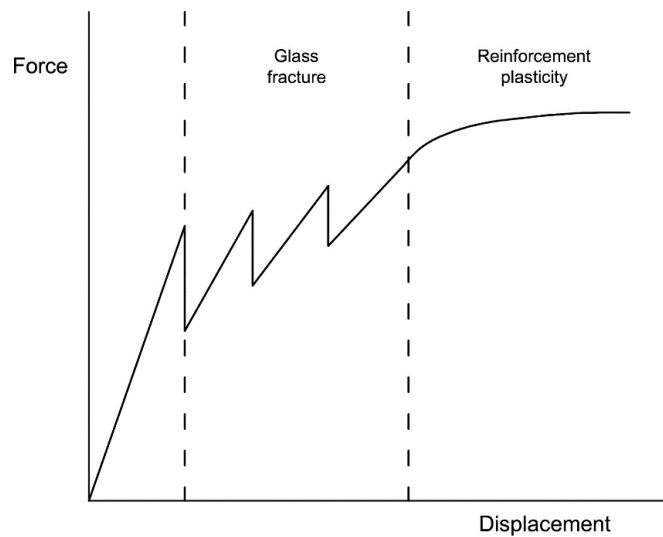


Figure 2.2: Desired load-carrying behaviour for structural glass beams [Martens et al., 2018]

2.2.2.1 Steel reinforced glass beams

The cross sections that will be analysed in this study are the results of years of research began back in the early 2000. The explorations, pioneered by Veer et al. and subsequently advanced by Louter et al., demonstrated the attainment of satisfactory post-fracture behaviour and ductility. These findings prompted the inference that optimal outcomes could be achieved through the synergistic utilization of an expansive bonding area between glass and reinforcement, in conjunction with a robust adhesive exhibiting notable rigidity.

However, it is important to acknowledge that various environmental factors have the potential to influence the adhesive bond. Considering this, Louter embarked on the development of a pragmatic glass beam concept and developed a study on the impact of those aspects. At first, he started to study the cross section with the hollow reinforcement and the different interlayer typologies, to understand the effect of the external factors, such as temperature, thermal cycling, humidity, and load duration [Louter, 2011]. After, he moved on the effect of glass type, reinforcement percentage and scale factor.

The experimental setup involved subjecting three-layer ANG beam specimens (Figure 2.3), measuring 1500 mm in length, to four-point bending tests.

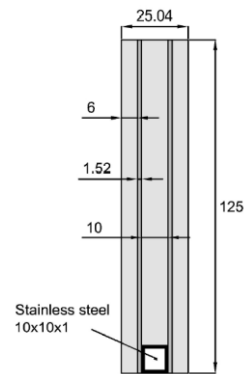


Figure 2.3: Steel-reinforced glass beam section [Martens et al., 2018]

To study the effect of the interlayer typology, in addition to an adhesively bonded beam specimen utilizing acrylic adhesive, Louter explored the feasibility of employing SentryGlas® (SG) as a bonding material.

The load-deflection diagrams for all three temperatures tested, -20, +23, and +60°C, thermal cycling, and humidity conditions are depicted in Figure 2.4. On the left (Figure 2.4 (a)), are reported the curves for specimens utilizing acrylate adhesive (referred to as 'GB'), and on the right for SG-laminated specimens (Figure 2.4 (b)). The findings led to the conclusion that the SG-laminated beams exhibited elevated levels of post-fracture strength and ductility across all tested temperatures, subsequent to thermal cycling and exposure to humidity.

Furthermore, these beams demonstrated sustained safety performance under prolonged loading conditions, even though a degree of creep was observed. For load durations spanning up to 15 months, these beams displayed the capacity to withstand loads reaching up to 80% of their projected ultimate failure load.

However, the effects of humidity and load duration were not examined for these beams. The primary factor attributing to the distinct behaviour was the extent of reinforcement debonding. Notably, the GB-laminated beams exhibited excessive debonding, while the SG-laminated specimens displayed only localized debonding.

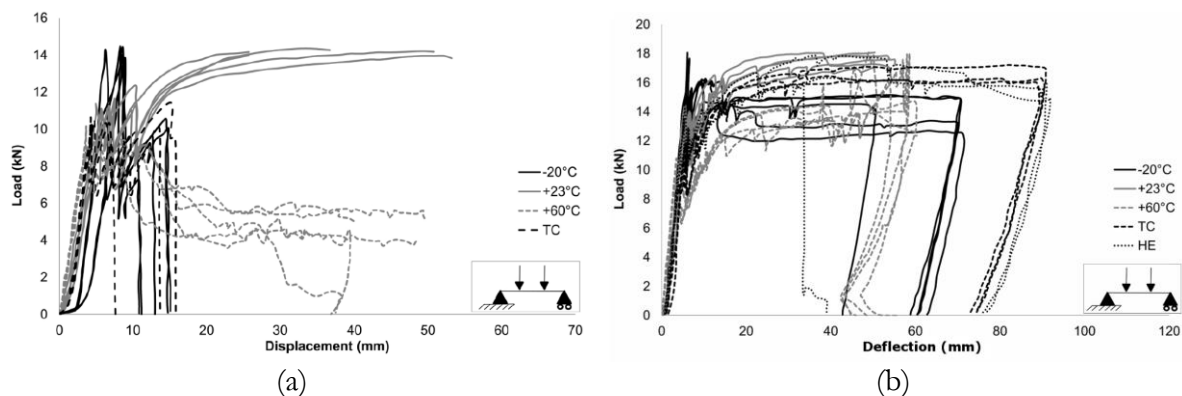


Figure 2.4: Load-deflection diagrams for beam specimens GB-interlayer (left) and SG-interlayer (right) [Martens et al., 2018]

Once the suitable and practical geometry was defined, the effects of reinforcement percentage and beam size were subsequently explored [Louter et al., 2012b]. To this end, the hollow steel section was substituted with a solid steel section and a scaled version of the SG-laminated beam, both illustrated in Figure 2.5.

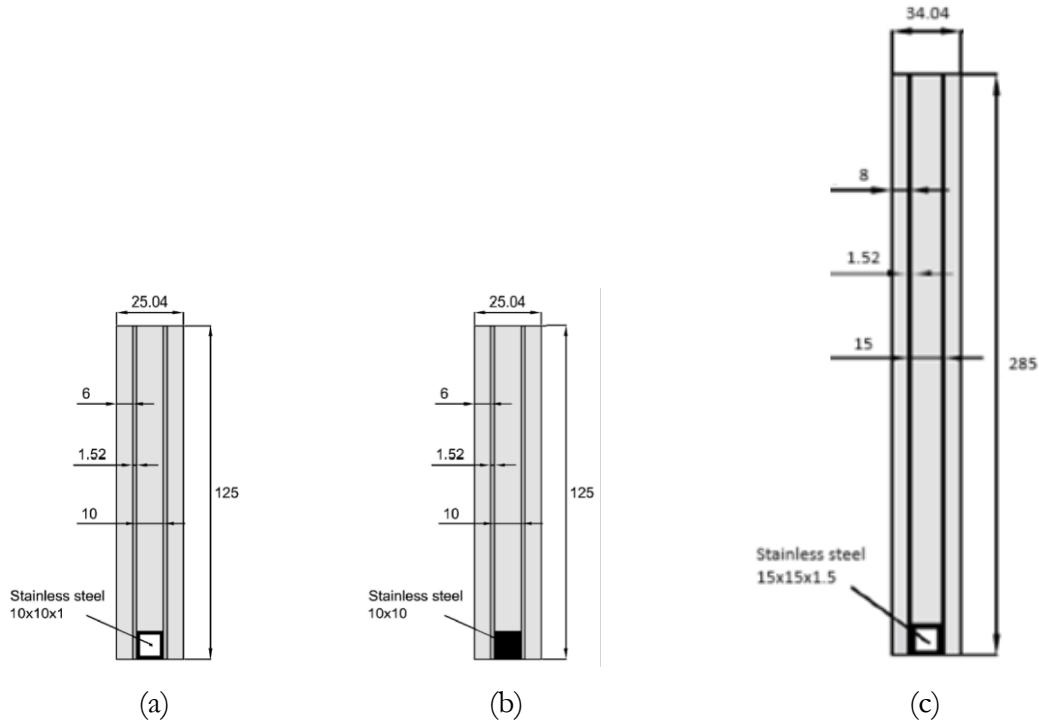


Figure 2.5: Reference cross section (a), cross sections investigated for the reinforcement percentage (b) and scale factor (c) [Martens et al., 2018]

The solid reinforced beam specimen subjected to a four-point bending test exhibited higher post-fracture strength and stiffness compared to the reference section. This outcome was attributed to the higher tensile capacity. Additionally, reduced fracture heights were observed, leading to a larger compressive zone. Conversely, the large-scaled beam (Figure 2.5 (c)) presented a behaviour similar to the reference beam, implying that beam size had only a limited impact on post-fracture behaviour.

The resulting graphs of this study are reported in Figure 2.6, those can be compared with the resulting graph of the reference cross section reported in Figure 2.4.

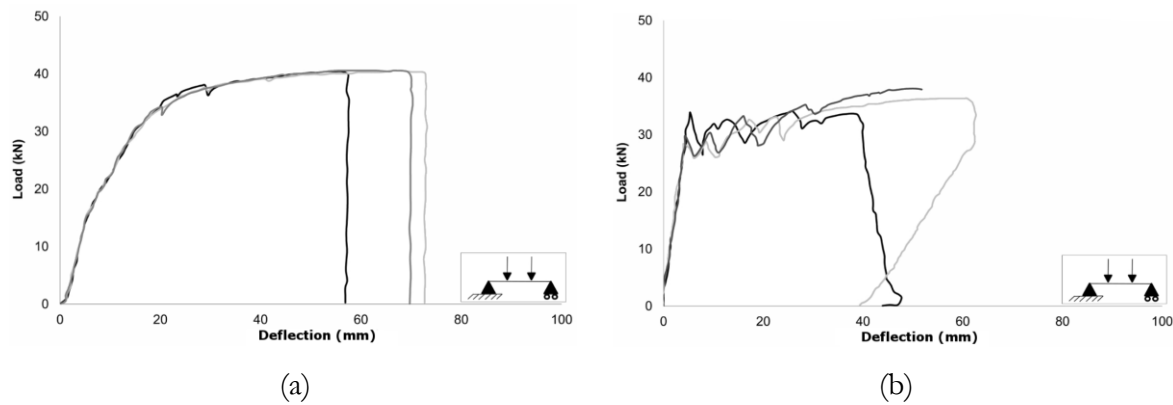


Figure 2.6: Load-displacement curves for the cross section with solid reinforcement (a) and larger-scaled section (b) [Martens et al., 2018]

Subsequent tests on the large-scaled beams, given their significantly greater slenderness compared to the reference beams, involved investigating lateral-torsional buckling. These tests indicated minimal lateral displacement solely during the post-fracture stage. Notably, glass fracture influenced the lateral stiffness of the beam. Although global lateral stability was considered non-critical for the examined beam, it was suggested that beams with higher slenderness must undergo thorough lateral instability testing.

A final aspect of interest regards the selection of the glass type. Louter et al. created three beam specimens, employing the reference cross section, each with a different glass type: annealed float glass (ANG), heat-strengthened glass (HSG), and fully tempered glass (FTG). These specimens were subjected to four-point bending tests [Louter et al., 2012b]. The load-deflection diagrams resulting from these test (Figure 2.7) led to the conclusion that glass type not only influences the initial failure strength but also impacts post-fracture strength and ductility.

The beams utilizing FTG demonstrated higher initial failure strengths but slightly lower post-fracture strength levels than their ANG and HSG counterparts. Regarding post-fracture ductility, it was noted that both HSG and FTG beams exhibited lower ultimate deflections compared to the annealed variant. Increased fracturing in HSG beams and complete fragmentation in FTG beams during glass fracture significantly compromised their sections, causing the compressive zone to fail earlier than in ANG beams.

In conclusion, opting for stronger glass types may offer advantages in terms of initial failure strength, but such a choice could lead to a less optimal post-fracture response compared to using ANG, as already stated previously at the beginning of the chapter. However, future research avenues might explore the incorporation of multiple glass types within a single beam [Martens et al., 2018].

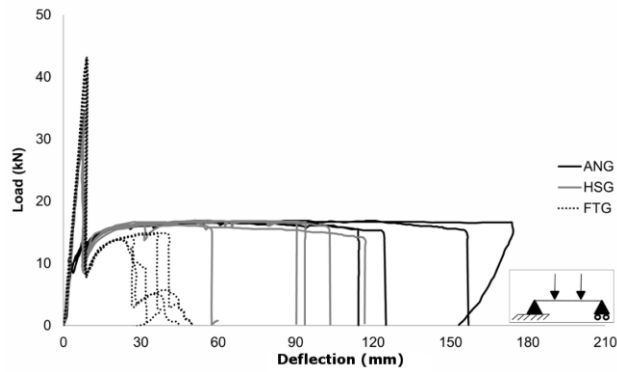


Figure 2.7: Load-displacement curves with different glass types [Martens et al., 2018]

2.2.2.2 FRP reinforced glass beams

Similar concepts developed for the steel reinforced glass beams can be developed by means of Fiber Reinforce Polymers (FRP). The incorporation of FRP as reinforcement holds promise due to its notable characteristics, including low weight and impressive structural strength. The fibres that are commonly used are carbon fibre reinforced polymer (CFRP), glass fibre reinforced polymer (GFRP), and steel fibre reinforced polymer (SFRP).

FRP, commonly manufactured through pultrusion, allow for diverse cross-sectional shapes achievable through stamp creation. Orlando et al. conducted four-point bending tests on laminated glass pane beams combined with CFRP pultruded round bars, adhered to the glass via bi-component resins [Orlando et al., 2009]. The cross section is reported in Figure 2.8.

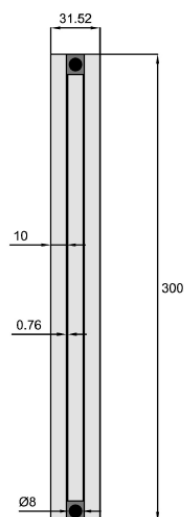


Figure 2.8: Cross section used by Orlando et al. [Martens et al., 2018]

Comparison of load-deflection curves for the different configurations is presented in Figure 2.9. Test results indicated that optimal mechanical performance was attained with deformed bars affixed to the glass using polyester resin, accompanied by an epoxy primer. This combination yielded maximum residual strengths amounting to 44% of the peak load. Conversely, specimens involving smooth bars and deformed bars bonded with epoxy resin led to instantaneous debonding of the FRP bars upon failure, resulting in negligible post-fracture strength.

In contrast, beams employing deformed bars, polyester resin and primer experienced collapse due to tensile bar failure.

A conclusion that was found in this work is that, in order to achieve better post-breakage performances, a more robust or larger reinforcement section should be adopted. However, the latter approach would mandate an increase in the thickness of the central glass pane.

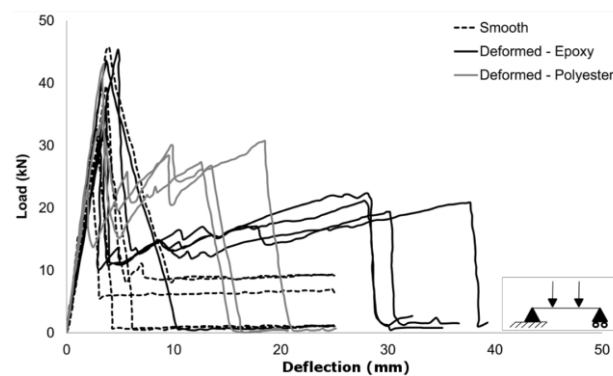


Figure 2.9: Load-deflection curves of the FRP reinforced beams from Orlando et al. [Martens et al. 2018]

This concept presented above in Figure 2.8 is similar to the one that will be analysed later on in the study. However, the configuration will present double stainless steel as reinforcement elements and also different dimensions. This is the result of the different studies which proved that the steel reinforcement gives higher performances.

2.2.2.3 Post-tensioned glass beams

The last typology of hybrid glass beams is represented by the post tensioned beams. Louter et al., leveraging insights from prior investigations on reinforced and post-tensioned concrete beams, embarked on the development and examination of a post-tensioned glass beam configuration. The beam design consisted of a three-fold SG-laminate of ANG panes, integrated with stainless steel rods affixed at the upper and lower sections of the beam [Martens, 2018]. The section is depicted in Figure 2.10.

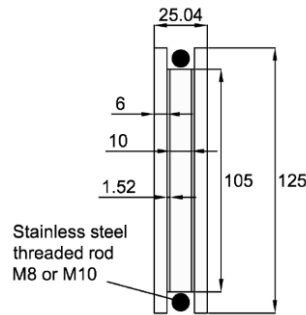


Figure 2.10: Cross section of the post-tensioned glass beam in Louter et al. 2014 [Martens, 2018]

Two distinct diameters of steel rods, accompanied by corresponding pre-loads, were scrutinized (M8 - 50 kN and M10 - 66.7 kN).

Beams featuring larger pre-loads and steel rod diameters exhibited heightened initial and ultimate failure strengths. Both these beams reached the yield phase, contributing to substantial post-fracture ductility. However, the ultimate collapse was marked by an explosive occurrence attributed to the early failure of the compressive glass zone. The resulting graph is reported below in Figure 2.11.

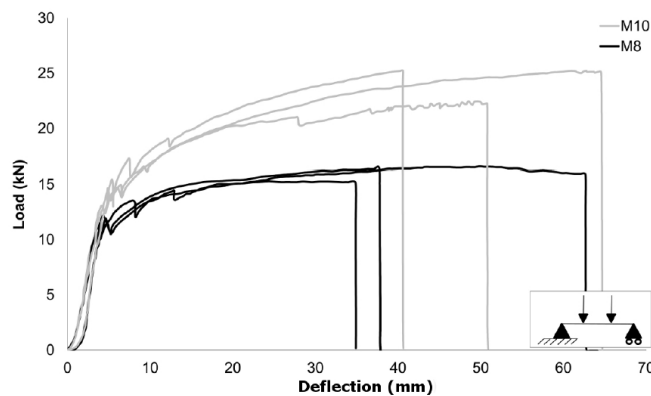


Figure 2.11: Load-deflection curves related with the post tensioned glass beam Louter, Cupac et al. [Martens et al., 2018]

An interesting analysis can be performed once these results are compared with the once from the reference cross section of steel reinforced glass beams (Figure 2.3 and Figure 2.4 (b)).

The post-tensioned glass beams notably achieved greater initial failure loads, up to 80% higher. Furthermore, the M8 and M10 post-tensioned beams attained average post-fracture performances comparable with the once of the reinforced glass beam. Despite the M8 post-tensioned glass beam incorporating more steel, its post-fracture performance was inferior to that of the reinforced glass beam. In terms of deformations, the reinforced glass beam exhibited significantly greater deformation values, twice those observed in the post-tensioned glass beams. Finally, the reinforced glass beams generally avoided explosive failure behaviour.

Collectively, this analysis leads to the conclusion that the advantages of post-tensioned glass beams are primarily evident during the initial failure stage. In the post-fracture phase, reinforced glass beams displayed more favourable behaviour.

2.3 Materials used in this research

In this chapter the materials employed in this research will be described. These materials are the result of the abovementioned research performed and discussed in the previous chapters. Nevertheless, the optimal configuration of the lamination of the hybrid glass beam under analysis needs to be further investigated. In fact, different stainless-steel sizes presenting different mechanical characteristics will be analysed. The materials that will be described below are Annealed Float Glass (ANG), SentryGlas® for the interlayer and Stainless Steel AISI304 as reinforcement.

2.3.1 Annealed Float Glass

The application of annealed float glass comes from his high post-fracture behaviour when employed in laminated configurations.

Nowadays, the most common procedure to manufacture glass is the float process. This accounts for the 90% of the global production of glass. As shown in Figure 2.12, the raw material is heated up and then pass through a melter, a tin bath and as last to an annealing lehr. In this last step, the glass pane is cooled down and thanks to rollers in the tin bath the desired thickness is obtained. From this process the final product takes the name of annealed float glass.

When a glass pane comes out from the manufacturing process, it passes through an automated systems which inspect the glass for visual defects and flaws that will be subsequently removed during the cutting process. This is important since the presence flaws on its surface represents weak points where the stress can concentrate, and crack propagation can begin.

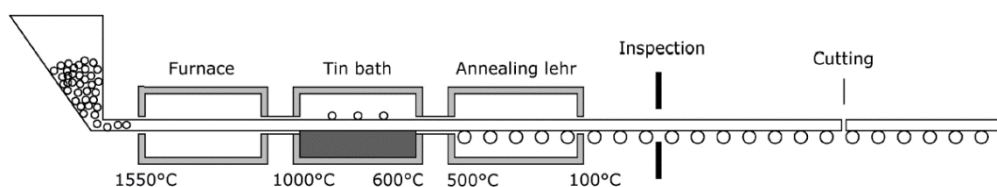


Figure 2.12: Schematic representation of the float glass process [Martens, 2018]

The physical and mechanical properties of ANG are reported in Table 2.1. Notably, glass density is similar to the one of concrete, while its Young's modulus mirrors that of aluminium. Glass is characterised by a linear-elastic, isotropic behaviour and manifests brittle failure, as depicted in Figure 2.13. Due to its incapability of stress redistribution through plastic deformation, glass displays high vulnerability to stress concentration.

Table 2.1: Physical and mechanical properties of soda-lime silicate glass

Property	Symbol	Unit	Value
Density	ρ	[kg/m ³]	2500
Young's modulus	E	[MPa]	70000
Poisson's ratio	ν	[-]	0.23
Characteristic tensile bending strength	$f_{t,k,gl}$	[MPa]	45
Coefficient of thermal expansion	α_T	[10 ⁻⁶ /K]	9

Has to be pointed out that the characteristic glass bending strength, contrary to being a constant material property, varies based on a multitude of factors. In particular, it is function of the surface flaws and the finishing of the edges, together with other parameters. In fact, the values follow a so-called Weibull distribution.

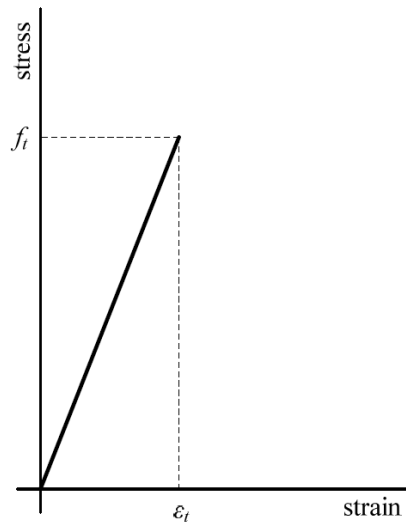


Figure 2.13: Schematic representation of the stress-strain diagram of glass in tensile loading [Loter 2011]

2.3.2 SentryGlas®

When a laminated glass is composed, a certain number of glass panes are attached together by means of an adhesive which takes the name of interlayer. In this study, the material chosen is SentryGlas®. This is a type of semi-crystalline thermoplastic polymer sheet material that undergoes a curing process within an autoclave.

One of the significant advantages of SentryGlas is its robust strength properties and a high glass transition temperature, around 55°C. Thanks to this, it generally results in a more favourable behaviour after fractures compared to beams laminated with Poly Vinyl Butyral (PVB) interlayers, the most common typology employed nowadays in the lamination of glass.

The physical and mechanical attributes of SG are influenced by time and temperature. Research performed by Callewaert described the mechanical properties of SG across various temperatures and load durations. From this investigation, a set of practical values within specific ranges was derived. The temperatures studied in his research were 23°C and 60°C, however in this study the values that have been selected are the once related with the lower temperature.

Those values are reported in Table 2.2. Important to highlight is that the Young's modulus and the Poisson's ratio were defined for a load duration of 30 minutes, based on the research of Callewaert [Martens, 2018].

Table 2.2: Physical and mechanical properties of SentryGlas [Martens, 2018]

Property	Symbol	Unit	Value
Density	ρ	[kg/m ³]	950
Young's modulus	E	[MPa]	110.53
Poisson's ratio	ν	[-]	0.49
Ultimate tensile strength	$f_{t,SG}$	[MPa]	34.5
Ultimate tensile strain	$\varepsilon_{t,SG}$	[-]	400
Glass transition temperature	T_{g1}	[°C]	55÷60

2.3.3 Stainless steel

The reinforcement applied for the specimens and numerical modelling is stainless steel AISI304. This choice has been dictated by a series of advances compared with other metals. The nature of stainless steel ensures the preservation of both mechanical and aesthetical qualities over time. Furthermore, it possesses a relatively high yield strength, ultimate strength, and strain, critical attributes for facilitating the development of safety mechanisms like post-fracture capacity, stress redistribution via plastic hinge formation, and membrane action.

Stainless steel also presents a coefficient of thermal expansion similar to the one of glass, setting it apart from other commonly used metal products. The specific designation for this steel is X5CrNi18-10, categorized within the family of austenitic stainless steels.

Later on, it will be shown the different typologies of cross sections. All three present solid reinforcement, however each of them possess different dimensions, 10 x 10 mm, 8 x 10 mm and 10 x 5 mm, being the first number the height of the reinforcement and the second one the width. The mechanical and physical properties of the three reinforcements are reported in Table 2.3. While in Figure 2.14 are reported the stress-strain diagrams that were defined in the laboratory before the experiments presented in chapter 4.2.

Table 2.3: Physical and mechanical properties of the different reinforcements in stainless steel reinforcements

Property	Symbol	Unit	Value		
			10x10 mm	8x10 mm	10x5 mm
Density	ρ	[kg/m ³]	7900	7900	7900
Young's modulus	E	[MPa]	180000	180000	180000
Poisson's ratio	ν	[-]	0.30	0.30	0.30
0.2% Yield strength	$f_{y,s}$	[MPa]	670	360	310
0.2% Yield strain	$\varepsilon_{y,s}$	[-]	0.0037	0.0020	0.0017
Ultimate tensile strength	$f_{t,s}$	[MPa]	822	683	611
Ultimate tensile strain	$\varepsilon_{t,s}$	[-]	0.215	0.388	0.449
Coefficient of thermal expansion	α_T	[10 ⁻⁶ /K]	16	16	16

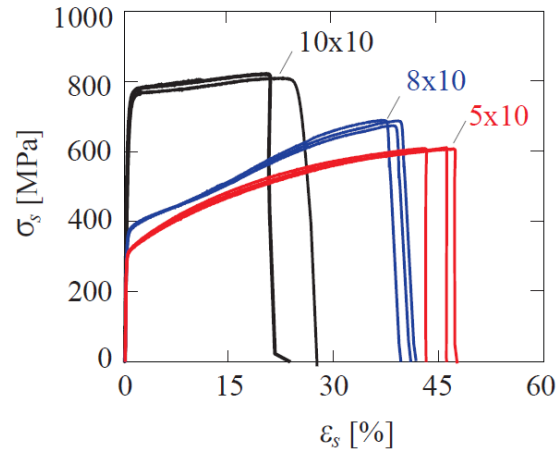


Figure 2.14: Stress-strain diagrams of the three stainless steel reinforcement

Chapter 3 - Connection and frame modelling

3.1 Connection modelling

In the research developed by Huang, W. (2017) is made reference to previous works done by Snijder concerning the correct representation of the stiffness of glass beam to column connection. This connection is not completely articulated, as a pinned connection, neither is completely stiff, as the case of clamped connection. Besides, it presents a semi-rigid behaviour.

The stiffness of a connection significantly influences the load-displacement characteristics of a structure. Opting for a semi-rigid joint linking a beam and column results in reduced end-of-beam moments compared to a fully rigid joint. This reduction in design moment can subsequently lead to a lower beam's section modulus, opening up possibilities for cost savings. In fact, among the design alternatives, the semi-rigid approach emerges as notably cost-effective when contrasted with conventional pinned and rigid joints.

For an optimal design, a comprehensive analysis of rotational stiffness and moment resistance is imperative. This need for assessment has been highlighted by Ferdous (2014) and Simões (1996), emphasizing the importance of evaluating these factors to achieve an ideal outcome. [Huang, W., 2017].

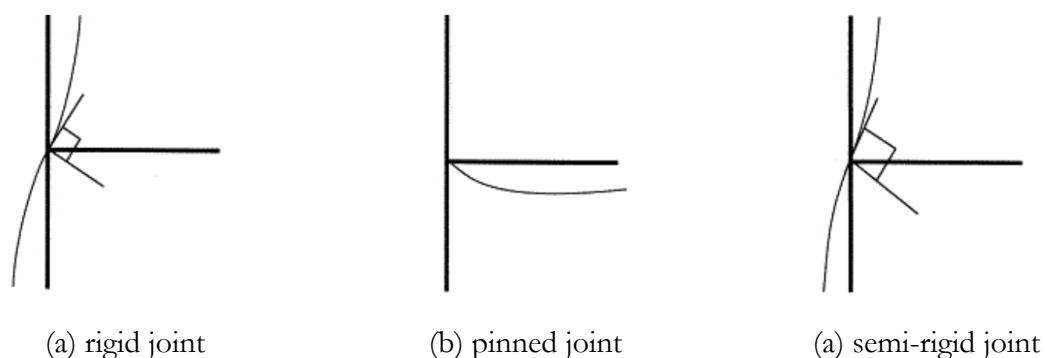


Figure 3.1: Different joints according to rotational stiffness [Huang, W., 2017]

As anticipated, traditionally, the joints connecting beams and columns have been treated as either ideally rigid connections or, although not truly rigid, they have been regarded as pinned. This approach often introduces an additional moment, consequently leading to unnecessary structural over-design.

In finite element analysis, a common simplification is to consider the semi-rigid joint as either rigid or pinned, facilitating straightforward calculations. However, for enhanced accuracy in analysis, it is crucial to model the connection according to its moment-rotation curve, since it represents the rigidity of the real connection.

The advantages coming from adopting semi-rigid connections are manifold. Modelling the connection more accurately offers an increased ability to predict structural behaviour with improved accuracy. Furthermore, it eliminates the concern of over-design in connections, optimizing material usage. Lastly, implementing semi-rigid connections has the potential to reduce the beam's height, contributing to more efficient structural design.

The connection can be modelled assigning to it a certain rotational stiffness k , that is represented by the ratio between the applied bending moment M and the relative rotation θ_r . This is also what will be done in the context of this research.

$$k = \frac{M}{\theta_r}$$

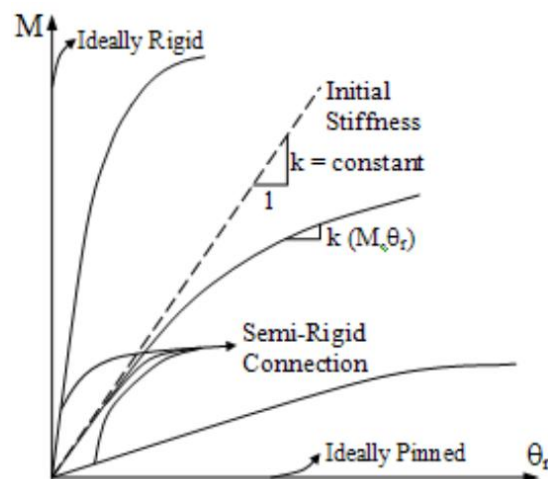


Figure 3.2: Structural behaviour of connections [Huang, W., 2017]

3.2 Frame analysis

In this research, once the study of the behaviour of the individual connection has been conducted, it will be extended to a frame whose geometry will be described in Chapter 5 -.

Literature does not contain many references regarding the influence that connection stiffness can have on the frame's response modelled with glass. However, below are presented two analysis approaches related to this modelling. The first approach is more classical, involving the study of various parameters that influence the response of a frame. The second approach is more closely linked to the seismic design of a glass frame and its dissipation capacity.

3.2.1 Parameters influencing the response

In the previous chapter, the significance of properly defining the level of stiffness of column-beam connections was emphasised. The response of a frame to external loads is influenced by the dimensions of the elements, cross-section sizes, the stiffness of the connections, and the materials used. In particular, the level of rigidity of the connections has an impact on the bending moment diagram. More precisely, rigid connections cause the bending moment to increase at the connection points and decrease at midspan, whereas hinged connections increase the moment at the centre of the beam and make it smaller at the ends (Figure 3.3).

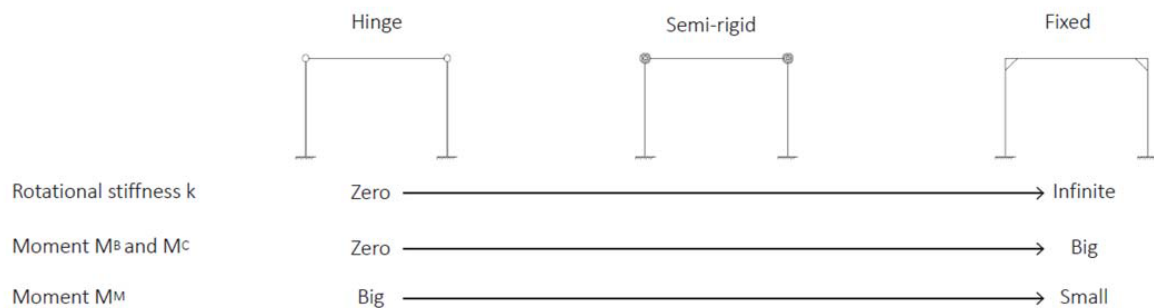


Figure 3.3: Relationship between the rigidity of the connections (k) and the effect on the bending moment [Huang, W., 2017]

Within the context of this research, the influence of frame dimensions will not be analysed. What will be examined in greater detail is the influence of connection stiffness, modelled through springs, and different sizes of stainless steel used as reinforcement. Afterwards, also a parametric study concerning the external loading will be performed.

3.2.2 Energy-based analytical model

In the study conducted by M. Santarsiero et al. the glass portal frame was considered as a part of a much complex 3D building. The system was considered to be situated in a seismic zone and the analysis was performed according to the Equivalent Lateral Force (EFL) method. However, following this procedure applied for concrete, steel and timber structure, some issues related with the design raised.

This study suggests solutions for the correct definition of the seismic dissipation capacity based on the forces and moments acting on a system at yielding and at failure. However, the study focuses more on the base-joint connection and the formation of plastic hinges in the steel angle brackets used to anchor the structure to the foundation (Figure 3.4).

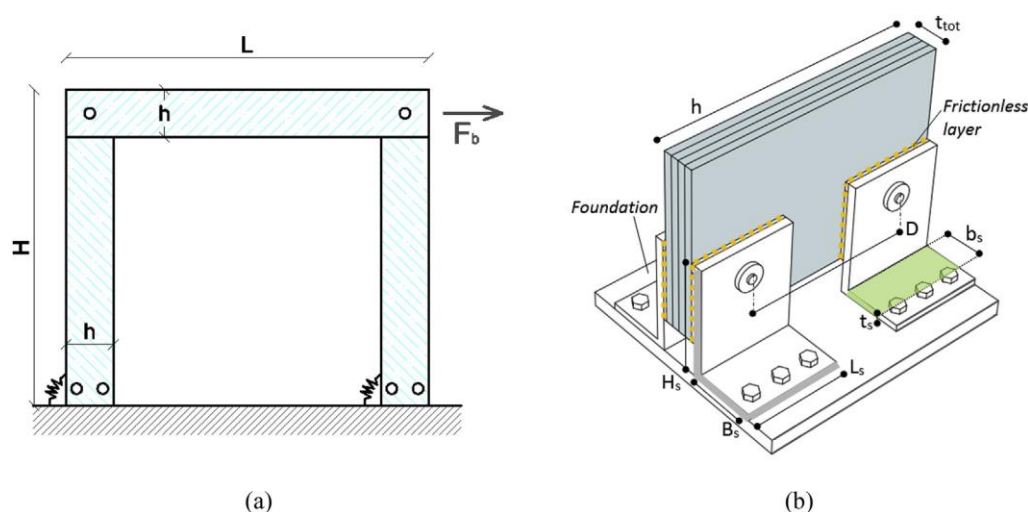


Figure 3.4: Schematic representation of (a) the structural glass frame object of analysis, with (b) detail view of a typical push-pull moment connection at the base of the columns.

[M. Santarsiero, et al 2019]

In the context of a seismic design two main parameters are the once which are employed, namely the behaviour factor q and the maximum horizontal displacement Δ that the structure can do.

The behaviour factor defines the dissipative level of a system. The value of this parameter for low dissipative structure is 1.5, while it can take values which go from 2 up to 5 for the classical materials employed in buildings. In particular, higher dissipative values are related with steel structures. Due to the inherent characteristics of glass, this requirement often leads to the adoption of a conservative assumption, taking a behaviour factor $q=1$. However, this approach results in an extremely cautious structural design and inefficient material utilization.

From the Ultimate Limit State collapse prevention, the maximum drift of vertical elements must satisfy the inequality for which $\Delta \leq D_{lim}$. This displacement limit is reported in the codes for steel, concrete and wood frames, but no specific limits are reported for glass structures. However,

this stands in contrast to the explicit demand in conventional glass structure design, where the glass must endure seismic forces without any damage, like cracking. The specified limits are acknowledged as potentially occurring within the "collapse prevention" condition, alongside significant damage to the primary components. Furthermore, even for glass members not directly part of earthquake-resistant structures but still capable of affecting occupant safety, collapse must be averted.

Chapter 4 - Analysis of the connection

4.1 Overview

The following chapter focuses on the study of the behaviour of the corner connection that could be realised between a column and a beam.

The research is based on experimental curves that were previously obtained by Ir. Mirko Pejatovic in which three different lamination configurations have been tested. The latter will be described in the next part.

For what concerns the numerical analysis, first a 3D model was developed in ABAQUS Standard in which all the different elements have been assembled recreating as accurate as possible the real lamination and behaviour of the specimen under analysis. Afterwards, the connection has been modelled through a Python code, called DSM tool, with the aim to verify if the spring constant defined from the experimental tests was recreating in the correct way the behaviour of the connection.

In Figure 4.1 are depicted the two model geometries and the boundary conditions applied, while in Table 4.1 a comparison of the characteristics and the assumption of the two models is reported.

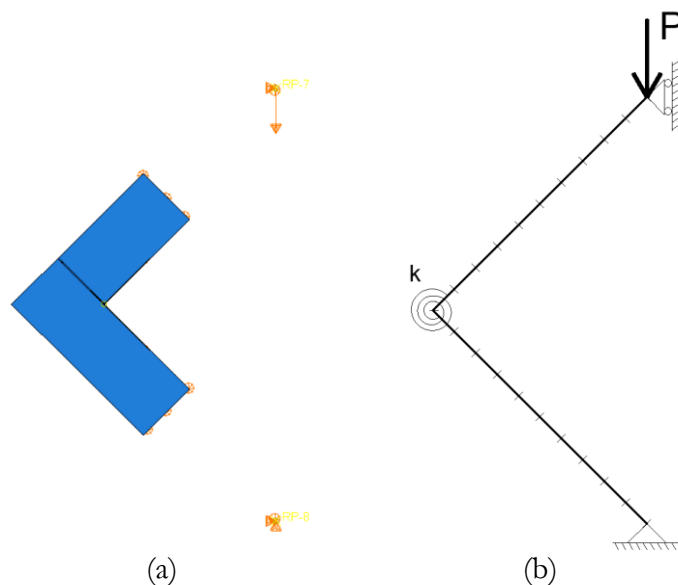


Figure 4.1: Model in ABAQUS (a) and model in DSM tool (b)

Table 4.1: Comparative description of the characteristics and assumptions of the two different models

	ABAQUS	DSM Tool
Model definition	3D model	1D model
Cross-section	Half cross section has been modelled assembling together each element to recreate the real geometry.	Definition an equivalent geometry in order to respect the hybrid bending stiffness.
Geometry	Just a portion has been modelled in order to improve the accuracy of the mesh and of the results. Boundary condition have been applied by means of tie constraint.	The two elements composing the structure have been divided in segments. Afterwards a reference system has been defined from which each node has been defined in the Python code. The boundary conditions have been applied at the extreme nodes.
Boundary conditions	Hinge at the bottom and imposed displacement at the top node. Symmetry recreated preventing the transition in the z-direction.	At the bottom a hinge has been insert and on the top vertex a roller in order to avoid the transition in the negative x direction. To recreate the stiffness of the connection a rotational spring has been modelled in the connection between the two elements.
Type of analysis	Displacement controlled simulation.	Load controlled simulation.
External loading	Obtained from the reaction forces.	Imposed from the results obtained from the ABAQUS model.
Internal forces	Obtained from the reaction forces. In particular, the bending moment has been obtained multiplying the reaction force times the lever arm.	Calculated directly by the tool.
Stiffness of the connection	Recreated through the construction of the model, wherein the assembly was meticulously executed to accurately define the characteristics of all materials and components constituting the connection.	Recreated by means of the rotational spring and the applied spring constant.

4.2 Experimental tests

4.2.1 Description of the tests

The experimental results have been obtained by Ir. Mirko Pejatovic. The latter were related with different typologies of cross sections in which the reinforcement and thickness of glass were different.

The selected test set up used to conduct the experiment is depicted in Figure 4.2. The element was subjected to a displacement-controlled test with a force acting along the vertical direction.

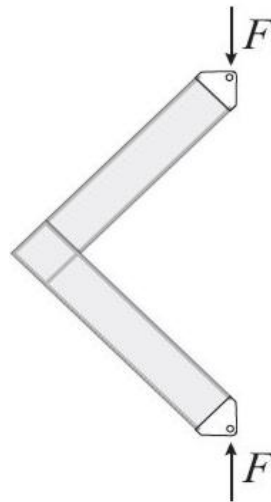


Figure 4.2: Schematization of the test set up.

The three different configurations that have been analysed are reported in Figure 4.3 and the geometrical characteristics are listed in Table 4.2. As can be observed, different reinforcement geometries have been analysed, this induced a difference in the size of the internal glass pane and so the area of glass.

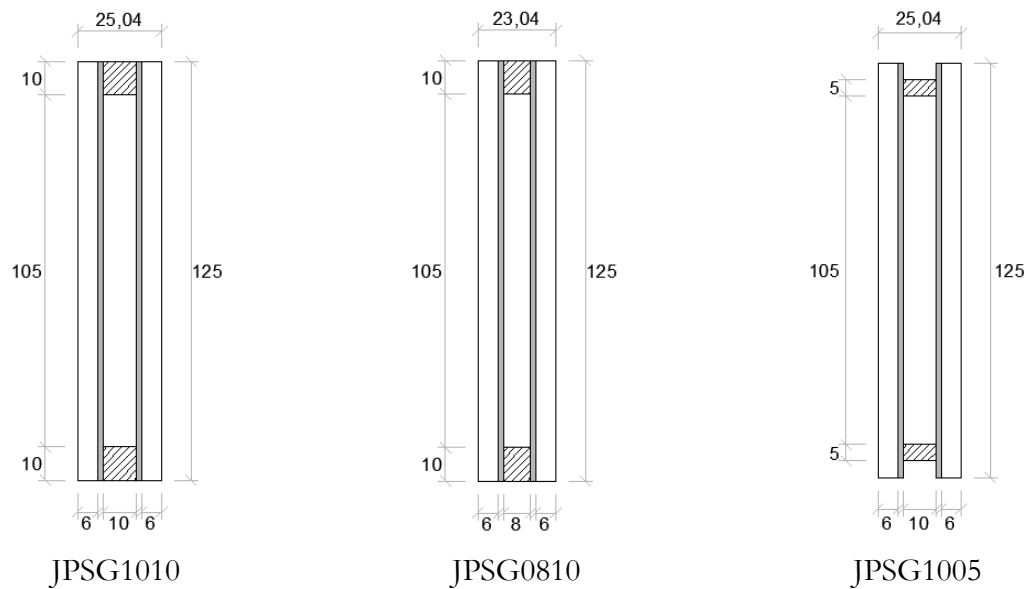


Figure 4.3: Different cross section typologies

Table 4.2: Geometrical characteristics of the different cross sections

	Symbol	Unit of measure	JPSG101	JPSG0810	JPSG1005
Height of ext. glass	$h_{g,e}$	[mm]	125	125	125
Thickness of ext. glass	$t_{g,e}$	[mm]	6	6	6
Height of int. glass	$h_{g,i}$	[mm]	105	105	105
Thickness of int. glass	$t_{g,i}$	[mm]	10	8	10
Thickness of interlayer	t_{SG}	[mm]	1.52	1.52	1.52
Height of reinforcement	h_s	[mm]	10	10	5
Thickness reinforcement	t_s	[mm]	10	8	10
Total height	h	[mm]	125	125	125
Total width	b	[mm]	25.04	23.04	25.04
Total area of glass	A_g	[mm ²]	2550	2340	2550
Area of 1 reinforcement	A_s	[mm ²]	100	80	50

4.2.2 Experimental results

The results of these tests are reported in Figure 4.4 in the form of Moment-Rotation graphs. In the x-axis are reported the relative rotations $\Delta\varphi$, in radians, and along the x-axis the bending moments M , in kNm.

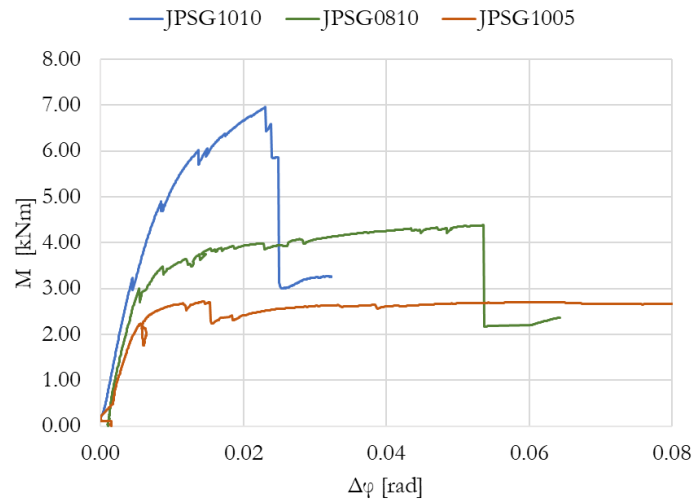


Figure 4.4: Moment-Rotation curves of the experiments

From the graph reported above can be understood that the different reinforcement influences the maximum bending moment reached by the different specimens. The three curves have an increasing trend characterised by small peaks that corresponds with the formations of the different cracks. The rotation at which the failure occurs varies for each case in an inversely proportional manner to the amount of reinforcement. The lower the amount of reinforcement, the greater the ductility exhibited by the connection.

In particular, the results of the tests are reported in Table 4.3, where M_c and $\Delta\varphi_c$ represent respectively the bending moment and relative rotation at the formation of the first crack, and M_f and $\Delta\varphi_f$ are the values of the same parameters at failure.

Using the data related with the formation of the first crack and the formula discussed in Chapter 3 -, it is possible to define a rotational stiffness, k , that can be used later in the Python code to approximate the real stiffness of the connection.

Table 4.3: Results of the experimental tests

Configuration	M_c [kNm]	$\Delta\varphi_c$ [rad]	M_f [kNm]	$\Delta\varphi_f$ [rad]	k [kNm/rad]
JPSG1010	3.19	0.0044	6.95	0.023	725.00
JPSG0810	2.98	0.0054	4.38	0.0536	551.85
JPSG1005	2.18	0.0052	2.70	0.0153	419.23

4.3 3D FEM analysis using reducing element approach

In the following section will be illustrated how the three different corner configurations have been modelled in ABAQUS Standard. In this case, the cross sections were recreated while maintaining all the layering. However, to minimize computational cost and increase the level of accuracy, only half of each cross-section has been modelled applying symmetry boundary condition at the interface. This also gave the possibility to create a more refined mesh that give the possibility to better recreate the cracking pattern in the glass components.

4.3.1 Material implementation

4.3.1.1 Annealed float glass

The Annealed float glass is characterized by a linear-elastic behaviour. The required properties for the material model in ABAQUS are the Young's modulus (E), Poisson's ratio (μ), and tensile strength (f_t). The values were previously defined in Table 2.1 and are respectively 70 000 MPa, 0.23, and 45 MPa.

In order to capture the brittle failure behaviour of glass, an adjustment is required in the material model. For this purpose, a user-defined material model, commonly referred to as a “UMAT model,” is necessary. The specific UMAT model for glass is based on the research conducted by Symoens E. (Symoens, 2019). This UMAT model enables the accurate representation of the brittle failure characteristics of glass.

4.3.1.2 Interlayer

The interlayer materials used in the experimental tests is SentryGlas® (SG). This is in particular a semi-crystalline thermoplastic polymer sheet.

In Abaqus has been implemented as a plastic material, the same as the stainless steel. Making reference to Table 2.2, the properties that were insert in the program are the Young's modulus (E), and Poisson's ratio (μ), with values of 110.53 MPa, and 0.49, respectively. Furthermore, the plastic behaviour was modelled defining a yield strength of 28.58 MPa and a final strength of 34.40 MPa. The material was considered infinitely plastic without a failure strain.

4.3.1.3 Stainless steel (AISI304)

The stainless steel used in the study has the quality of EN 1.4301 (AISI 304) and was subjected to tensile tests before testing. For each specimen different stainless steel were used. In particular, the characteristic yield stress and final stress and strain for each case are reported in Table 4.2Table 2.3.

The required properties for the material model of the steel in ABAQUS include Young's modulus (E), and Poisson's ratio (μ), 180000 MPa, and 0.29, respectively.

4.3.2 Definition of the geometry

The different cross sections that were implemented in ABAQUS Standard can be observed in Figure 4.5. The light blue represents the Annealed float glass, the dark blue the SentryGlas interlayer and the grey the stainless steel AISI304. Each element was implemented as a single part and then the final shape was created by assembling them.

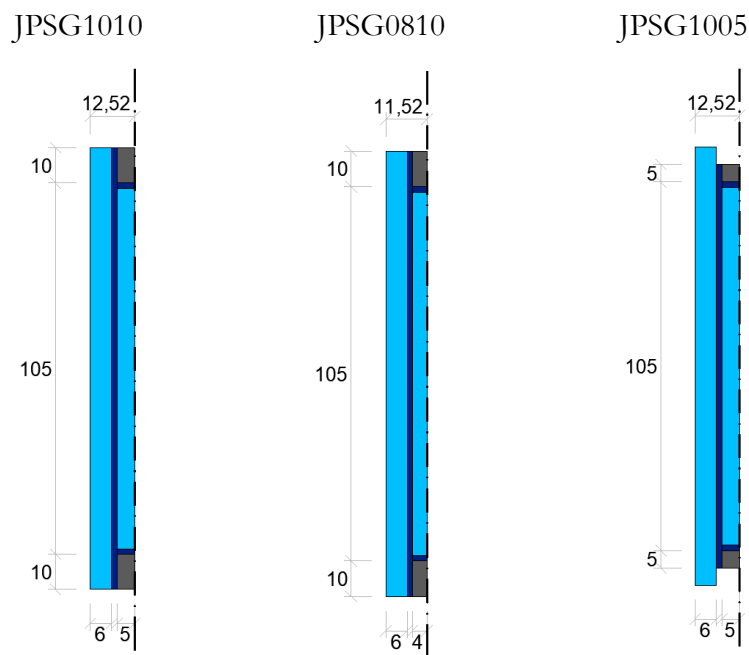


Figure 4.5: Half-cross sections implemented in ABAQUS Standard

In order to optimize the calculation time and the meshing, just a portion of the whole corner was modelled. The boundary conditions were applied at the original distance by means of datum points (RP-7 and RP-8), that were attached to the element by means of tie constrains.

Figure 4.6 shows the different boundary conditions that were applied to the model. At the bottom, all the 3 translations were fixed, and the rotations were left free, creating a hinge connection. A displacement was applied on top of the structure in the negative y-direction and was incrementally increased in a sequential manner. On the internal surface, in order to recreate the symmetry, the displacement in the z-direction was fixed.

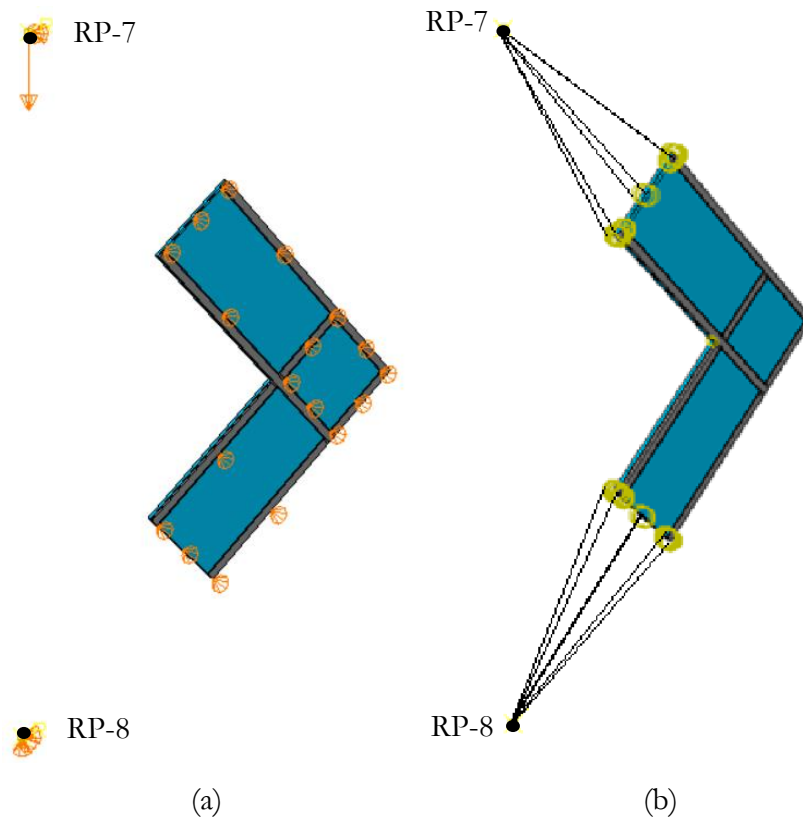


Figure 4.6: 3D FEM model in ABAQUS, applied boundary condition (a) and tie constraints (b)

To accurately approximate the cracking pattern of glass, a refined mesh consisting of tetrahedral elements was adopted. The mesh was further refined in the square part where the connection is established. This refinement allows for a more detailed representation of the structural behaviour and enables a better capture of the cracking phenomena occurring in the glass material.

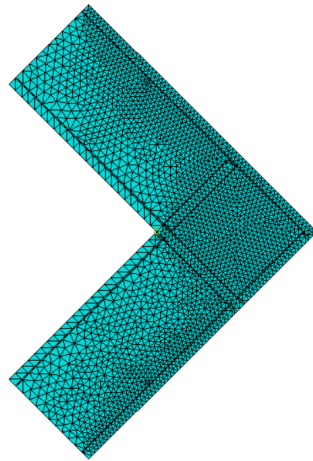


Figure 4.7: Mesh applied on the corner element

4.3.3 Results

The resulting curves are plotted in Figure 4.9, Figure 4.10 and Figure 4.11. Those curves have been obtained by considering the displacement of 3 points, the intersection (P11), one point in the upper beam (bL1) and one point in the bottom one (cL1). For each time step new coordinates of the points were obtained due to the deformations induced by the imposed displacement. Subsequently, by means of the three points two different straight lines have been defined. Analysing the change in the angular coefficient, the different angles with the horizontal were determined. Finally, calculating the difference between the original angle and the one in each different step, the relative rotation between the two elements was determined.

The x and y displacement of selected three points, highlighted in Figure 4.8 were extrapolated from the results of the program. From the original coordinates of the points was possible to recreate the movement of the straight lines connecting the bL1-P11 and cL1-P11.

In this case, the bending moments that are generated in each increment at the corner were defined by multiplying the vertical reaction force of the bottom support RP-8 with the lever harm between this point and point P11.

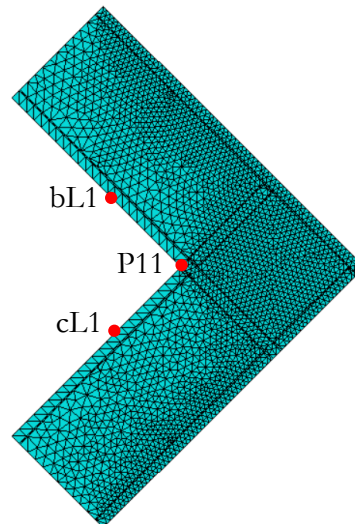


Figure 4.8: Position and nomenclature of the points used for the analysis

In this numerical simulation the curves present a trend that is closer to the one of the experiments due to the higher accuracy in both cross-section geometry and materials behaviour. The time increment Δt that was chosen for the numerical simulations is 0.005 seconds since this value resulted in a better approximation of the results.

In the first case, JPSG1010, the maximum bending capacity is not reached, this can be related with the yielding of the reinforcement and the bonding effect between the reinforcement and the interlayer. Furthermore, in this initial case, the transition in slope, coinciding with the occurrence of the first crack, appears to align with the second peak observed in the experimental curve (Figure 4.9).

The second numerical simulation is depicted in Figure 4.10. The linear phase, that is extended until the formation of the first crack, exhibits higher bending moments. Subsequently, the numerical cross-section begins to behave more similarly to the actual one. It does not reach the final failure points of the experiments. Besides this, the behaviours are comparable.

The curve obtained for the last case presents the same trend as the experiments (Figure 4.11). Nevertheless, it seems that the numerical cross section presents a higher bending capacity than the real one, since all the curve is shifted upward of almost 1 kNm. This effect could result from the loss of bond between the reinforcement and the interlayer that is not modelled in the numerical simulation.

Table 4.4: Comparison between experimental results and numerical simulation in ABAQUS

Configuration	Experimental results				Numerical results ABAQUS			
	M_c [kN]	$\Delta\varphi_c$ [kN]	M_f [kNm]	$\Delta\varphi_f$ [rad]	M_c [kNm]	$\Delta\varphi_c$ [rad]	M_f [kNm]	$\Delta\varphi_f$ [rad]
JPSG1010	3.19	0.0044	6.95	0.0230	4.65	0.0082	6.45	0.0209
JPSG0810	2.98	0.0054	4.38	0.0536	3.61	0.0047	3.85	0.0499
JPSG1005	2.18	0.0052	2.70	0.0153	3.34	0.0052	3.72	0.0141

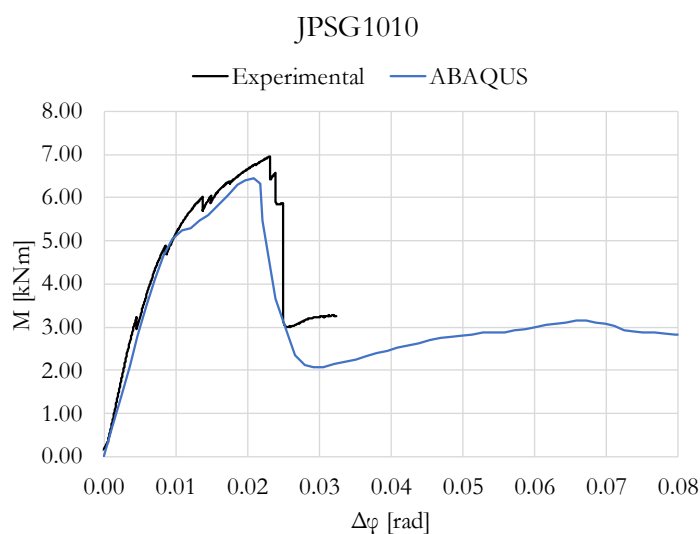


Figure 4.9: Resulting curves from experiments and DSM Tool for JPSG1010

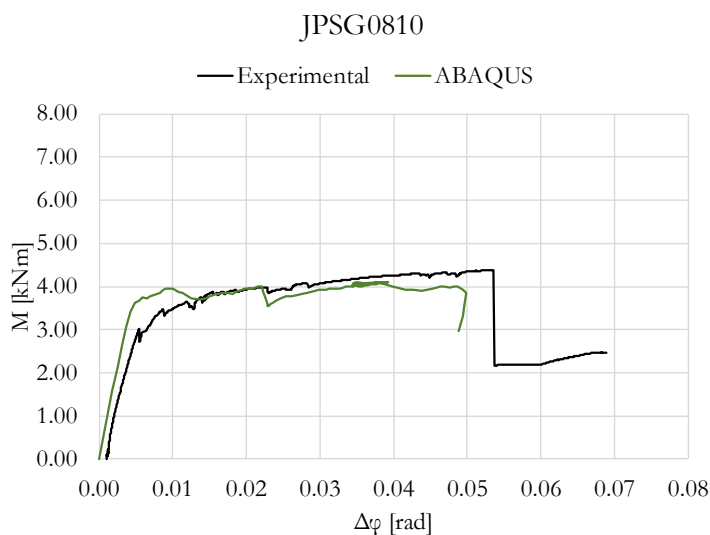


Figure 4.10: Resulting curves from experiments and DSM Tool for JPSG0810

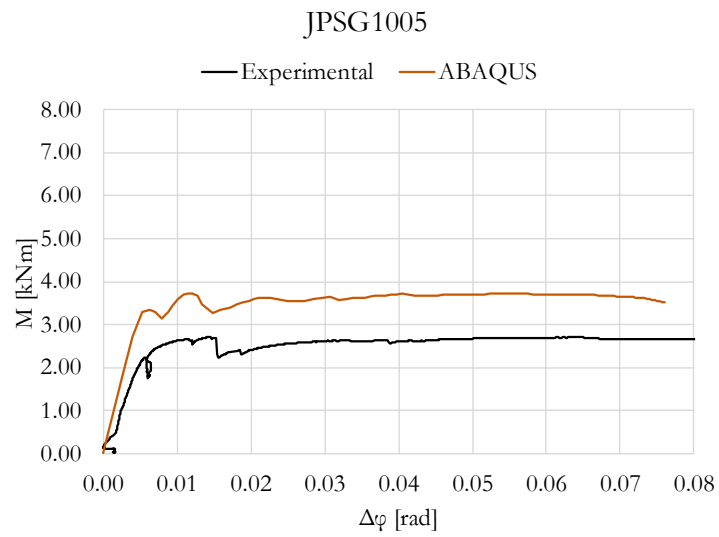


Figure 4.11: Resulting curves from experiments and DSM Tool for JPSG1005

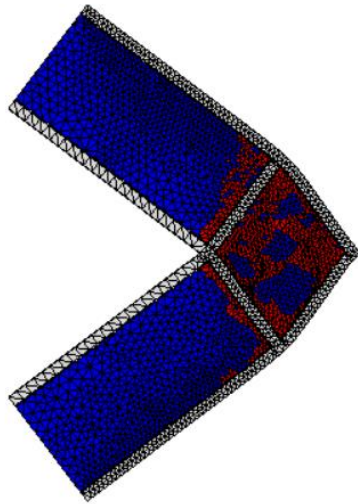


Figure 4.12: Resulting cracking pattern for JPSG1010

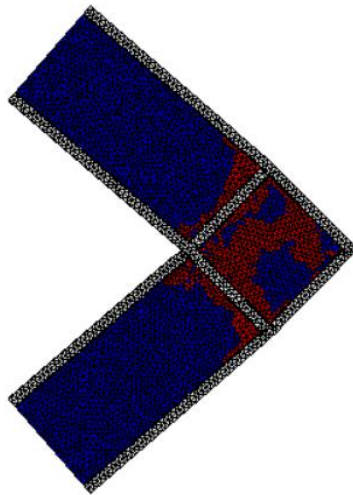


Figure 4.13: Resulting cracking pattern for JPSG0810

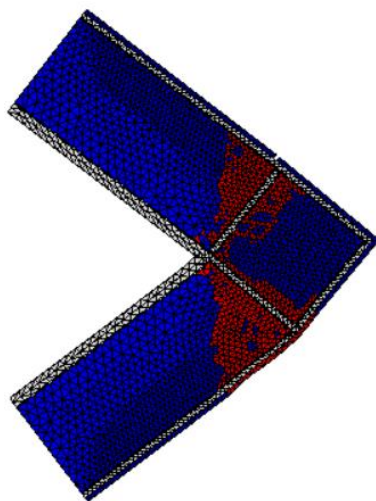


Figure 4.14: Resulting cracking pattern for JPSG1005

4.4 Direct Stiffness Method tool

The following chapter will explain the procedure by which the curves from the experiments have been reconstructed by means of a Python code based on the Direct Stiffness method.

This method is a linear, first-order model capable of calculating the displacements and internal forces of a structure. In the code that was used, second order effects and material non-linearity are added to the model, which also allows for the implementation of several corrosion effects. With these additions, a DSM tool is established in which the stiffness matrix is updated in a stepwise manner and iteratively solved, suited for the assessment of existing reinforced concrete structures.

In the case under analysis this tool will be used to model the composite cross section made of glass and stainless steel. Here the corrosion effects will be not taken into account, setting the time equal to zero. Furthermore, the concrete will be model as a linear-elastic material, giving the mechanical characteristics of annealed float glass.

To be able to accurately predict the structural performance of existing concrete structures, this Direct Stiffness Method is extended to a second order, non-linear tool allowing for the incorporation of degradation effects. The DSM tool start with the input of several parameters, including the geometry, external loads, environmental conditions etc. Next, an initiation is required due to the iterative nature of the process.

The second order effects are included in the Direct Stiffness Method by means of particular expressions in which the internal nodal forces are unknown [Van Coile, 2016]. From this, an iterative procedure is done starting from the input values and giving as an output the displacements and internal forces.

However, the Direct Stiffness Method considering second order effects is a linear model, which means that it assumes linear elastic materials. In order to get a more accurate analytical model, material non-linearity is added to the DSM. This is accomplished by updating the stiffness of each element based on the constructed moment-curvature diagrams and normal force-strain diagrams. The moment-curvature diagrams can be constructed for each element based on general flexural theory [Wright & MaxGregor, 2012]. Due to a certain curvature χ , tensile and compressive strains arise, separated by the neutral axis at a distance x from the outermost fibre in compression. The stresses corresponding to these strains can be determined by using stress-strain relationships. What is crucial is to recreate the elastic-brittle behaviour of glass and to define the correct geometrical characteristics of the cross sections, such as the area of glass and of reinforcement, position of the reinforcement and moment of inertia of the composite cross section.

4.4.1 Definition of the geometry

In order to define the geometry, the code uses an excel file in which a discretization of the model must be done. The model can be divided smaller beam elements that then will be connected one to the other. This is done by the definition of different nodes giving their x- and y-coordinate according to a user defined origin of the axis.

The subdivision that has been chosen is reported in Figure 4.15. The origin of the axis is positioned in the lower left corner so that all the x and y coordinates would result positive. Each beam has been divided in 10 parts (blue numbers) with a total of 21 points (green numbers).

The applied boundary conditions consisted of a hinge at the bottom node (node 1) and a roller at the top node (node 21). Furthermore, to replicate the correct behaviour of the connection, a spring has been inserted at the intersection, corresponding to node 11.

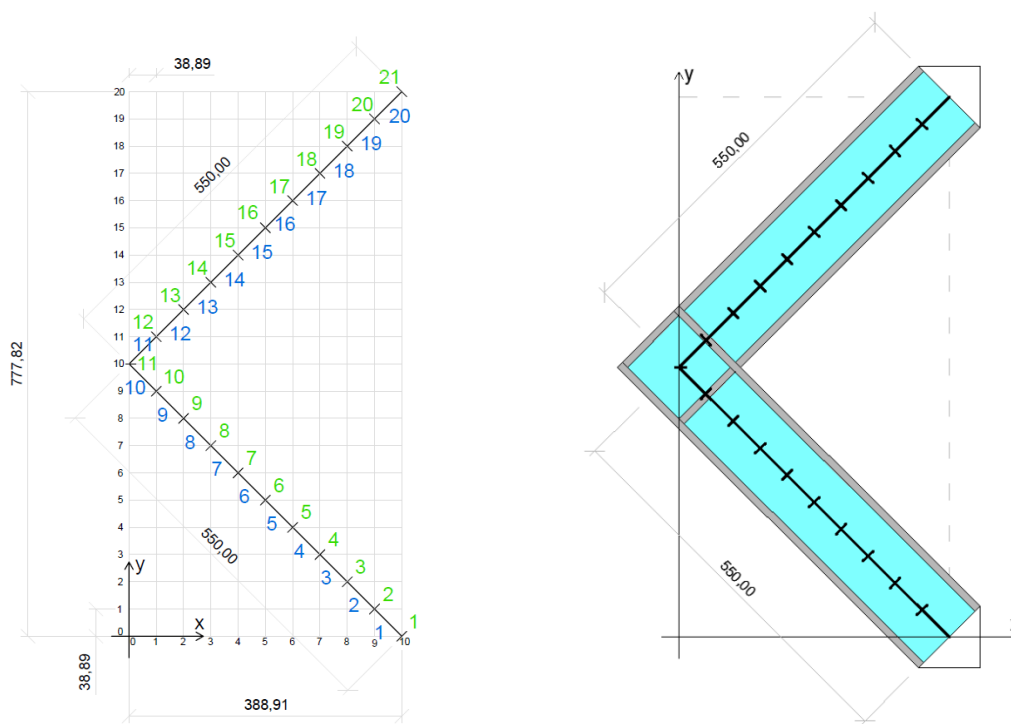


Figure 4.15: Subdivision of the corner element

4.4.2 Cross-section characteristics

The complex section formed by all the various materials, glass, reinforcement and interlayer, cannot be modelled in the programme, so a simplified section was introduced. First the characteristics of the materials used are introduced, and then how the geometric characteristics were introduced into the programme.

4.4.2.1 Materials behaviour

The constitutive diagrams used to describe the materials behaviour are reported here below (Figure 4.16). Has to be pointed out that the annealed float glass does not change for the different cases, however the characteristics of the stainless steel used for the reinforcement are not the same.

In this case a first approximation is done, since in the code is not possible to model a bi-linear stress-strain diagram for the reinforcement. From previous chapters is defined that the yield and final stress of steel are not the same. However, in the model the constitutive law of the steel is modelled as the continuous lines and not as the dashed once (Figure 4.16 (b), (c) and (d)).

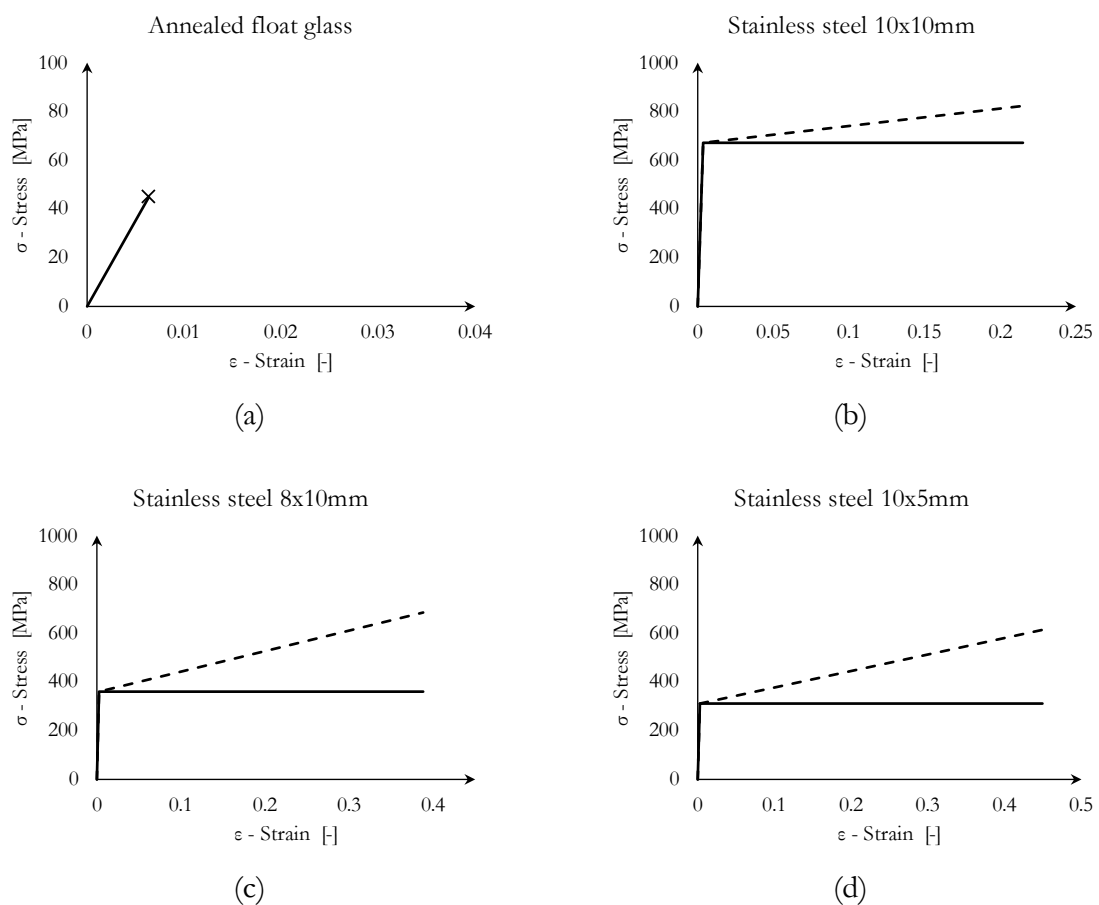


Figure 4.16: Graphs of the constitutive law of the materials

4.4.2.2 Geometrical characteristics

As mentioned earlier, due to the limitations of the Python code, it was necessary to employ a simplified cross-section instead of the original one. The primary goal was to preserve a hybrid moment of inertia that closely resembled that of the original section. To achieve this, the reinforcement was represented by a single reinforcement bar with an equivalent area. Regarding the glass component, maintaining the same moment of inertia required careful consideration of the height, which was kept consistent at 125 mm. The width, on the other hand, was calculated by neglecting the interlayer and considering only the thickness of the three glass panes. The comparison between the real cross sections and the numerical once can be observed in Figure 4.17, Figure 4.18 and Figure 4.19. The resulting geometrical characteristics are reported in . Additionally, the figures also include moment-curvature diagrams that are automatically generated by the program, which serves as the basis for its calculations.

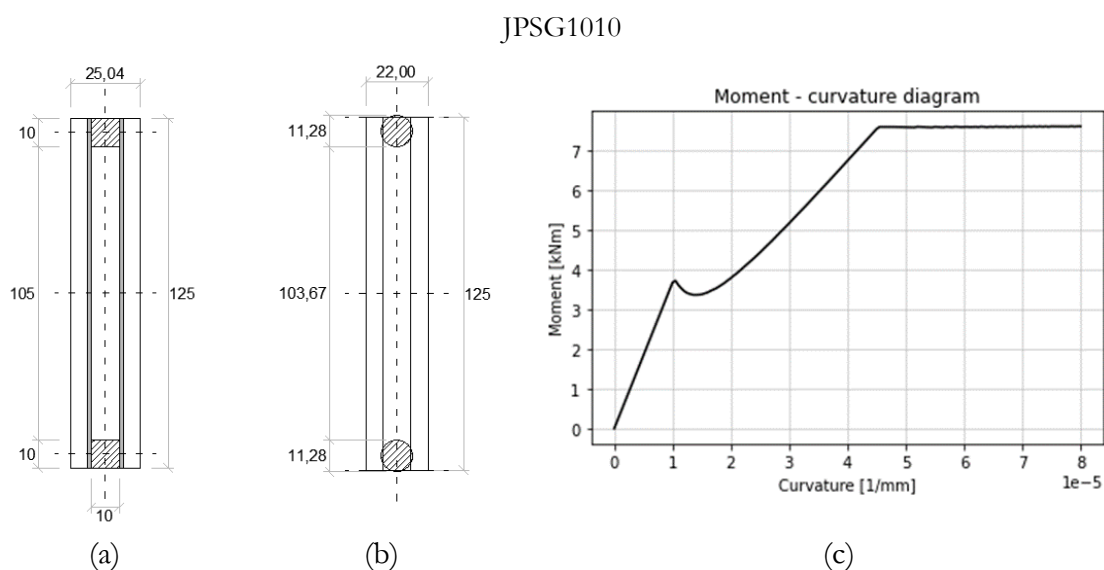


Figure 4.17: Real cross section (a), numerical cross section (b) and moment-curvature diagram defined by the DSM tool (c) for JPSG1010

JPSG0810

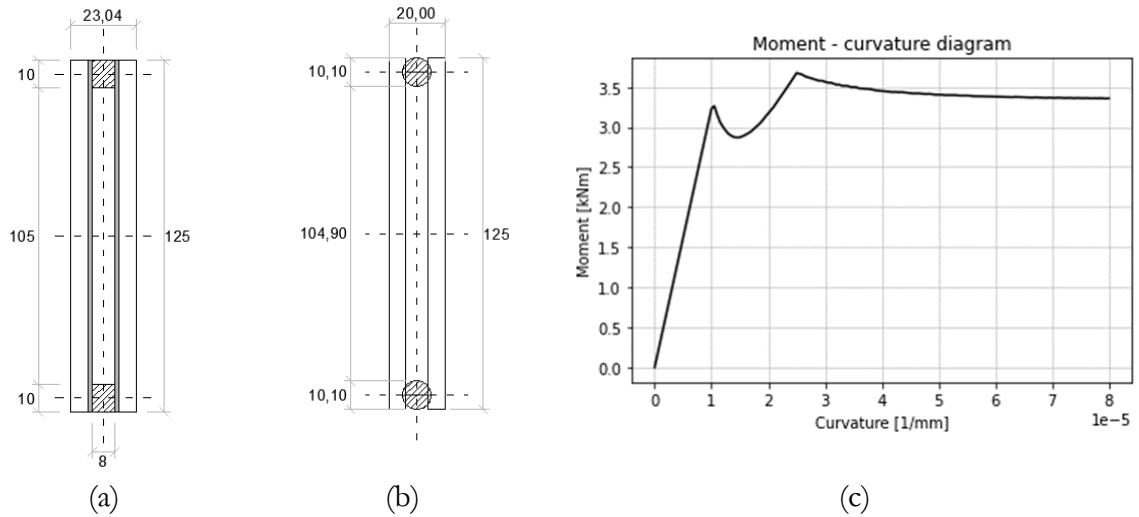


Figure 4.18: Real cross section (a), numerical cross section (b) and moment-curvature diagram defined by the DSM tool (c) for JPSG0810

JPSG1005

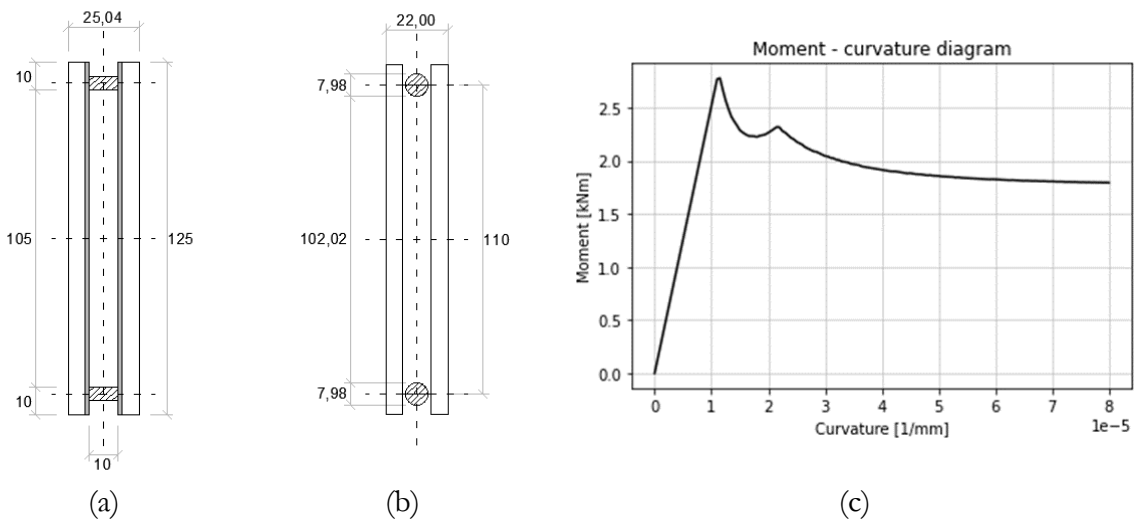


Figure 4.19: Real cross section (a), numerical cross section (b) and moment-curvature diagram defined by the DSM tool (c) for JPSG1005

Table 4.5: Characteristics of the real cross sections and of the once implemented in Phytion

	Symbol	Unit of measure	Real cross section			Equivalent cross section (Phytion)		
			JPSG1010	JPSG0810	JPSG1005	JPSG1010	JPSG0810	JPSG1005
Height of ext. glass	$h_{g,e}$	[mm]	125	125	125	125	125	125
Thickness of ext. glass	$t_{g,e}$	[mm]	6	6	6	6	6	6
Height of int. glass	$h_{g,i}$	[mm]	105	105	105	104	105	102
Thickness of int. glass	$t_{g,i}$	[mm]	10	8	10	10	8	10
Thickness of interlayer	t_{sg}	[mm]	1.52	1.52	1.52	-	-	-
Total height	h	[mm]	125	125	125	125	125	125
Total width	b	[mm]	25.04	23.04	25.04	22	20	22
Total area of glass	A_g	[mm ²]	2550	2340	2550	2750	2500	2750
Dimension of the reinforcement	$b_s \times h_s$	[mm]	10x10	08x10	10x05	-	-	-
Diameter of the reinforcement	d	[mm]	-	-	-	11.28	10.09	7.98
Area of 1 reinforcement	A_s	[mm ²]	100	80	50	100	80	50
Hybrid bending stiffness	EI_{hybrid}	[Nmm ²]	3.23×10^{11}	2.86×10^{11}	2.59×10^{11}	3.22×10^{11}	2.86×10^{11}	2.53×10^{11}
Hybrid moment of inertia (*)	I_{hybrid}	[m ⁴]	4.62×10^{-6}	4.09×10^{-6}	3.70×10^{-6}	4.59×10^{-6}	4.09×10^{-6}	3.62×10^{-6}

(*) The hybrid moment of inertia is obtained dividing the hybrid bending stiffness with the Young' s Modulus of glass ($E= 70000 \text{ MPa}$). The values are reported in m4 since is the unit of measure which is required in the Phytion code

4.4.3 Results

In the graphs in Figure 4.21, Figure 4.22 and Figure 4.23 the experimental curves, in black, and the curves obtained from the data coming from the DSM Tool, in colours, are plotted together.

The curves representing the results of the Python code have been obtained following the same procedure previously explained for the ABAQUS model. As before, the 3 nodes considered are, the intersection (point 11), one point in the upper beam (point 12) and one point in the bottom one (point 10). From the original coordinates of the points was possible to recreate the movement of the two beams. Considering the changes in the angular coefficient, the angles with the horizontal were determined and, at last, the relative rotations.

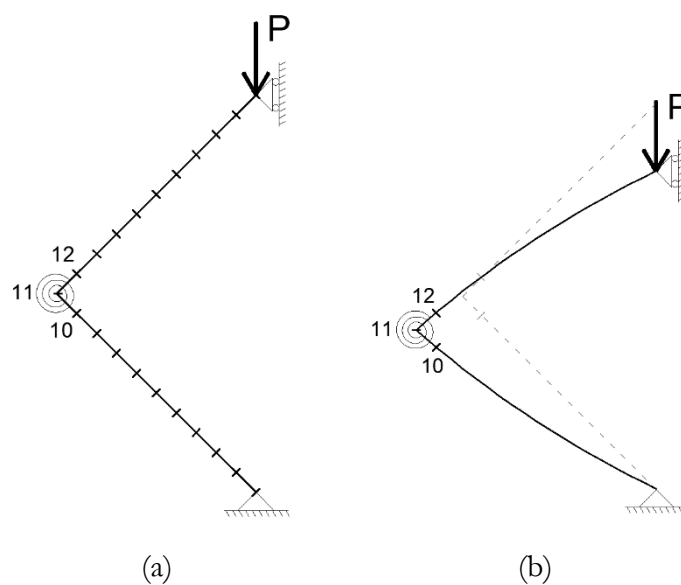


Figure 4.20: Position of the chosen points in the undeformed (a) and deformed (b) configuration

The bending moments at each load increment were directly calculated using the DSM tool. A distinct maximum load was assigned to each case, as each typology exhibits failure at a different load. However, the number of analysis steps between the beginning and end remained consistent to ensure an adequate number of data points for plotting the curve with the highest possible accuracy.

In Table 4.6 are reported the results of the three simulations. In particular, is it possible to compare for each simulation the value of the initial load P_0 , final load P , number of steps n , number of steps completed n_f , load at failure P_f , bending moment at failure M_f and the final relative rotation $\Delta\varphi_f$.

Table 4.6: Results of the DSM Tool

Configuration	P_0	P	n	n_f	P_f	M_f	$\Delta\varphi_f$
	[kN]	[kN]	-	-	[kN]	[kNm]	[rad]
JPSG1010	1	21	100	96	20.39	7.17	0.0092
JPSG0810	1	10	100	97	9.82	3.42	0.0052
JPSG1005	1	9	100	88	8.11	2.82	0.0055

In Figure 4.21, Figure 4.22 and Figure 4.23 are reported the results from the simulations in the DSM tool.

As can be observed, together with the experimental curves in black, two sets of curves are plotted. The once named “Rigid” in the legenda are the curves resulting from the analysis without applying a spring constant in the corners, so considering a stiff connection. The other set of curves are the once considering the spring constant k in kN/rad defined in Table 4.3.

As a general observation, it can be noted that in all three cases, the outcomes derived from the numerical simulation considering the spring constant exhibit a consistent pattern with the experimental results during the elastic phase. However, a difference arises between the two curves once the initial crack appears. This disparity primarily stems from the fact that the experimental curves were obtained through a displacement-controlled test, whereas the DMS tool in Python operates with a fixed load increment and lacks the ability to control displacements.

Furthermore, the calculations in the code rely on the Moment-Curvature diagram of the cross-section, and the plastic branch associated with the yielding of the reinforcement cannot be utilized due to the continual increase in load. The Moment-Curvature diagrams, automatically defined by the code, were previously reported in in Figure 4.17 (c), Figure 4.18 (c) and Figure 4.19 (c).

For JPSG1010 the simulation exhibits a higher stiffness, even though the hybrid bending stiffness is comparable. The other two cases JPSG0810 and JPSG1005 approximate the elastic branch in a precise manner. Hower, all the three cases do not consider the influence of the yielding of the reinforcement.

Furthermore, it should be emphasized that the DSM tool takes into account the formation of a singular crack in correspondence of the section where the tensile strength of the glass is exceeded first. Subsequently, the fracture progressively widens with each subsequent increase in load. This perspective does not account for the actual behaviour of the glass, where there is the development of numerous small fractures, that subsequently grow and reach the compressed edge of the beam. A final numerical comparison of the results is reported in Table 4.7.

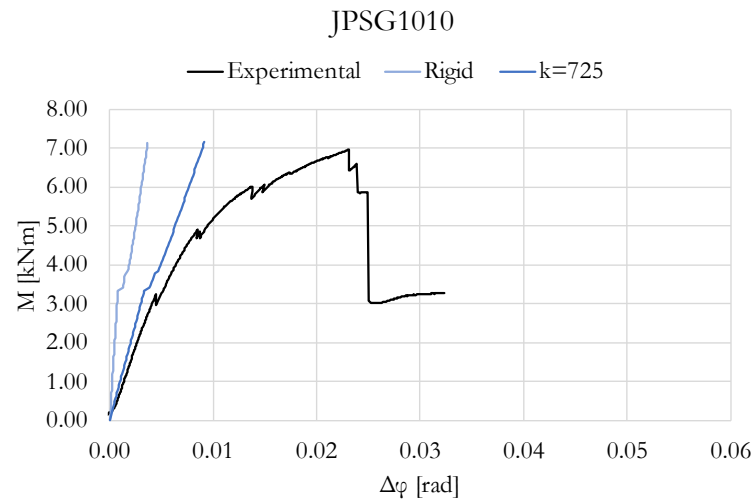


Figure 4.21: Resulting curves from experiments and DSM Tool for JPSG1010

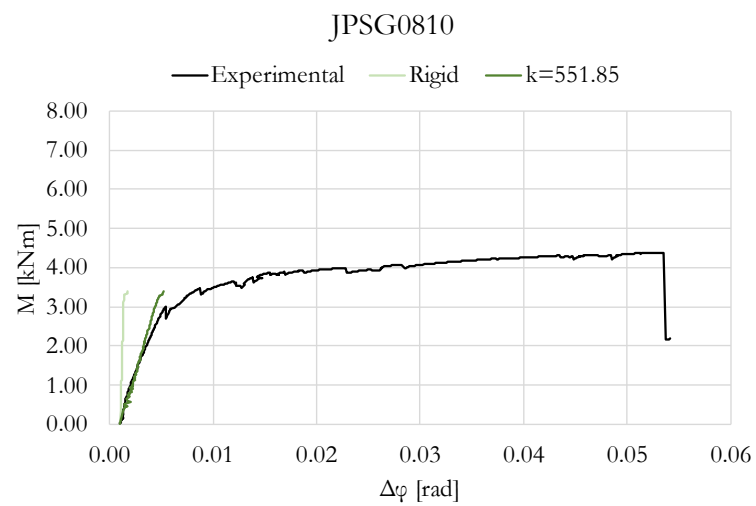


Figure 4.22: Resulting curves from experiments and DSM Tool for JPSG0810

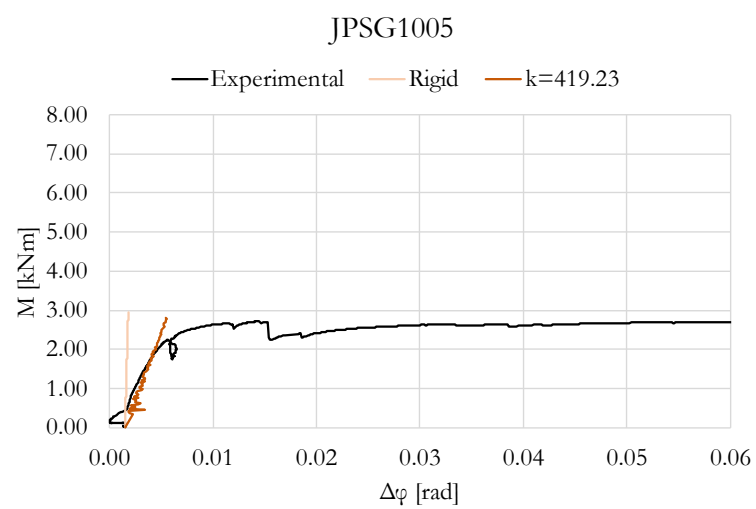


Figure 4.23: Resulting curves from experiments and DSM Tool for JPSG1005

Table 4.7: Comparison between experimental results and numerical simulation in Python (DSM Tool)

Configuration	Experimental results				Numerical results (DSM Tool)			
	M_c [kN]	$\Delta\varphi_c$ [kN]	M_f [kNm]	$\Delta\varphi_f$ [rad]	M_c [kNm]	$\Delta\varphi_c$ [rad]	M_f [kNm]	$\Delta\varphi_f$ [rad]
JPSG1010	3.19	0.0044	6.95	0.0230	3.26	0.0033	7.17	0.0092
JPSG0810	2.98	0.0054	4.38	0.0536	3.22	0.0047	3.42	0.0052
JPSG1005	2.18	0.0052	2.70	0.0153	-	-	2.82	0.0055

4.5 Comparison of the results

In this section a comparison between the two different methodologies used to recreate the experimental curves will be done. The results are plotted together for the three cases in Figure 4.24, Figure 4.25 and Figure 4.26.

For the first case under analysis, the curve generated by the Python code (DMS Tool) consistently remains above the resulting curves of the experiment and of ABAQUS. After the elastic branch, following the formation of the first crack, both curves exhibit a similar increasing trend, but with a significant separation between them. The curves describing the DSM tool results exhibits higher stiffness that result in a much lower differential rotation at failure in comparison with both, experiments and ABAQUS. As previously mentioned in the section discussing this modelling approach, this discrepancy in behaviour can be attributed to the fact that the Python code does not operate as a displacement-controlled test, resulting in this distinct curve behaviour.

Regarding the numerical curves obtained from the results in ABAQUS Standard, it can be observed that they consistently describe the data. However, in this case, the curve remains consistently below the experimental curve, indicating that the cross-section exhibits lower stiffness. The intersection of the two curves occurs at the second peak of the experimental curve, coinciding with the change in slope of the numerical curve and indicating the end of the elastic branch.

In conclusion, it can be stated that the behaviour of the experimental curves during the elastic branch is accurately replicated. However, when nonlinearities in the different materials come into play, the curve resulting from the DSM tool does not accurately approximate the results.

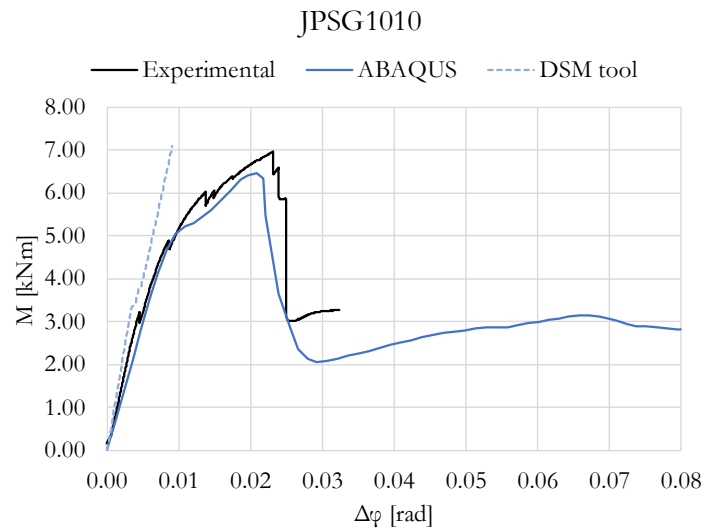


Figure 4.24: Resulting curves for JPSG1010

The set of curves corresponding to the JPSG0810 configuration is depicted in Figure 4.25. In this case the stiffness of the cross section is described in a perfect way in the DSM tool during the elastic phase. However, due to the nature of the Python code, the plastic branch of the cross-section cannot be effectively utilized since the load consistently increases.

The curve resulting from the ABAQUS data displays a trend that aligns with the experimental curve. Nonetheless, the cross-section exhibits higher stiffness until the formation of the first crack, after which the behaviour is reasonably replicated until failure, which occurs prematurely compared to the actual behaviour.

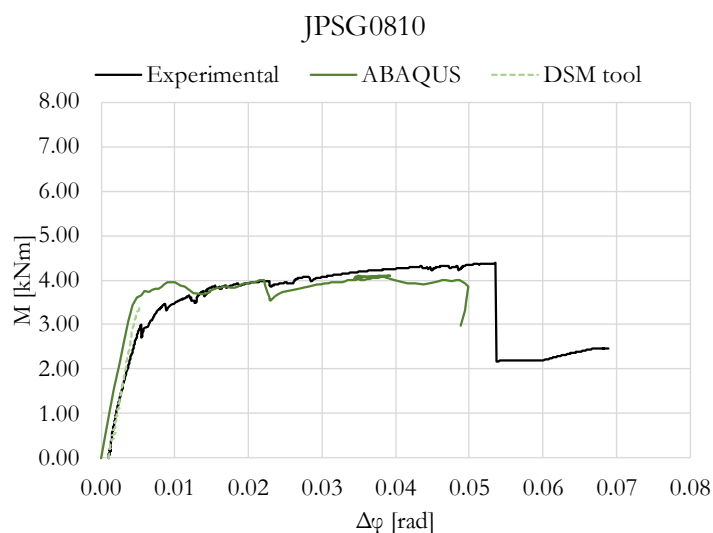


Figure 4.25: Resulting curves for JPSG0810

Lastly, the curves pertaining to the JPSG1005 configuration are illustrated in Figure 4.26. Due to the Moment-Curvature relationship of the cross-section and the continuous increase in load within the DSM tool, the failure in the Python results corresponds to the conclusion of the elastic branch that also in this case is recreated in a consistent way. Consequently, the curve no longer represents the behaviour of the cross-section beyond that point.

On the other hand, the ABAQUS curve exhibits a trend that effectively reproduces the behaviour of the cross-section. However, the cross-section appears to be stiffer, and the entire dataset is shifted by approximately 1 kNm. This discrepancy may be attributed to the occurrence of slip in the reinforcement during the test, which is not captured by the simulations due to the reduced bonding surface.

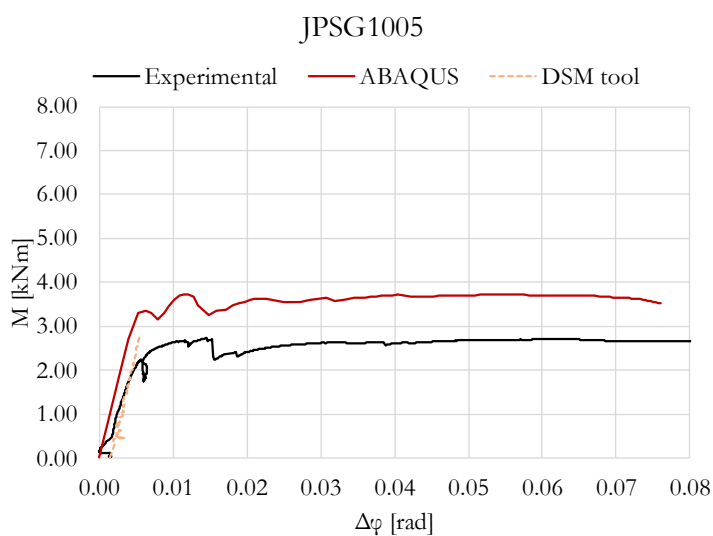


Figure 4.26: Resulting curves for JPSG1005

Chapter 5 - Frame analysis

The following section will analyse the behaviour of the abovementioned cross sections employed to form a frame, with the aim to understand their behaviour in a complete system.

Below in Figure 5.1 is reported the schematization of the frame. It is formed by three columns and two beams; the height of the columns will be 1500 mm and the length of the beams will be 1500 mm. On the system will act two vertical load P , applied at midspan of the two beams, and a horizontal load H that will act on the top of the left column. The boundary conditions considered for the column base connection are hinges. Those have been chosen because, in practical applications, establishing a connection that ensures zero rotation is highly challenging.

The frame as is presented will be recreated both in the in ABQUS and in the DSM tool in order to compare the results of the two sets of simulations. Different loading conditions will be analysed to obtain a better understanding of the influence that the different loads have on the structure. In this instance, there are no accessible experimental outcomes, thereby precluding the possibility of conducting a comparison with actual behaviour.

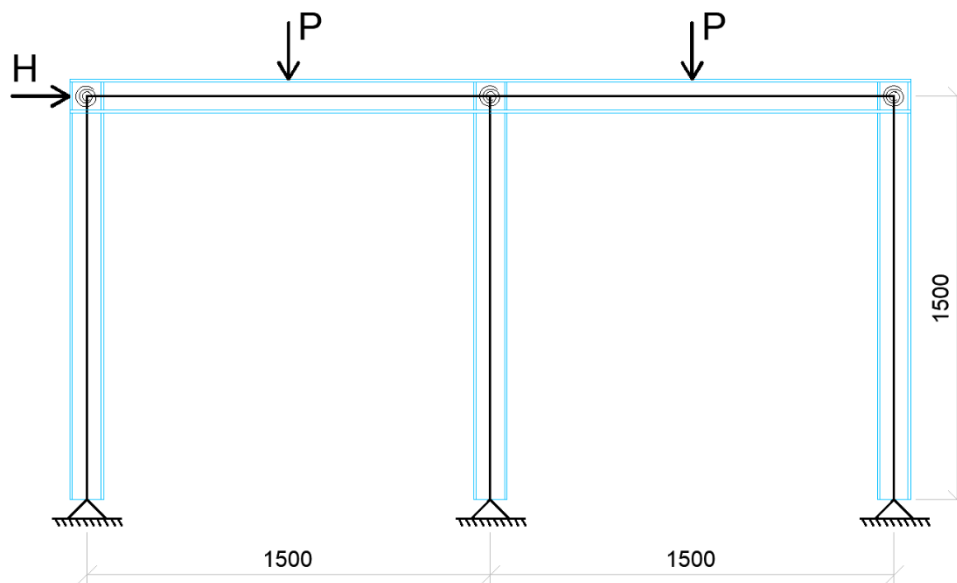


Figure 5.1: Schematic representation of the frame

5.1 3D FEM analysis using reducing element approach

Starting from the corner models, a full frame was developed in ABAQUS Standard in order to perform various simulations. All the geometric and mechanical characteristics previously defined in Chapter Material implementation 4.3.1 were also applied in the models that will be presented in this section. The main difference is related with the loading conditions, since in this case both vertical and horizontal loads are applied in a separate way.

In the study, different loading combinations will be presented: the simultaneous application of vertical and horizontal loads, the isolated impact of either vertical or horizontal loads on the structure, and finally, a sequential two-step loading sequence wherein gravity loads precede the application of horizontal forces.

5.1.1 Definition of the geometry

The cross sections developed for the frames are the one depicted in Figure 4.5 presented in chapter 4.3.1. Nevertheless, to accurately replicate the interaction between the components, each constituent part of the cross section, including glass, stainless steel, and the interlayer, was modelled as a singular element in ABAQUS. Subsequently, these elements were assembled to form the complete structure.

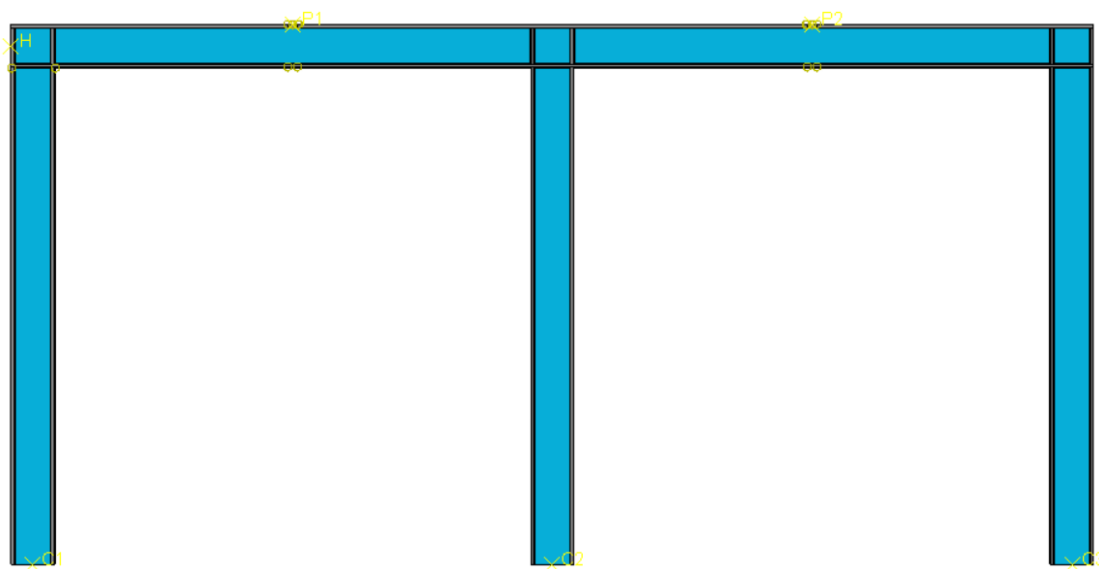


Figure 5.2: Frame modelled in ABAQUS Standard

The boundary conditions chosen for the frame are reported in Figure 5.3. At the base of each column, hinges were implemented as the designated boundary conditions. This choice is rooted in the challenge of achieving a clamped connection with zero rotations in real-world scenarios.

Given the modelling of a half cross-section, the prevention of translation in the z-direction was enforced across all frame elements. This measure was taken to establish symmetry and preclude out-of-plane deformations.

Furthermore, the loads were imposed as displacements. Both vertical loads, denoted as P , were subjected to uniform boundary conditions, resulting in consistent increments at each time step. Conversely, the horizontal load, H , was applied independently due to its action along the x direction. In the initial series of simulations, all three displacements were assigned an equivalent value of 100 mm.

To ensure precise application of boundary conditions, tie constraints were established at the base of the columns and at the points where forces were applied (yellow circles). For the loads, this strategy aimed to replicate the effects of concentrated forces while minimizing stress concentrations. Rather than being directly applied to discrete points, the forces were distributed across small partitions to confine their application within a restricted yet more widely dispersed region.

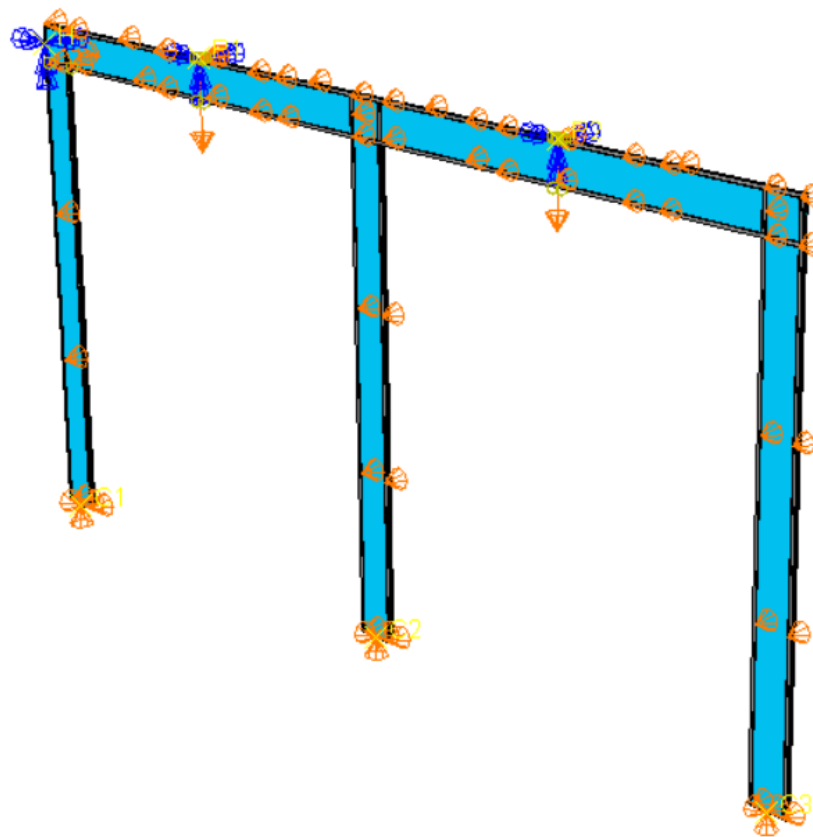


Figure 5.3: Applied boundary condition in the 3D FEM model

Frame analysis

In this case, the analysis has been focused on the load-bearing capacity of the frame and the behaviour of connections. Given that the crack formation has already been examined in the section concerning only the connection, by means of a very refined mesh, a distinct approach has been established. This has been done to accurately replicate the crack pattern while simultaneously optimizing the simulation duration.

A mesh refinement was defined in the connection elements with a size of 10 mm, while in the columns and in the beams the mesh size was 30 mm. Nevertheless, as will be evident in the subsequent chapters, the crack pattern is appropriately reproduced in the analysed cases.

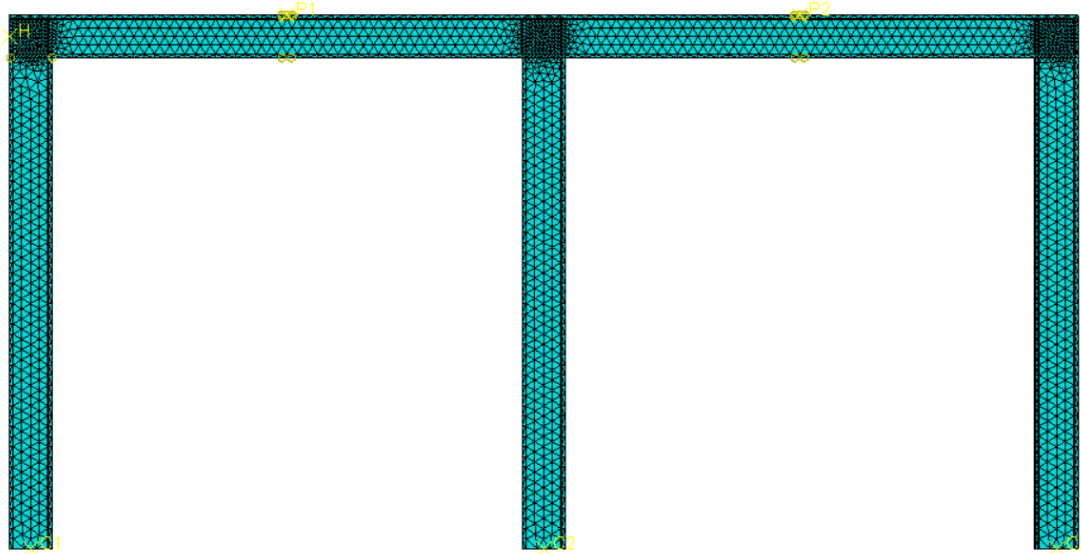


Figure 5.4: Mesh applied to the frame

5.1.2 Results

As previously indicated, the crucial consideration for the frame lies in its load-carrying capacity compared with its displacements and deflections.

In the next chapter, a parametric study will be conducted to examine the influence of the ratio between the vertical and the horizontal load on the behaviour of the frame. The results depicted in Figure 5.5 and Figure 5.6 stem from a vertical displacement of 100 mm applied to the positions P, as well as a horizontal shift, H, of 100mm. In this instance, the displacements were simultaneously applied.

To delineate the load-deflection and load-displacement curves pertinent to the vertical and horizontal behaviour of the frame, distinct points have been designated to capture data concerning their translations along the x and y directions.

For what concern the deflections, the chosen points correspond to the central locations on the lower portions of the two beams. As for translations, the selected points correspond to the central positions of the square corner elements as the top of the columns.

From the resulting graphs, can be grasped that all the three laminations present the same behaviour. However, the main parameters influencing the results are the vertical-to-horizontal load ratio and the quantity of reinforcement. In fact, the load carrying capacity of each case is decreasing with the area of reinforcement. A larger different can be observed between the first two curves, related with JPSG1010 and JPSG0810, and the one related with the JPSG005. This highlight that the change in the height of the reinforcement is a crucial parameter. Nevertheless, the last configuration presents a higher capacity to withstand horizontal loads, reaching higher horizontal displacement compared with JPSG1010 and JPSG0810.

Furthermore, in Figure 5.7, Figure 5.8 and Figure 5.9 the resulting crack patterns for the different cases are depicted. As can be observed, the crack formation is concentrated at midspan of the two beams, in the connections and in the top part of two external columns.

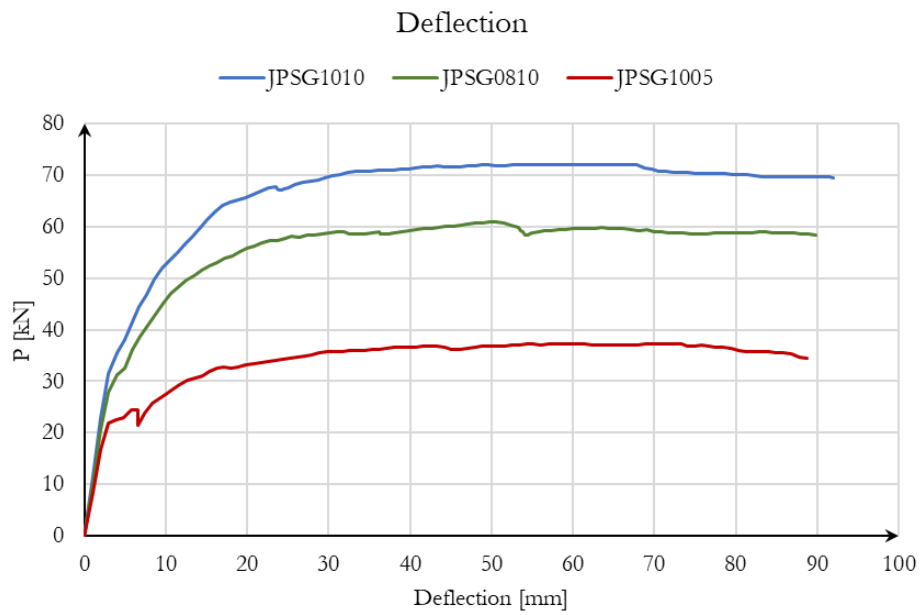


Figure 5.5: Load- deflection curves resulting from 3D FEM analysis in ABQUS

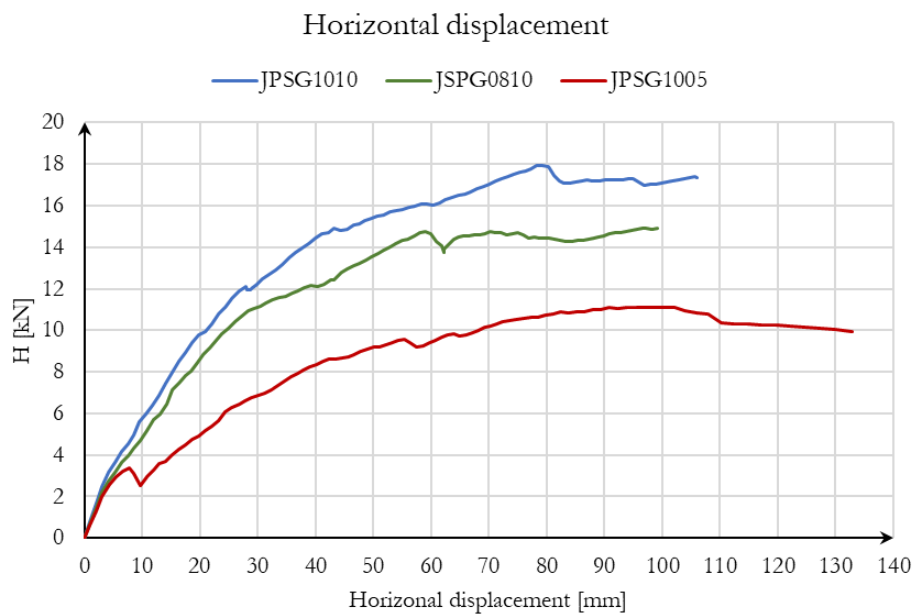


Figure 5.6: Load-displacement curves resulting from 3D FEM analysis in ABQUS

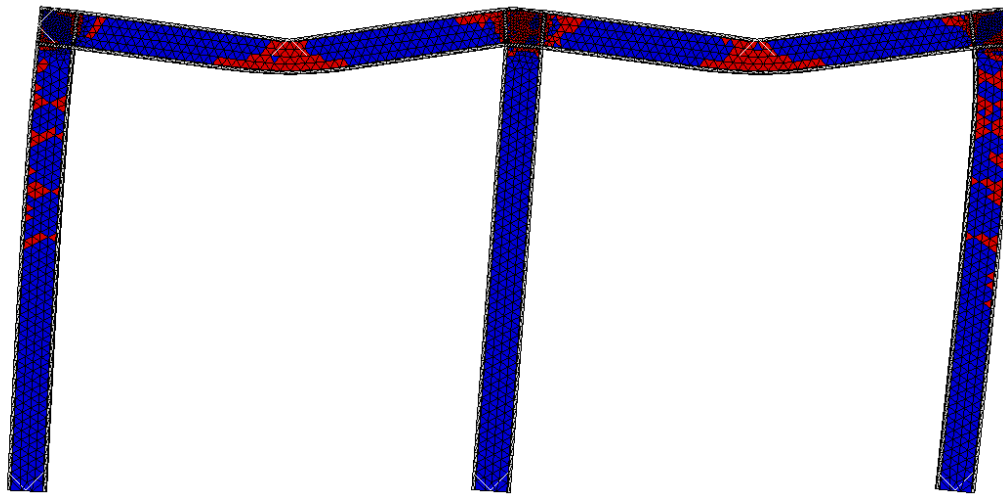


Figure 5.7: Crack pattern at failure for the frame modelled with JPSG1010

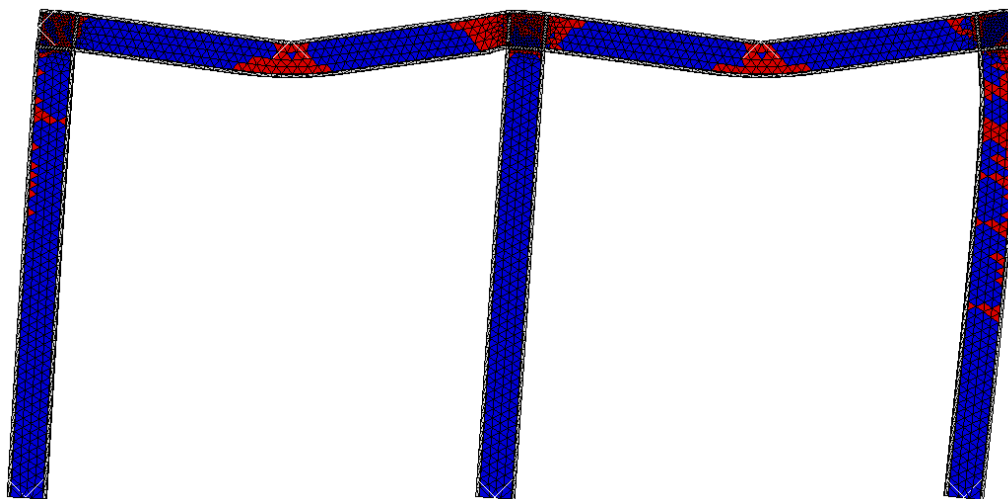


Figure 5.8: Crack pattern at failure for the frame modelled with JPSG0810

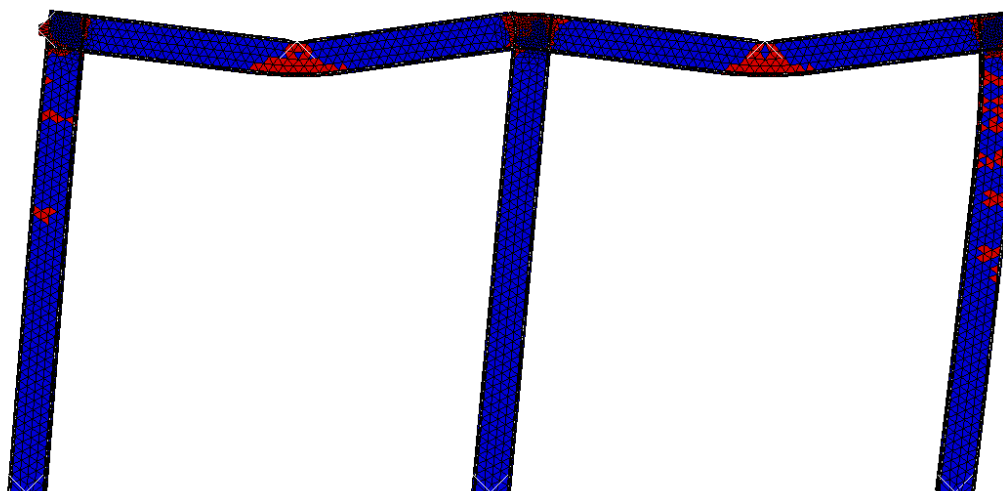


Figure 5.9: Crack pattern at failure for the frame modelled with JPSG1005

5.2 Direct Stiffness Method tool

In the DSM tool the frame has been modelled following the same steps previously mentioned for the corner model. Cross section characteristics, including both material behaviour and geometrical characteristics, have been kept unchanged.

As for the corner the frame was studied with and without the spring constant in the connections in order to grasp the influence that this has on the global behaviour.

5.2.1 Definition of the geometry

The elements of the frame present all the same length, 1500 mm. In the DSM tool the subdivisions that have to be defined must present all the same length. Nevertheless, the selection of this dimension must be executed to ensure a reliable approximation of outcomes, while simultaneously avoiding excessive fragmentation of components. This precaution is essential to prevent convergence issues within the results, which could lead to errors in the code execution.

Different lengths have been tested, however, the most suitable subdivision that provides an accurate approximation of the results is the one with 150 mm long elements, resulting in 10 subdivisions for each element. The outcome of this subdivision is presented in the Figure 5.10 and Figure 5.11 below.

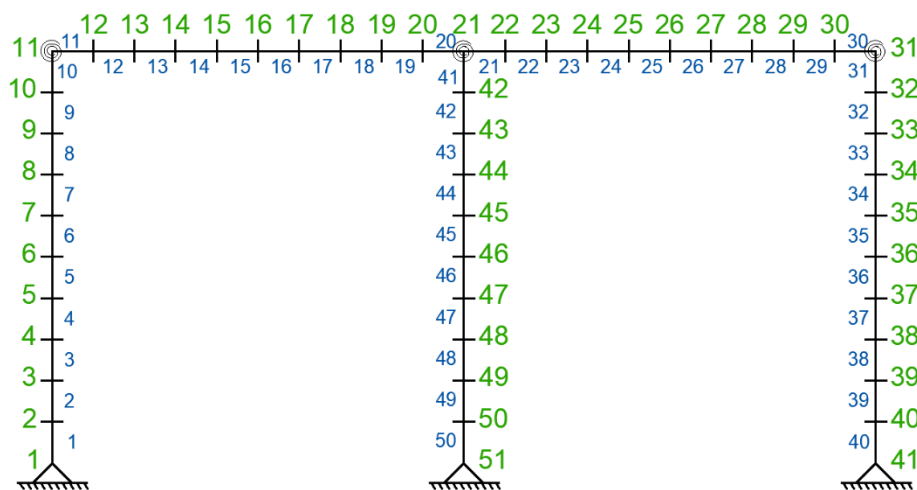


Figure 5.10: Subdivisions of the elements composing the frame

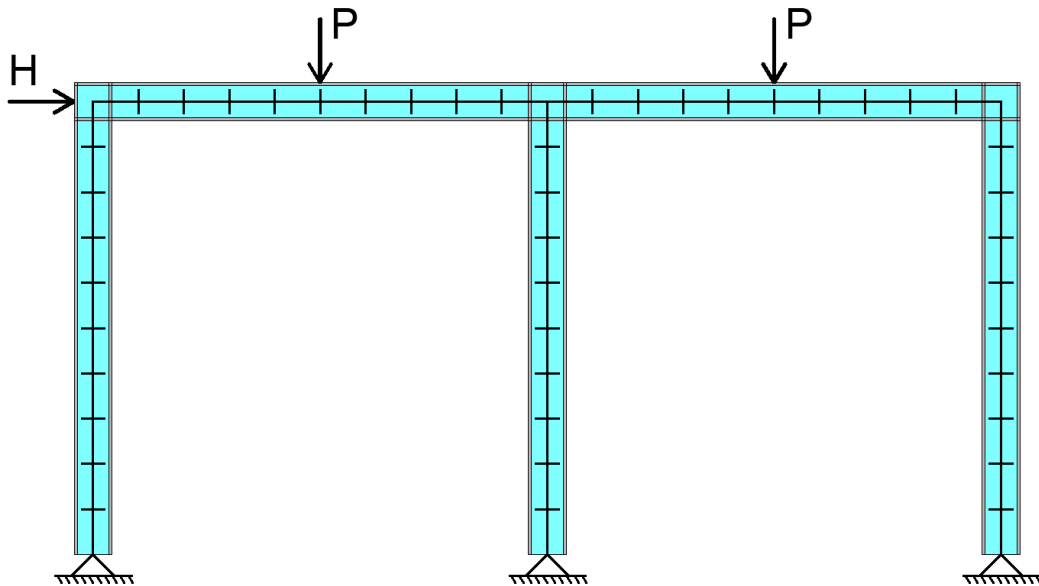


Figure 5.11: Subdivision of the elements inside the frame thickness.

5.2.2 Results

For the frame analysis the most crucial results are the once related with the load-displacement curves. In Figure 5.12, Figure 5.13 and Figure 5.14 are presented the graphs related with the deflections and the horizontal displacements.

The graphs relate with the vertical load P and the deflection have been obtained doing an average value of the deflection of mid span of the two beams. Similarly, the horizontal displacement was determined by averaging the top displacements of the three columns.

Although the maximum loads had been defined within the code, in all three cases, failure transpired before these loads were attained. Notably, the frames exhibited diminished resilience in contrast to the outcomes from ABAQUS analysis. This disparity can be attributed to the DSM tool's inability to account for stress redistribution within the frame. Instead, when the maximum bending capacity is exceeded at a single cross-section, the code deems the entire structure as having failed.

Furthermore, in all the three cases when the connection was modelled with the spring constant higher deformations and loads were reached, thanks to the higher ductility of the structure.

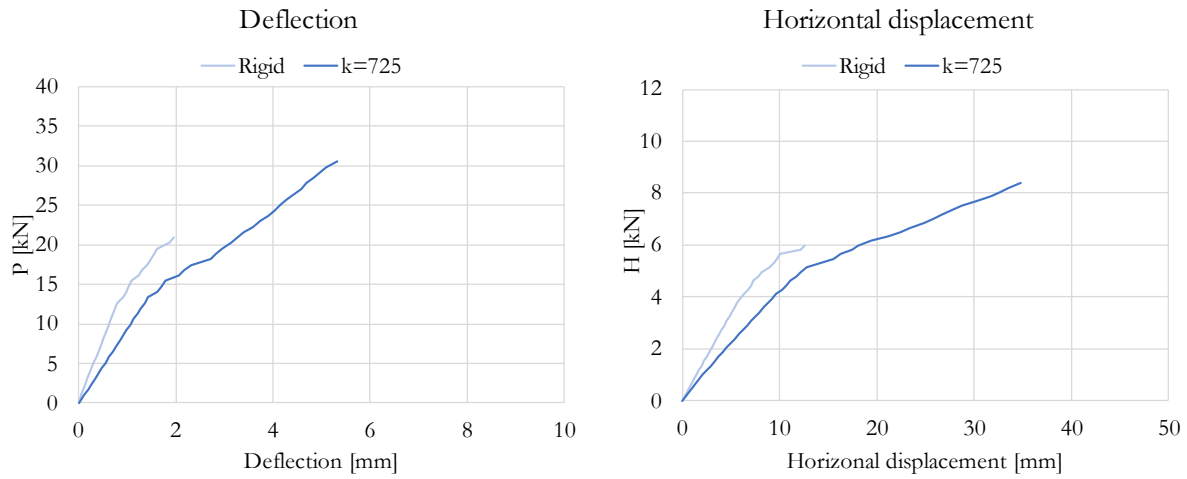


Figure 5.12: Results from the DSM tool for JPSG1010

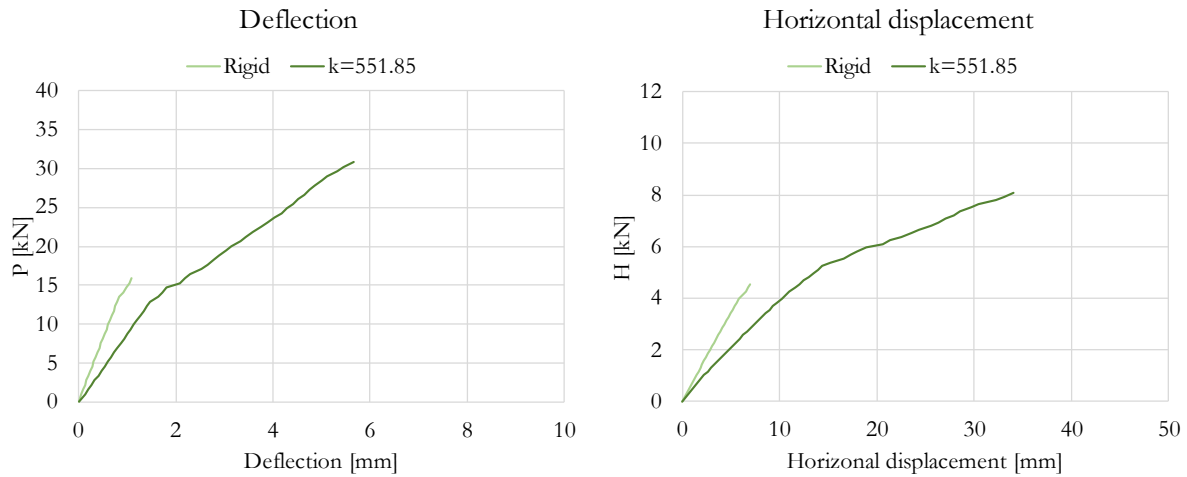


Figure 5.13: Results from the DSM tool for JPSG0810

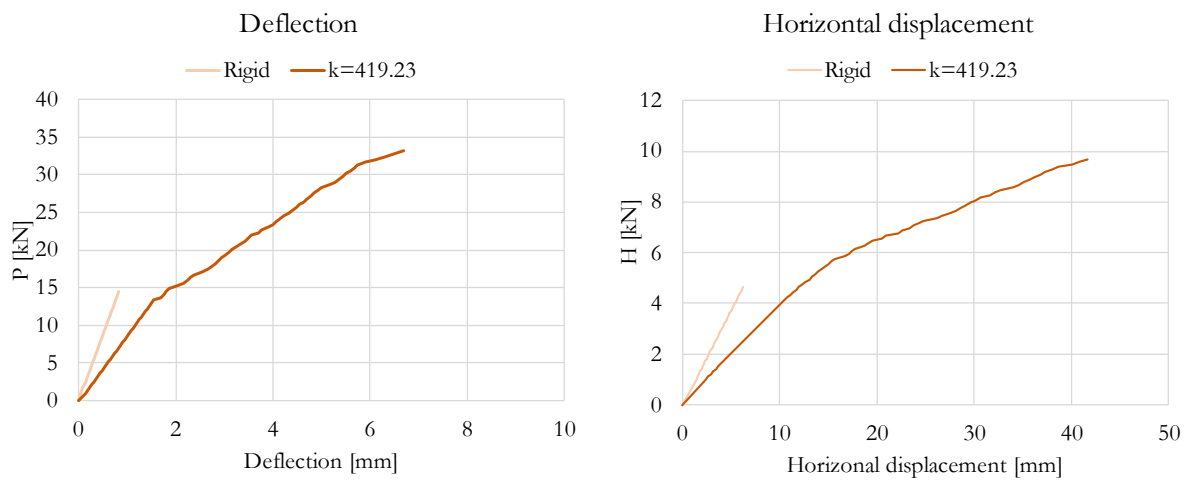


Figure 5.14: Results from the DSM tool for JPSG1005

5.3 Comparison of the results

In this chapter a comparison of the results coming from the frame analysis performed in ABAQUS Standard and DSM tool will be performed. The resulting curves are reported in the graphs presented in Figure 5.15, Figure 5.16 and Figure 5.17.

In general, what can be immediately understood is that the 3D FEM models recreate the behaviour of the frame in a more complete manner. This is in line with how the models are created due to the lower level of approximations and assumptions that are done.

In the case of the frame analysis, in contrast with the results presented for the corner in chapter 4.5, the results of ABAQUS are better approximated by the rigid connection in the DSM tool, up until the reaching the failure of the model to a lower load compared to the FEM model. When the spring constant considered the model presents a lower stiffness and there is a divergence in the results. However, as previously stated, when the connection is modelled with the spring constant higher loads can be reached.

These trends are consistent in all three cases studied. Reason behind this behaviour can be the way the DSM tool works, namely, the fact that it monotonically increases the load and cannot control the displacements. Furthermore, the DSM tool base his calculations on the moment-curvature relationships of the cross-sections (Figure 4.17 (c), Figure 4.18 (c) and Figure 4.19 (c)). Once the maximum moment is reached in one of the sections, the tool considers the failure of the entire structure, avoiding of stress redistribution which are recreated in ABAQUS.

Analysing the results of each single case, for the JPSG1010 the load at which the model in DSM tool reaches failure is around 40% of the maximum load registered in the ABAQUS model. While for the JPSG0810 is around 50%. For the last configuration JPSG105 the maximum load withstand by the structure is similar to the one resulting from ABAQUS and also the trend of the load-displacement diagrams is close. A possible explanation of this behaviour can be found in the fact that the stainless steel 5x10 mm exhibits higher ductility even if it can withstand lower stresses. This can be deduced from the stress-strain diagram reported in Figure 2.14 contained in the Chapter 2.3.3.

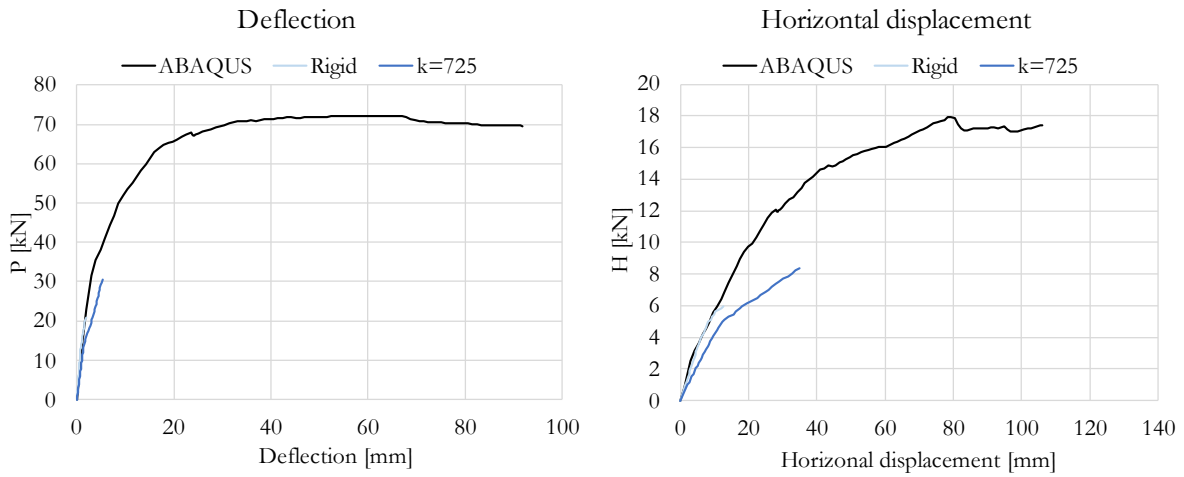


Figure 5.15: Resulting curves for the frames modelled with JPSG1010

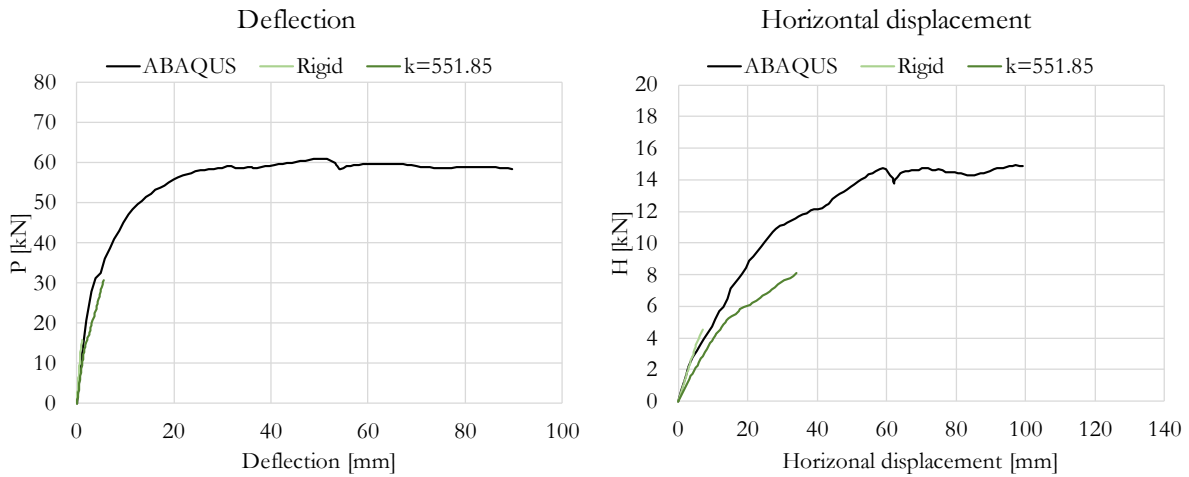


Figure 5.16: Resulting curves for the frames modelled with JPSG0810

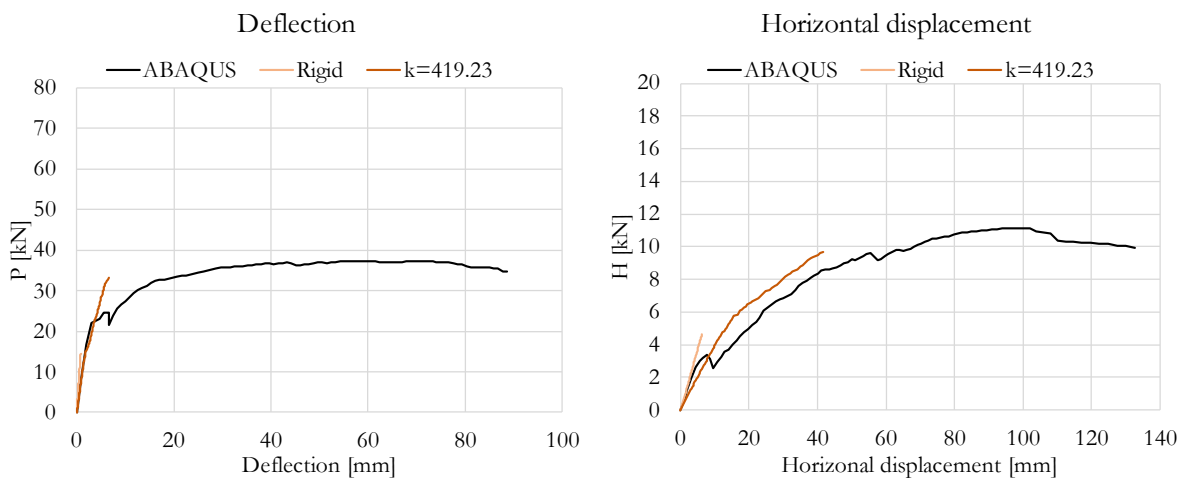


Figure 5.17: Resulting curves for the frames modelled with JPSG1005

5.4 Parametric study

As previously stated at the beginning of Chapter 5.1 different loading configuration have been analysed for the frame. Those results will be analysed in this chapter in which a comparison between the influence of the different loading conditions, horizontal and vertical, will be done.

5.4.1 Only vertical load P

This study, focusing on the application of just vertical loads on the structure, aim to understand the maximum capacity to withstand gravity load of the frame. The results of this parametric study are reported in Table 5.1.

Must be pointed out that the maximum load registered from the three models the ABAQUS does not differ much from the one obtained from the previous analysis. However, it can be observed that in the three cases the formation of first crack is clearly visible, corresponding to the peaks that can be observed on the left side of the graphs after which the liner-elastic branch is abandoned. From this point, an increasing branch is present up until the maximum load is reached, after which, a decreasing branch is present.

The resulting curves are presented in Figure 5.15, Figure 5.16 and Figure 5.17. In particular, two sets of curves are presented for each typology. The first one, denoted by (a) represent the whole deflection achieved by the ABAQUS model. The second one on the right, denoted by (b), are reported in order to display the different initial stiffness of the different models.

Afterwards, in Figure 5.21, Figure 5.22 and Figure 5.23 the bending moment, shear force and normal force diagrams are reported in order to show the internal forces in the frame at failure. In particular, those graphs were obtained from the DSM tool.

Lastly, in Figure 5.24, Figure 5.25 and Figure 5.26, the crack patterns corresponding to the different configurations are depicted. As can be observed, the three figures exhibit similarities and align with the distribution of bending moment and the deformation resulting from a loading configuration such as the one under examination

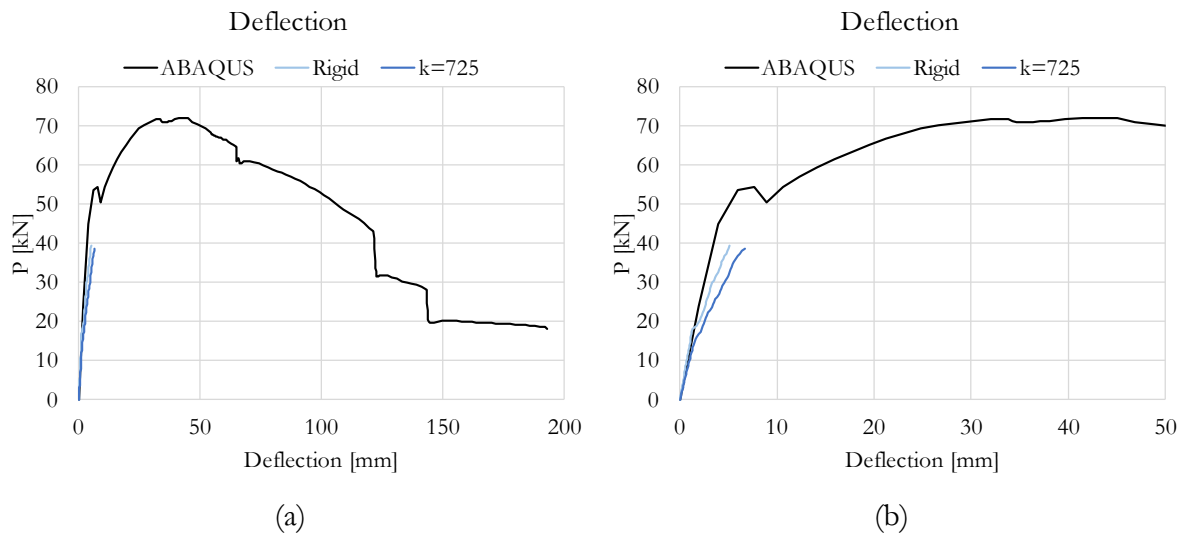


Figure 5.18: Resulting curves with the maximum deflection achieved (a) and with a focus on the initial stiffness (b) for the frame modelled with JPSG1010.

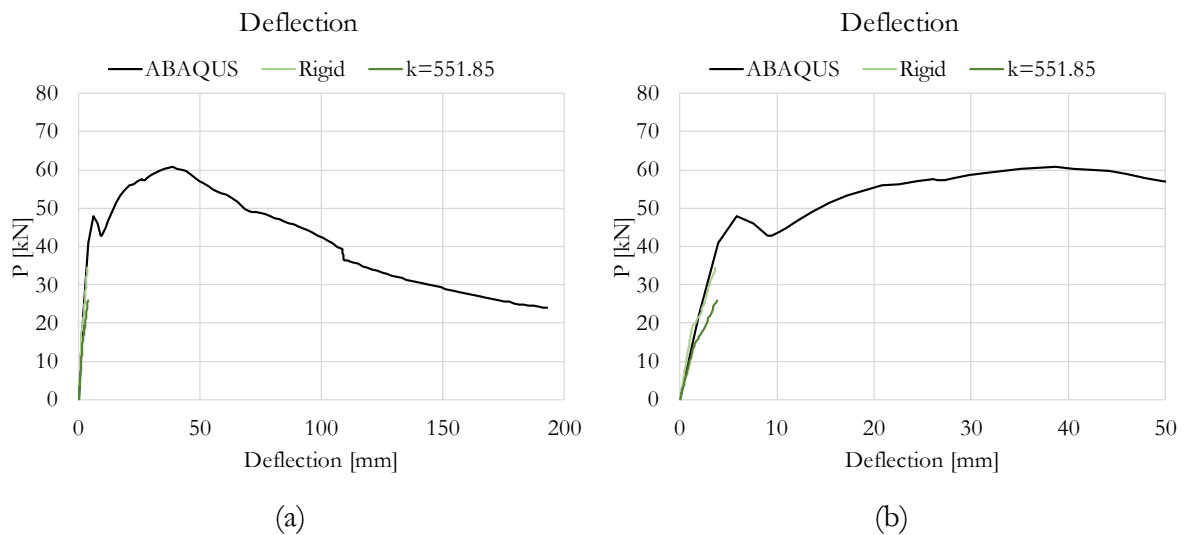


Figure 5.19: Resulting curves with the maximum deflection achieved (a) and with a focus on the initial stiffness (b) for the frame modelled with JPSG0810.

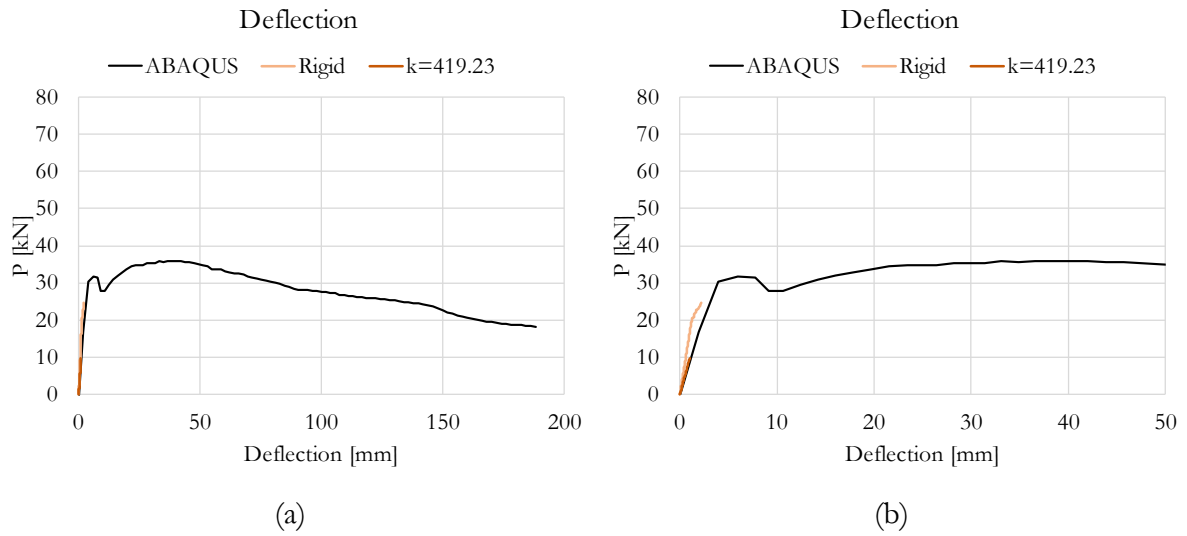


Figure 5.20: Resulting curves with the maximum deflection achieved (a) and with a focus on the initial stiffness (b) for the frame modelled with JPSG1005.

Table 5.1: Numerical results coming from the numerical modelling with just vertical load applied

Configuration	ABAQUS				DSM tool			
	Rigid		k		Rigid		k	
	P_c [kN]	d_c [mm]	P_f [kN]	d_f [mm]	P_f [kN]	d_f [mm]	P_f [kN]	d_f [mm]
JPSG1010	54.67	7.65	71.93	45.07	39.47	5.11	38.78	6.68
JPSG0810	47.89	5.91	60.76	38.75	34.37	3.68	26.03	3.84
JPSG1005	30.38	3.98	35.99	40.23	24.55	2.16	9.60	1.00

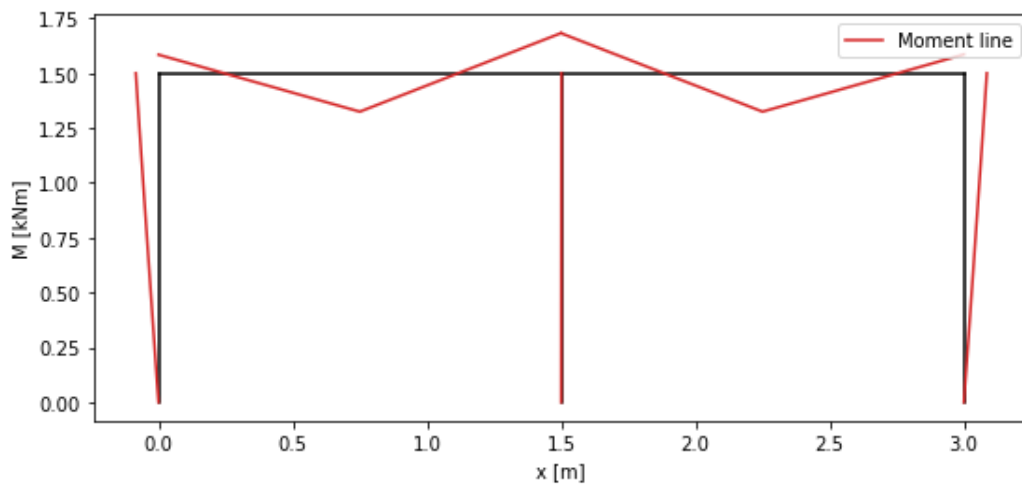


Figure 5.21: Bending moment diagram resulting from the DSM toll when only vertical loads are applied

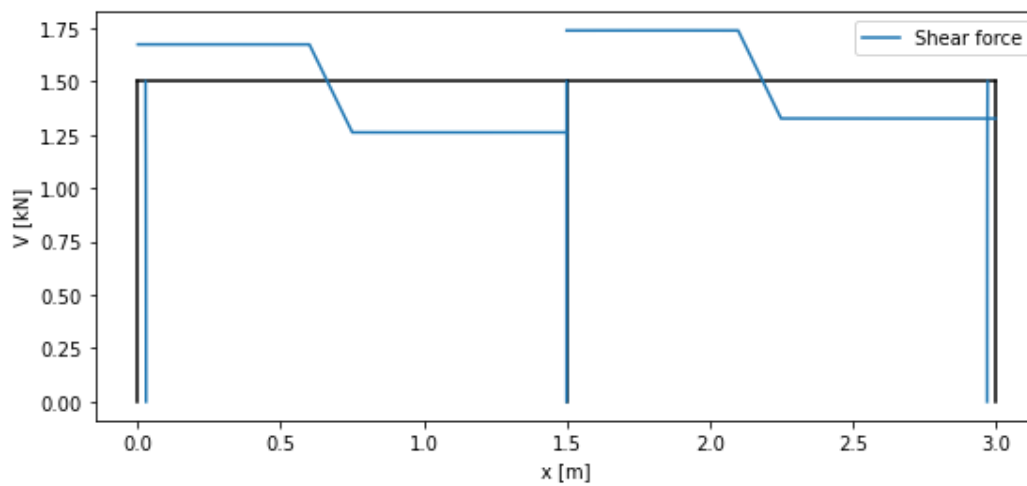


Figure 5.22: Shear force diagram resulting from the DSM toll when only vertical loads are applied

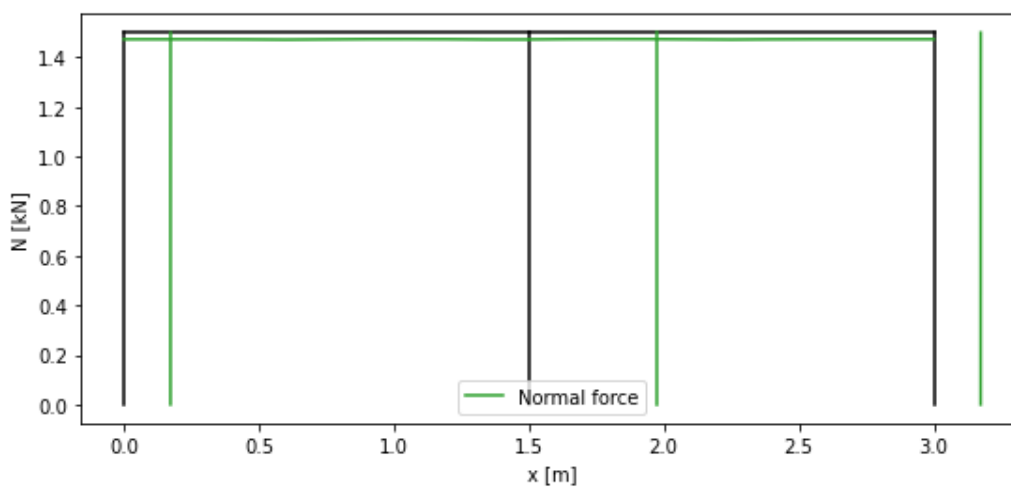


Figure 5.23: Normal force diagram resulting from the DSM toll when only vertical loads are applied

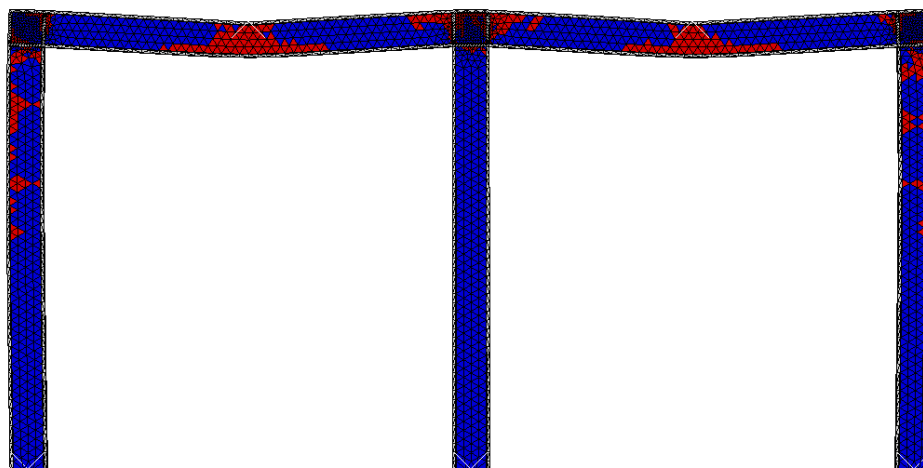


Figure 5.24: Resulting crack pattern for the frame modelled with JPSG1010 when only vertical loads are applied

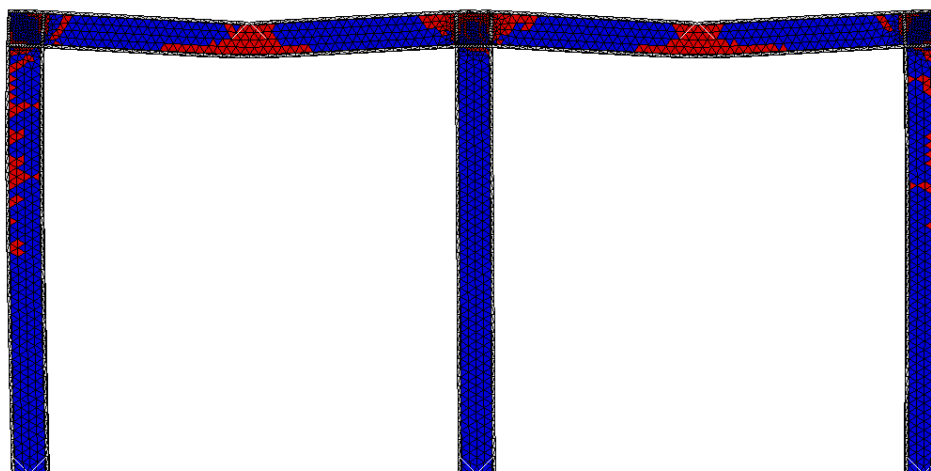


Figure 5.25: Resulting crack pattern for the frame modelled with JPSG0810 when only vertical loads are applied

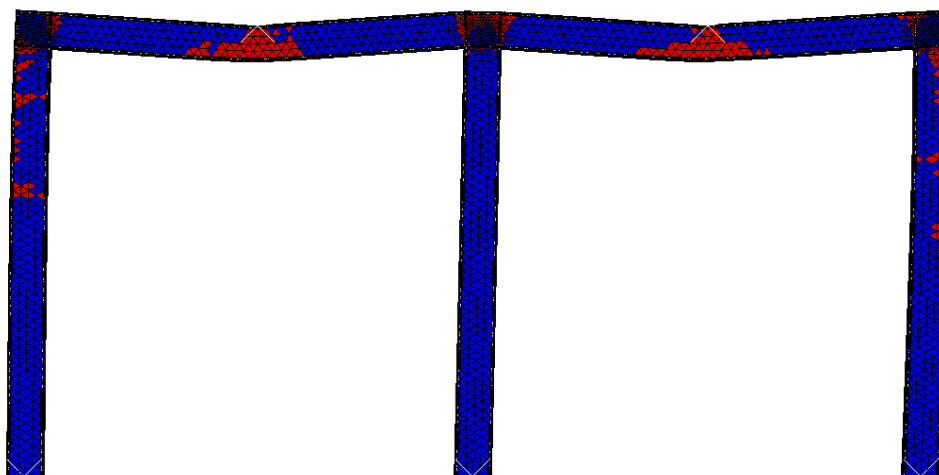


Figure 5.26: Resulting crack pattern for the frame modelled with JPSG1005 when only vertical loads are applied

5.4.2 Only horizontal load H

The analysis related with the application of just the horizontal load H gave the results reported in the graphs below in Figure 5.27, Figure 5.28 and Figure 5.29.

In the graphs is possible to clearly see the maximum displacement that each structure can withstand. This can be stated for the first two configurations, but it does not verify in the last configuration, which does not present a drop as the other two. The values are also reported in Table 5.2.

Regarding the frames modelled with JSPG1010 and JSPG0810 it can be observed that both configurations can support higher horizontal loads compared to the case in which both vertical and horizontal load are applied. In particular, the load that is supported is around 30% higher in both cases.

The last case, the structure constituted by JPSG1005 has an increase in the structural capacity lower compared with the previous two cases, just 20%. However, as previously stated, this case does not present a real ultimate displacement, but it follows a constant branch.

The results obtained from the Python modelling are quite distinctive. The initial stiffness is approximated to some extent when considering both rigid and semi-rigid connections. Similar to the cases presented earlier, the frame experiences collapse at lower loads compared to ABAQUS due to the reasons outlined in various sections. A noteworthy aspect is that in this scenario, the behaviour is more accurately replicated when considering connections as rigid.

Once again, the diagrams for bending moment, shear force, and normal stress are presented in Figure 5.30, Figure 5.31 and Figure 5.32. Analysing the bending moment diagram, it is evident that the crack patterns align with its distribution (Figure 5.33, Figure 5.34 and Figure 5.35). Specifically, the cracks converge at the top of the columns, beneath the connections, and in the connection associated with the right column, where the bending moment is greater.

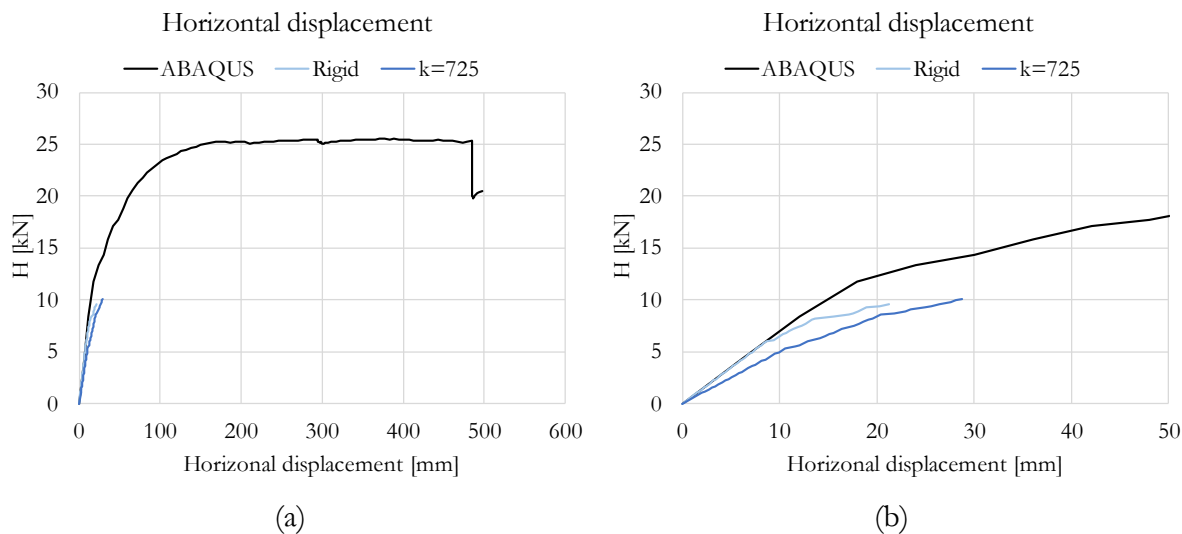


Figure 5.27: Resulting curves with the maximum horizontal displacement achieved (a) and with a focus on the initial stiffness (b) for the frame modelled with JPSG1010.

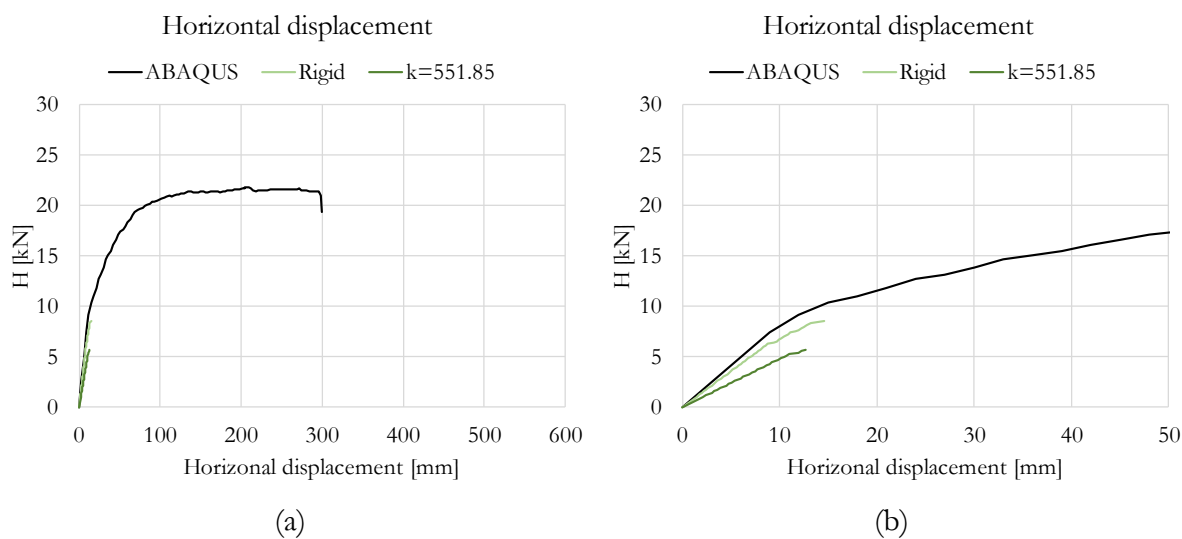


Figure 5.28: Resulting curves with the maximum horizontal displacement achieved (a) and with a focus on the initial stiffness (b) for the frame modelled with JPSG0810.

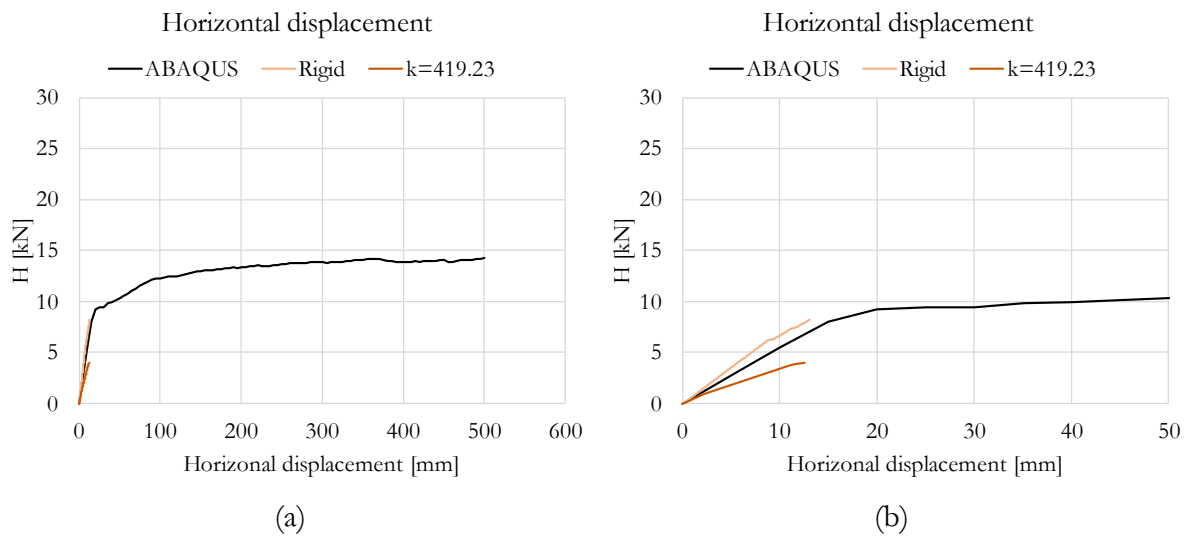


Figure 5.29: Resulting curves with the maximum horizontal displacement achieved (a) and with a focus on the initial stiffness (b) for the frame modelled with JPSG1005.

Table 5.2: Numerical results coming from the numerical modelling with just horizontal load applied

Configuration	ABAQUS		DSM tool			
	H_{max} [kN]	v_f [mm]	Rigid		k	
			P_f [kN]	d_f [mm]	P_f [kN]	d_f [mm]
JPSG1010	25.52	485.50	9.58	21.65	10.10	28.70
JPSG0810	21.79	298.63	8.50	14.56	5.66	12.64
JPSG1005	14.22	- (*)	8.22	13.08	4.03	12.51

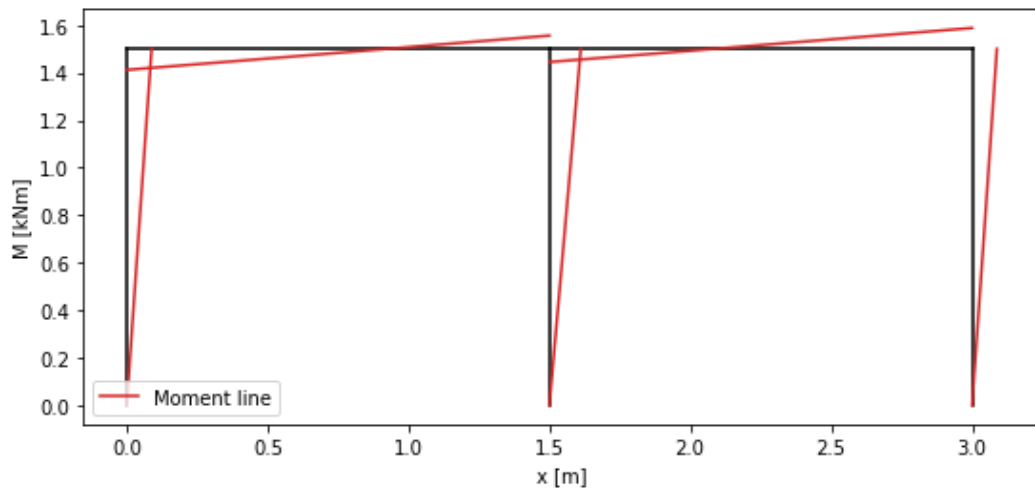


Figure 5.30: Bending moment diagram resulting from the DSM toll when only horizontal load is applied

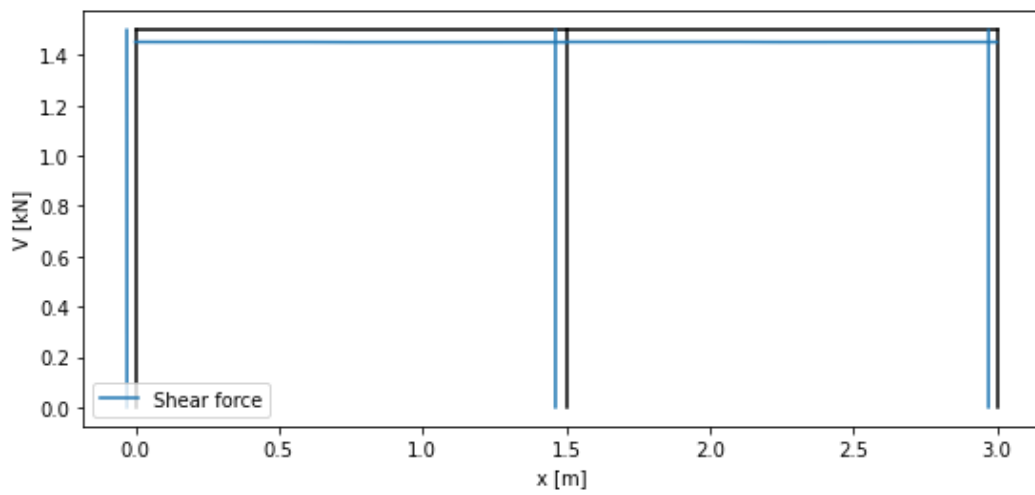


Figure 5.31: Shear force diagram resulting from the DSM toll when only horizontal load is applied

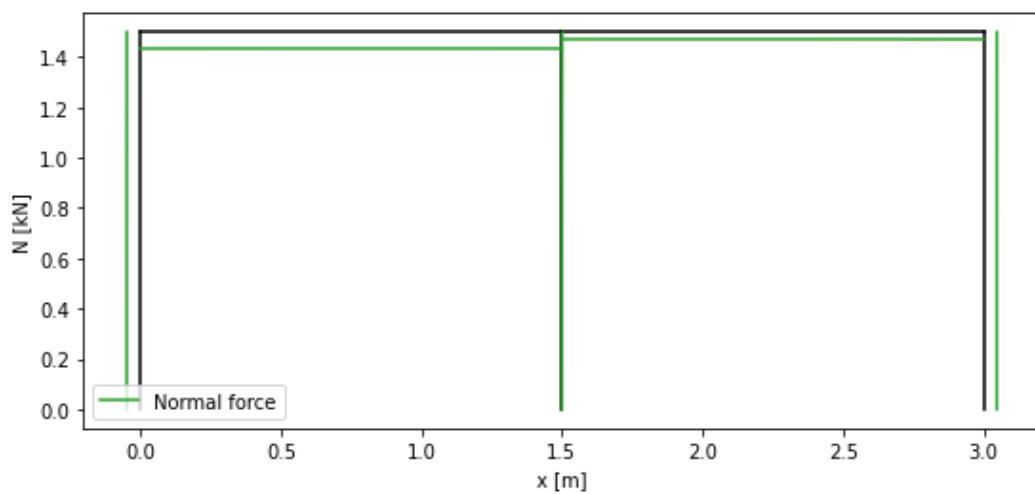


Figure 5.32: Normal force diagram resulting from the DSM toll when only horizontal load is applied

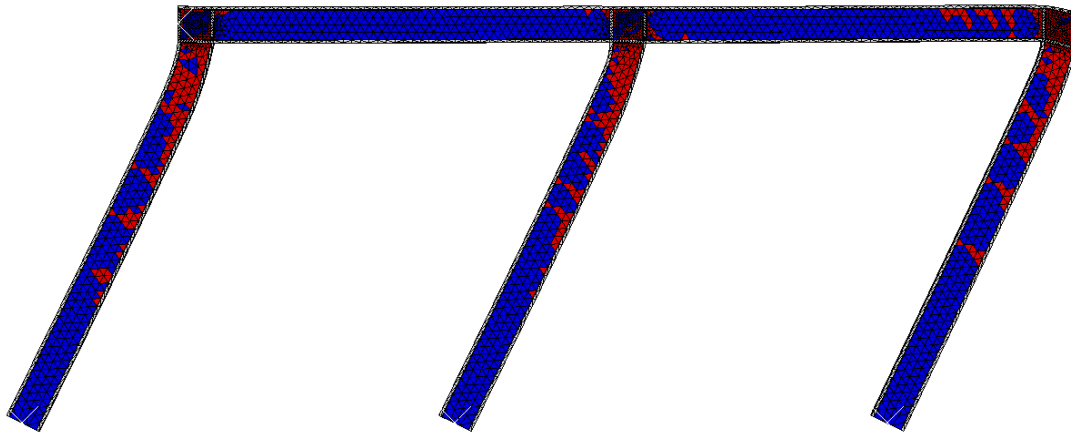


Figure 5.33: Resulting crack pattern for the frame modelled with JPSG1010 when only horizontal load is applied

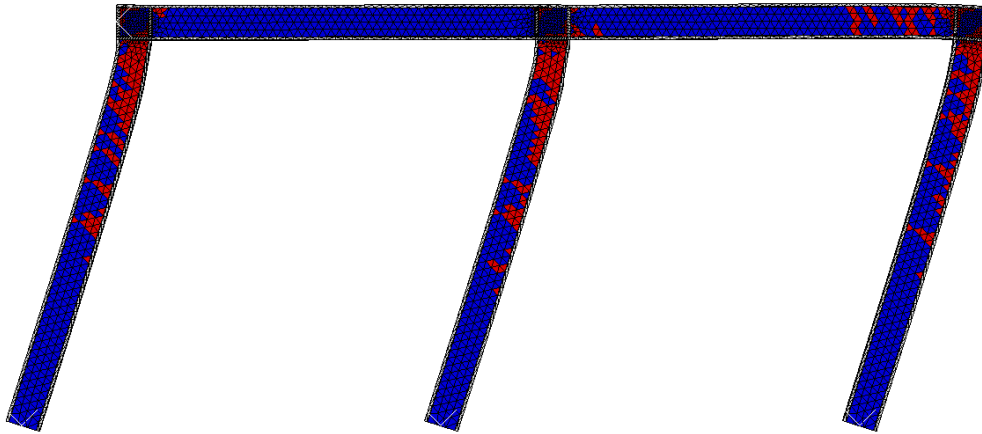


Figure 5.34: Resulting crack pattern for the frame modelled with JPSG0810 when only horizontal load is applied

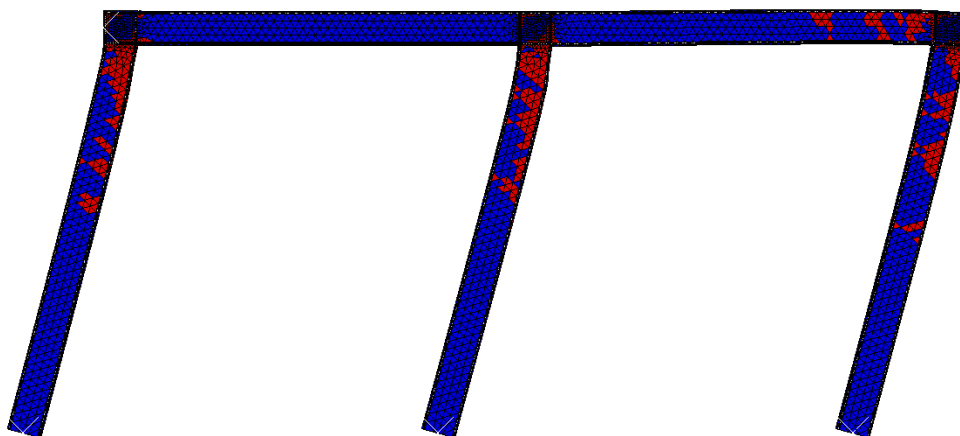


Figure 5.35: Resulting crack pattern for the frame modelled with JPSG1005 when only horizontal load is applied

5.4.3 Two-step analysis

In this section the application of the load will not be simultaneously as in the cases previously treated in Chapter 5.1. The analysis that will be performed come from models created in ABAQUS Standard since the DSM tool does not have the possibility to create a two-step analysis.

The study will be focus on understanding the influence of different values of the vertical load on the global behaviour of the structure.

The applied horizontal force will differ for each case under examination. the selected values are derived from the outcomes presented in the previous Chapter 5.4.2, where the behaviour of the frame was analysed under solely horizontal loads. This with the aim to stress the influence that the gravity load has on the horizontal capacity of the frame.

In all three instances, the reference curve, designated simply as P emerges as the outcome of implementing a 100 m displacement in the downward y -direction, followed by a 100 m displacement in the x -direction.

In all three cases, it can be observed that the graph depicting the horizontal displacement, resulting from this initial analysis, exhibits a displacement in the negative x -direction, discernible through the presence of straight lines along the x -axis. This is because, due to the hinged boundary conditions at the base and the significant vertical displacement, the frame has become unstable and started to slide towards the left (negative x -direction). This behaviour has been recorded in all three frames with different values. Subsequently, at the end of the first step of the analysis, the application of the horizontal load occurs, resulting in the curves observed for the different cases. Has to be pointed out that, this instability has not occurred, or to a lesser extent, in cases where a smaller loads P have been applied.

Various curves have been derived by applying distinct vertical displacement magnitudes. This approach has been undertaken to yield diverse load P values. It is feasible to discern the distinct peak values in the deflection graphs illustrated below in Figure 5.36 (a), Figure 5.39 (a) and Figure 5.42 (a). In particular, the values of the different impose deflections and the relative P load values are reported in Table 5.3, Table 5.4 and The last case under analysis, utilizing the JPSG1005 section, behaves similarly to the preceding JPSG0810 case. As in the previous instance, it is not feasible to pinpoint structural failure clearly. The decrease in load-bearing capacity is also comparable, where applying 30% of load P results in an 8% reduction, and the application of 70% of load P leads to a 20% decrease in capacity. When the maximum load P is applied, the reduction in strength is 35%.

By following the same assumptions adopted in the previous case, the structural failure was assumed for horizontal displacements beyond which a decrease in data was observed, followed by the initiation of the ascending branch. Unfortunately, in this case, it is not possible to compare the data with the results of the earlier analysis, as obtaining consistent results from ABAQUS was not possible. In this case further experimental investigation is needed.

Table 5.5. Regarding the horizontal capacity of the frame, it remains relatively consistent despite alterations in the vertical load.

The tables below present the outcomes for the various scenarios. For the deflection measurements, the applied displacement d and the maximum vertical load P_{max} endured by the structure are reported. Regarding the horizontal displacements, H_{max} denotes the maximum horizontal force the structure experienced before reaching failure, which transpired at a displacement denoted as v_f .

It is important to emphasize that the highest load was not observed to coincide with the ultimate point of failure displacement. This holds true, especially in the instance of the initial lamination JPSG1010, wherein the peak force is documented following the conclusion of the elastic phase. Beyond these peaks, a declining behaviour is evident, culminating in the structural failure marked by a significant drop.

In the subsequent two cases, interpretation of the results has enabled to identify the failure as a decrease in the data, followed by the begin of a divergence branch.

In the first case, characterized by the frame modelled with the JPSG1010 lamination, it can be observed that the application of the maximum load P results in the frame having enough strength to still support a horizontal load H of 16.81 kN. However, when a portion of the load P is applied, the frame can sustain higher horizontal loads, averaging around 22 kN. This leads to an increase of 23% in load-bearing capacity compared to when the maximum load P is applied.

This result can be compared with the outcomes from the previous Chapter 5.4.2, where only a horizontal force was applied. In that case, the maximum value of load H was 25.52 kN. This implies that, applying a load P between 70% and 30% of the maximum vertical load, the horizontal load-carrying capacity of the structure is reduced 17% to 10%.

Furthermore, it is essential to emphasize that the failure of the structure occurs at significantly lower horizontal displacements compared to when only horizontal loads are applied. This is because, at the end of the application of load P , crack formation is already occurring in various parts of the structure, in particular in the connections and at the centre of the beams. This can be

observed in the crack patterns presented in Figure 5.37. The final displacement can decrease by 42%, when a load equal to 70% of P is applied, and by 35% when 30% of P is applied.

Table 5.3: Numerical results of the two-step analysis for the frame modelled with JPSG1010

Load	Deflections		Horizontal displacements	
	d [mm]	P_{max} [kN]	v_f [mm]	H_{max} [kN]
P	100	72.51	73.15	16.81
30%P	3	22.84	319.97	22.85
50%P	4	32.82	250.16	21.75
70%P	5	52.92	280.37	21.11

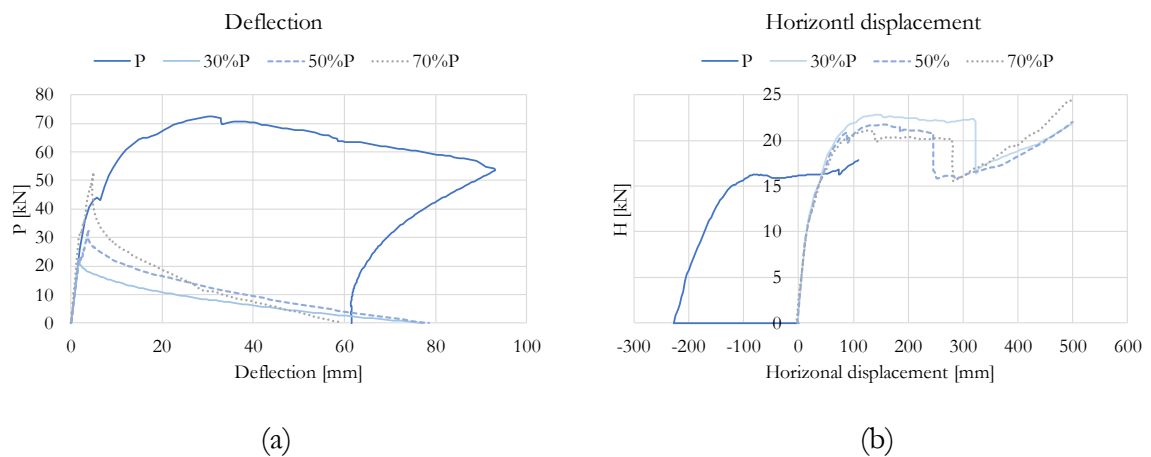


Figure 5.36: Resulting curves for frame modelled with JPSG1010 on which different percentage of load P have been applied followed by H

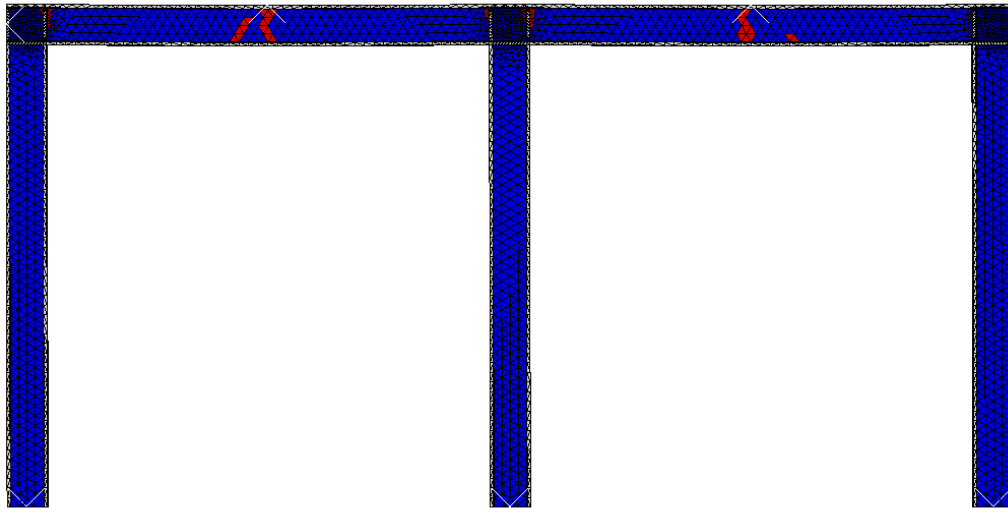


Figure 5.37: Crack pattern at the end of the first step, when 50% of the vertical load is applied, for the frame modelled with JPSG1010

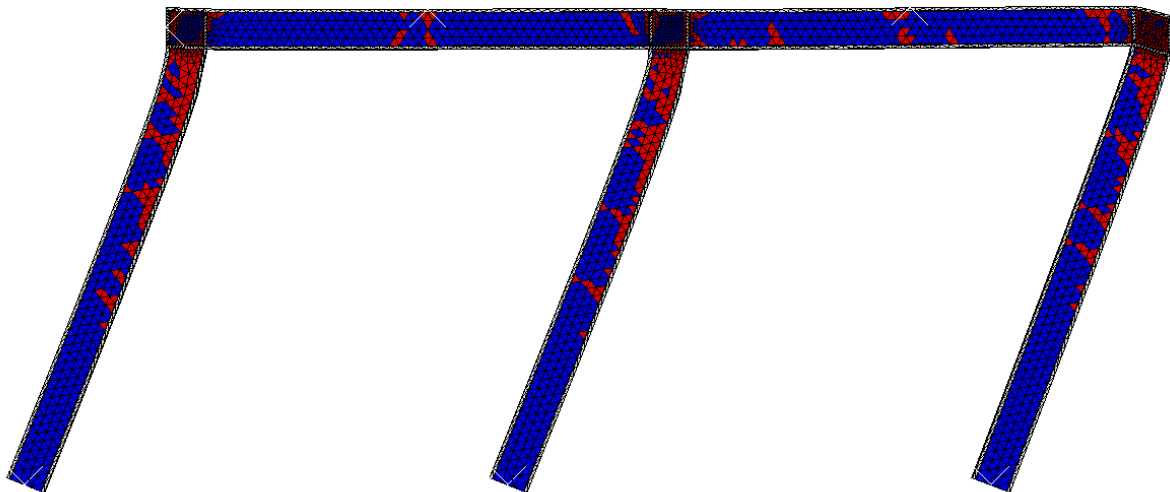


Figure 5.38: Crack pattern at the end of the two-step analysis for the frame modelled with JPSG1010

The second lamination under examination presents similar results to the first, however notable deviations are registered particularly when a percentage of load P is applied. In this case, when the maximum load P is applied, the vertical load-bearing capacity decreases by 35%, compared when only the horizontal load is applied. However, when 70% of load P is applied, the capacity drops by 21%, and in the case of applying 30% of load P , the capacity decreases of a lower amount, by 7%.

The intriguing aspect of these simulations is that the structural failure is not clearly discernible from the graphs. After the end of the elastic range, the curves appear to diverge. A closer examination of the data reveals that at certain points, there is a reduction followed by the start of the ascending branch. At these points, the failure of the structure was assumed, which in this case coincides with the maximum horizontal load considered.

This final failure occurs at obviously smaller horizontal displacements. The registered decrease moves from 40% to 45% when 30% or 70% of the vertical load is applied. Therefore, in this case, the horizontal displacement decreases to a greater extent.

Table 5.4: Numerical results of the two-step analysis for the frame modelled with JPSG0810

Load	Deflections		Horizontal displacements	
	d [mm]	P_{max} [kN]	v_f [mm]	H_{max} [kN]
P	100	60.52	14.24	14.10
30%P	2	20.12	179.74	20.22
50%P	5	33.95	181.98	18.79
70%P	7	42.74	166.62	17.18

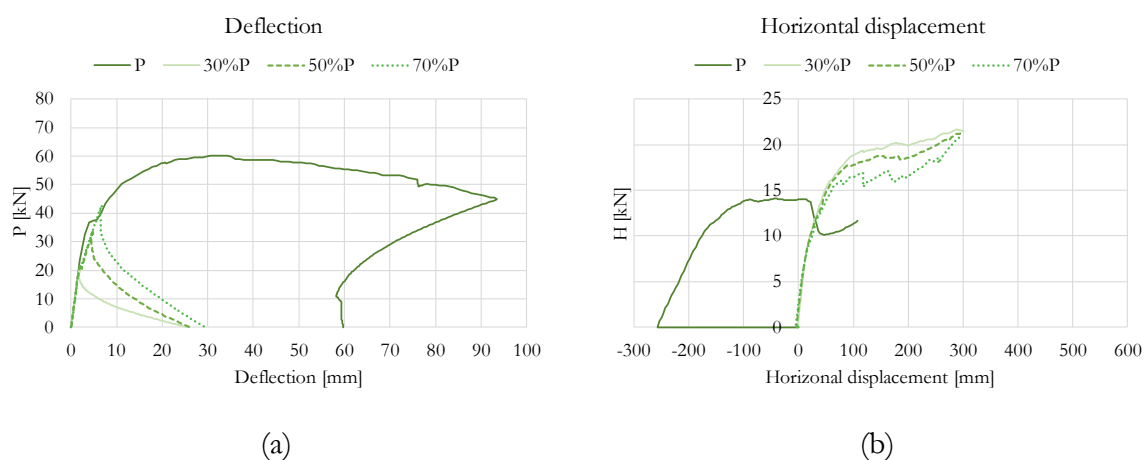


Figure 5.39: Resulting curves for frame modelled with JPSG0810 on which different percentage of load P have been applied followed by H

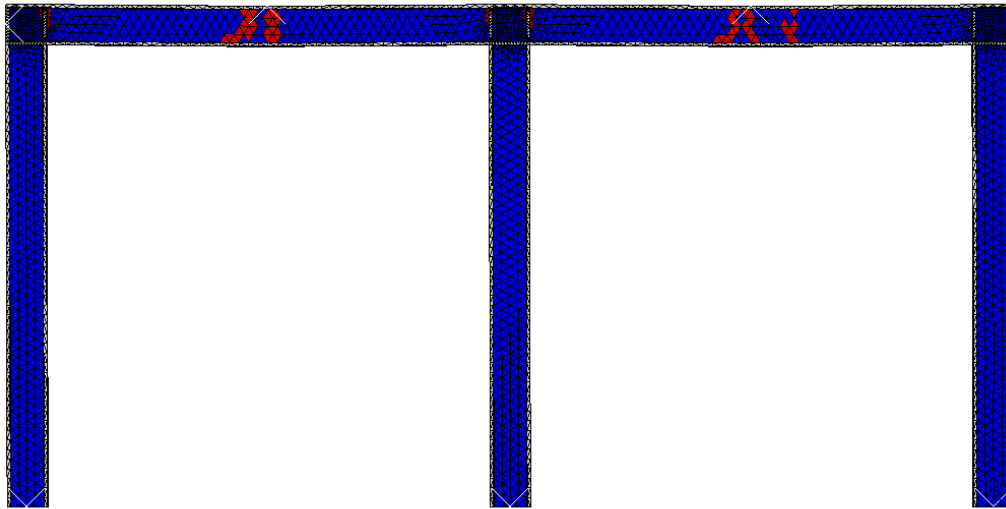


Figure 5.40: Crack pattern at the end of the first step, when 50% of the vertical load is applied, for the frame modelled with JPSG0810

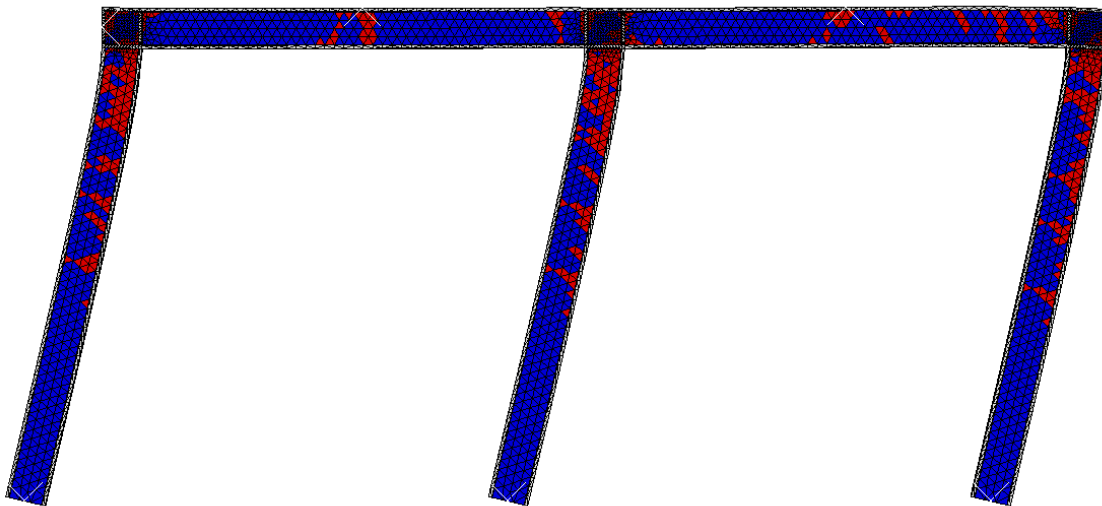


Figure 5.41: Crack pattern at the end of the two-step analysis for the frame modelled with JPSG0810

The last case under analysis, utilizing the JPSG1005 section, behaves similarly to the preceding JPSG0810 case. As in the previous instance, it is not feasible to pinpoint structural failure clearly. The decrease in load-bearing capacity is also comparable, where applying 30% of load P results in an 8% reduction, and the application of 70% of load P leads to a 20% decrease in capacity. When the maximum load P is applied, the reduction in strength is 35%.

By following the same assumptions adopted in the previous case, the structural failure was assumed for horizontal displacements beyond which a decrease in data was observed, followed by the initiation of the ascending branch. Unfortunately, in this case, it is not possible to compare the data with the results of the earlier analysis, as obtaining consistent results from ABAQUS was not possible. In this case further experimental investigation is needed.

Table 5.5. Numerical results of the two-step analysis for the frame modelled with JPSG1005

Load	Deflections		Horizontal displacements	
	d [mm]	P_{max} [kN]	v_f [mm]	H_{max} [kN]
P	100	36.28	14.24	9.28
25%P	1	9.03	216.13	13.08
50%P	3	17.14	169.53	12.41
70%P	6	25.13	117.87	11.34

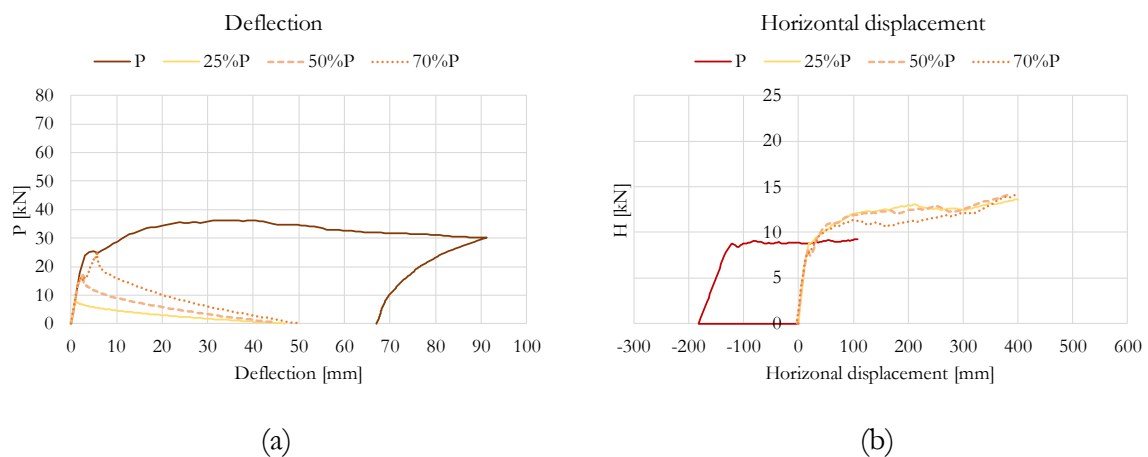


Figure 5.42: Resulting curves for frame modelled with JPSG1005 on which different percentage of load P have been applied followed by H

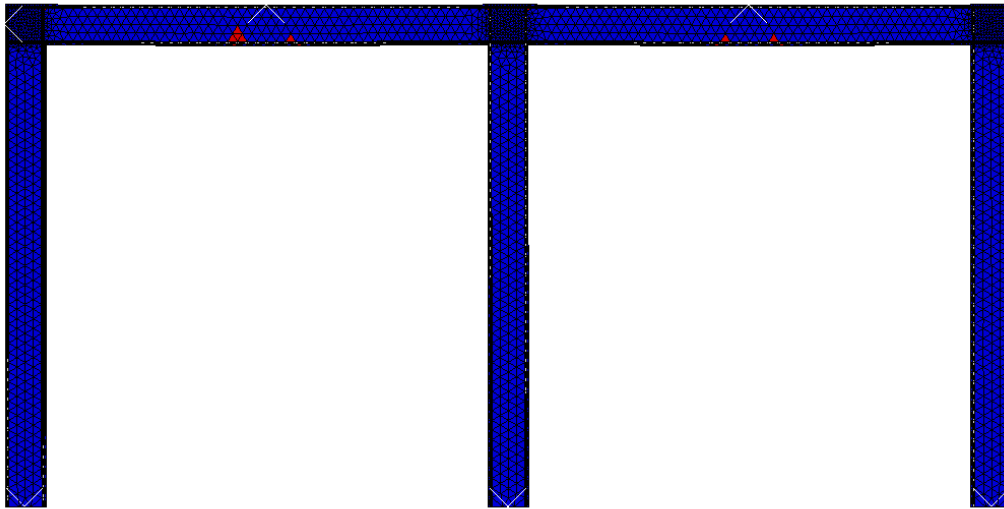


Figure 5.43: Crack pattern at the end of the first step, when 50% of the vertical load is applied, for the frame modelled with JPSG1005

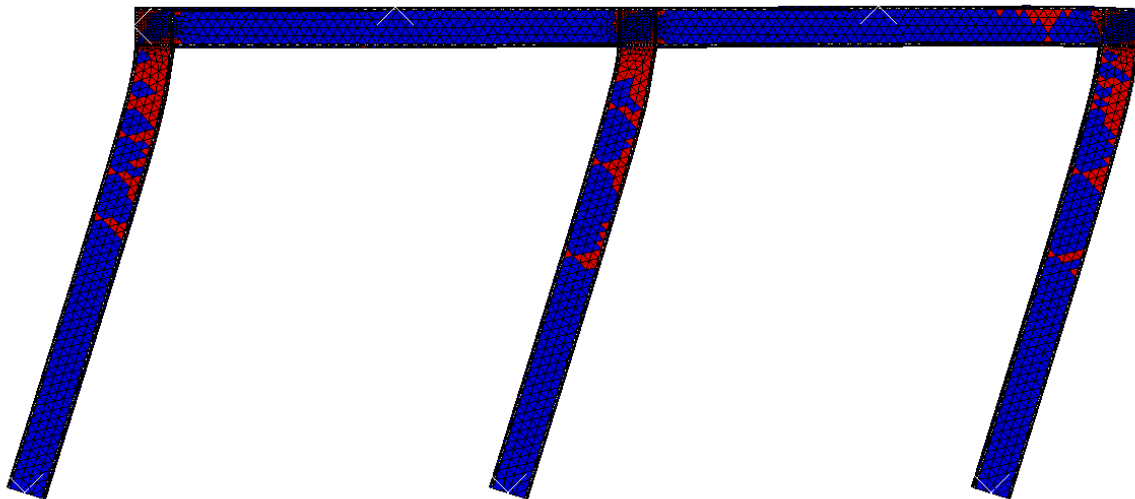


Figure 5.44: Crack pattern at the end of the two-step analysis for the frame modelled with JPSG1005

Chapter 6 - Conclusions

6.1 Overall conclusions

The study of connections within the field of glass structures is certainly of paramount importance. From this, the thesis has focused its attention on assessing the impact of the stiffness of the connections, modelled through springs, on the response of the structure.

In particular, starting from the experimental outcomes, a rotational stiffness constant was defined and subsequently employed within the DSM tool. The results demonstrated that utilizing the correct connection stiffness accurately reproduces the experiments. However, owing to the construction of the code, once the maximum bending moment capacity is reached in a section, the tool assumes the entire structure has collapsed. This leads to a situation where, in the case of analysing an individual connection, the plastic capacity of the steel reinforcement was not recreated in a correct way. It should be noted, though, that the behaviour of the models up to the end of the elastic branch accurately replicates what was obtained in the experiments.

Regarding the analysis of the frame performed with the DSM tool, multiple factors influence the obtained results. Primarily, the analysis is always based on the moment-curvature diagram of the section, so when the capacity is reached in a section, the entire structure collapses. Additionally, the code does not consider stress redistribution and creates cracks in a punctual manner that then expand until failure. Lastly, considering the rigidity of the connections, this was assumed to be the same for all three nodes of the frame. However, the connection at the central node does not have the same configuration as the two connections at the ends, where only beam and column are connected, this aspect also impacts the overall response of the structure.

Analysing the results of the 3D model created using ABAQUS, it accurately reproduces the behaviour of the structure. Specifically, concerning the connection, the stiffness of the first case JPSG1010 is optimally recreated. For the other two cases, some inaccuracies are present. In the second configuration JPSG0810, the model seems to be overly rigid in the elastic linear phase but then accurately replicates the plastic behaviour of the stainless-steel reinforcement, having a bending capacity comparable to once of the experiments. Meanwhile, the third case, JPSG1005, exhibits results with a trend similar to the experimental one but presents higher bending moment capacity. This discrepancy could be attributed to the inability of the ABAQUS model to recreate the loss of adhesion between reinforcement and interlayer.

Comparing the results obtained from the connection modelling, it can be concluded that the ABAQUS model more accurately reproduces the behaviour of the latter, partly because the model

Conclusions

was created with fewer approximations. The results from the Python model accurately replicate the behaviour of the connection in the elastic linear phase of materials, but when secondary effects come into play, the model struggles to recreate the correct behaviour of the connection.

Regarding the frame analysis, it can be concluded that the DSM tool fails to accurately analyse this type of structure. The initial stiffness is comparable to that in ABAQUS, but the structural failure occurs at lower loads. This is due to how the code works, being based on the moment-curvature relationship and the creation of individual cracks that then propagate as the load increases. On the other hand, the 3D model in ABAQUS considers the crack formation based on the UMAT model, which recreated the brittle behaviour of glass. The ABAQUS model describes a behaviour that can accurately replicate the response of the frame. This can be evidenced by the crack patterns that is in line with what is expected from the given loading configuration. However, to prove this, further experimental investigation is needed.

From the parametric study, the maximum capacities for vertical and horizontal loadings of the frame were obtained. After this, the study focused on a two-step analysis where vertical loads were applied first, followed by horizontal loading. From these studies, it emerged that applying loads lower than the maximum capacity that the structure can support allows for good resistance to horizontal loads. The forces that the frame can still sustain after the application of vertical loads decrease on average by 20% when 70% of the vertical load is applied, compared to the analysis where only horizontal loads are applied. Meanwhile, the maximum displacements leading to structural collapse decrease by approximately 40% when 70% of the maximum vertical load is applied.

Overall, it can be stated that the Finite Element Model (FEM) created in ABAQUS Standard accurately replicates the behaviour of the various types of laminations, despite some discrepancies being present. On the other hand, the analytical model based on the Direct Stiffness Method and implemented through the Python code fails to accurately reproduce the entire behaviour of the laminations, but it accurately reproduces the linear-elastic phase. Efforts are being made to achieve more accurate results, however those are difficult to achieve due to the high level of assumptions that must be done in order to model both the cross-sections and the configurations.

6.2 Future work

In the specific context of the current research, it can be observed that the behaviour of the beam-column connection is accurately replicated by the ABAQUS software. The same cannot be said for the connection modelled through the DSM tool, where a more focused implementation of the code is required to address the brittle behaviour of glass and how fractures propagate, as in the case of a UMAT model. Another option is to work on the moment-curvature diagrams in a different way, without altering the geometric characteristics of the section but changing how they are defined.

Regarding the frame analysis, to determine whether the results obtained from the ABAQUS model are sufficiently accurate, experimental studies need to be conducted. These studies would help capture the actual behaviour of the frame. This is important because in a frame, various mechanisms are activated simultaneously, leading to secondary effects that the ABAQUS model might not replicate accurately.

As for the frame model recreated using the Python code, the previously suggested approaches remain valid on a material level. In this case, a more in-depth study of the central connection, where there are two beams and a column, should be carried out. Unfortunately, without experimental results that can prove the correct value of the spring constant, recreating the stiffness of that connection using a k value is quite challenging.

As a final improvement, a more thorough study of the stiffness of the base connection of the column could also be conducted, allowing this connection to be modelled as a spring with a certain rigidity as in the case of the top connections.

Bibliography

- [1] Bos, F. P. (2009). *Safety Concepts in Structural Glass Engineering. Towards an Integrated Approach*. PhD thesis, Delft University of Technology.
- [2] Cupač, J., Martens, K., Nussbaumer, A. et al (2017). *Experimental investigation of multi-span post-tensioned glass beams*. *Glass Struct Eng* 2, 3–15. <https://doi.org/10.1007/s40940-017-0038-5>.
- [3] Huang, W. (2017). *L-shaped Connection for Glass Portal Frame. Structural analysis and its application*. TU Delft.
- [4] J. Wright and J. MacGregor (2012). *Flexure: Behaviour and Nominal Strength of Beam Sections*. in *Reinforced Concrete: Mechanics and Design*, 6th ed. USA: Pearson, ch. 4, sec. 2, pp. 108-119.
- [5] Louter, P. C. (2011). *Fragile yet ductile: structural aspects of reinforced glass beams*. TU Delft.
- [6] Louter, P. C., Belis, J., Veer, F. A., and Lebet, J.-P. (2012b). *Structural response of SG-laminated reinforced glass beams; experimental investigations on the effects of glass type, reinforcement percentage and beam size*. *Engineering Structures*, 36:292-301.
- [7] Martens, K. (2018). *Statically Indeterminate Reinforced Glass Beams*. Ghent University.
- [8] Moreman, S (2022). *Rotational characteristics of steel reinforced glass beam-to-column adhesive joints: experimental and numerical study*. Ghent University.
- [9] Pejatovic, M., Caspeepe, R., & Belis, J. (2022). *Numerical study of post-fracture behavior of a two-sided reinforced laminated glass beam-column connection prototype*. *GLASS STRUCTURES & ENGINEERING*, 7(3), 399–414. <https://doi.org/10.1007/s40940-022-00193-x>
- [10] R. Van Coile (2016). *Towards reliability-based structural fire safety: development and probabilistic applications of a direct stiffness method for concrete frames exposed to fire*. M.Sc. dissertation, Dept. Struct. Eng., Ghent University.
- [11] Santarsiero, M., Bedon, C., Moupagitsoglou, K. (2019). *Energy-based considerations for the seismic design of ductile and dissipative glass frames*. *Soil Dynamics and Earthquake Engineering*. <https://www.sciencedirect.com/science/article/pii/S0267726119304063>
- [12] Symoens, E. (2019). *Experimental validation of a numerical model for the simulation of membrane action in reinforced laminated glass beam systems*. Ghent University.